INTERNAL REPORT
HIP-2019-04

Search for a Pseudoscalar Higgs Boson in the Context of Two-Higgs-Doublet Models

Jaana Heikkilä

HELSINKI INSTITUTE OF PHYSICS
P.O. Box 64 • FI-00014 UNIVERSITY OF HELSINKI • FINLAND

HIP Internal Report Series
HIP-2019-04

Search for a Pseudoscalar Higgs Boson in the Context of Two-Higgs-Doublet Models

Jaana Heikkilä

Department of Physics
Faculty of Science
UNIVERSITY OF HELSINKI

ACADEMIC DISSERTATION

To be presented, with the permission of the Faculty of Science of the University of Helsinki, for public criticism in the auditorium D101 of the Physicum building, Gustaf Hällströmin katu 2, Helsinki, on Friday November 22nd 2019, at 12 o'clock.

Helsinki 2019

Supervisors

Professor Paula Eerola, University of Helsinki

Dr. Giovanni Petrucciani, CERN

Pre-examiners

Associate professor Jonas Strandberg, KTH Royal Institute of Technology

Associate professor Stefania Xella, Niels Bohr Institute

Opponent

Professor Alexander Read, University of Oslo

ISSN 1455-0563

ISBN 978-951-51-1289-7 (paperback)

Printed by Picaset Oy

ISBN 978-951-51-1290-3 (pdf)

http://ethesis.helsinki.fi

Electronic Publications at the University of Helsinki

Helsinki 2019

HELSINGIN YLIOPISTO — HELSINGFORS UNIVERSITET — UNIVERSITY OF HELSINKI

Tiedekunta — Fakultet — Faculty	Laitos — Institution — Department
Faculty of Science	Department of Physics

Tekijä — Författare — Author
Jaana Heikkilä

Työn nimi — Arbetets titel — Title

Search for a Pseudoscalar Higgs Boson in the Context of Two-Higgs-Doublet Models

Oppiaine — Läroämne — Subject
Physics

Työn laji — Arbetets art — Level	Aika — Datum — Month and year	Sivumäärä — Sidoantal — Number of pages
PhD Thesis	November 2019	159 pages

Tiivistelmä — Referat — Abstract

A search for a pseudoscalar Higgs boson A is performed, focusing on its decay into a standard model-like Higgs boson h and a Z boson. Decays of the h boson into a pair of tau leptons are considered along with Z boson decays into a pair of light leptons (electrons or muons). A data sample of proton-proton collisions collected by the CMS experiment at the LHC at $\sqrt{s} = 13\,\text{TeV}$ is used, corresponding to an integrated luminosity of $35.9\,\text{fb}^{-1}$.

The search uses the reconstructed mass distribution of the A boson as the discriminating variable. This analysis is the first of its kind to utilise the SVFIT algorithm while exploiting the possibility to apply a mass constraint of 125 GeV in the $\text{h} \to \tau\tau$ four-vector reconstruction. The resolution of the reconstructed mass of the A boson is improved compared to the mass resolution obtained in previous analyses targeting the same final state.

No excess above the standard model expectation is observed in data. Model-independent as well as model-dependent upper limits in the m_A–$\tan\beta$ plane for two minimal supersymmetric standard model benchmark scenarios are set at 95% confidence level. The model-independent upper limit on the product of the gluon fusion production cross section and the branching fraction for the $\text{A} \to \text{Zh} \to \ell\ell\tau\tau$ decay ranges from 27 fb at 220 GeV to 5 fb at 400 GeV. The observed model-dependent limits on the process $\sigma(\text{gg} \to \text{A}+\text{b}\bar{\text{b}}\text{A})\mathcal{B}(\text{A} \to \text{Zh} \to \ell\ell\tau\tau)$ in case of the hMSSM (low-tb-high) scenario exclude $\tan\beta$ values from 1.6 (1.8) at $m_\text{A} = 220\,\text{GeV}$ to 3.7 (3.8) at $m_\text{A} = 300\,\text{GeV}$, respectively.

Avainsanat — Nyckelord — Keywords
Higgs physics, beyond the standard model, neutral Higgs bosons, CMS, LHC, CERN

Säilytyspaikka — Förvaringsställe — Where deposited

Muita tietoja — övriga uppgifter — Additional information

HELSINGIN YLIOPISTO — HELSINGFORS UNIVERSITET — UNIVERSITY OF HELSINKI

Tiedekunta — Fakultet — Faculty	Laitos — Institution — Department
Matemaattis-luonnontieteellinen tiedekunta	Fysiikan osasto

Tekijä — Författare — Author
Jaana Heikkilä

Työn nimi — Arbetets titel — Title

Search for a Pseudoscalar Higgs Boson in the Context of Two-Higgs-Doublet Models

Oppiaine — Läroämne — Subject
Fysiikka

Työn laji — Arbetets art — Level	Aika — Datum — Month and year	Sivumäärä — Sidoantal — Number of pages
Väitöskirja	Marraskuu 2019	159 sivua

Tiivistelmä — Referat — Abstract

Tässä väitöskirjassa kuvataan, kuinka pseudoskalaaria Higgsin bosonia A etsitään tutkimalla sen ennustettua hajoamista standardimallin Higgsin bosoniin h ja Z-bosoniin. Tutkittu lopputila koostuu kahdesta tau-leptonista ja kahdesta kevyestä leptonista (elektronista tai myonista), jotka ovat vastaavasti seurausta h-bosonin ja Z-bosonin hajoamisesta. Analyysi perustuu LHC-kiihdyttimellä tuotettuihin protoni-protoni-törmäyksiin, jotka on mitattu CMS-koeasemalla. Törmäyksien massakeskipiste-energia oli 13 TeV ja mitattu data vastaa $35.9\,\mathrm{fb}^{-1}$ integroitua luminositeettia.

Etsinnässä käytetään A-bosonin rekonstruoitua massaa erottelemaan törmäystapahtumat, jotka mahdollisesti sisältävät A-bosonin, ja ne, joissa sitä ei todennäköisesti ole. Higgsin bosonin h nelivektori rekonstruoidaan käyttämällä SVFIT-algoritmia, joka huomioi h-bosonin mitatun massan 125 GeV. Rekonstruoituun A-bosonin massaan liittyvä mittaustarkkuus paranee huomattavasti verrattuna mittaustarkkuuteen, joka saavutettiin aikaisemmissa samankaltaisissa analyyseissa. Tämä on ensimmäinen CMS-analyysi, joka käyttää tätä lähestymistapaa.

Standardimallin ennuste A-bosonin rekonstruoidun massan jakaumasta kuvaa mitattua dataa ilman merkittäviä poikkeavuuksia. Tilastolliset ylärajat A-bosonin tuottotodennäköisyydelle lasketaan sekä malliriippumattomasti että ottaen huomioon kaksi minimaalisen supersymmetrisen standardimallin ennustusta. Malliriippuvat ylärajat ottavat huomioon A-bosonin tuoton gluonifuusion kautta ja hajoamistodennäköisyyden tutkittuun kahden tau-leptonin ja kevyen leptonin lopputilaan. Malliriippuvat ylärajat vaihtelevat 27 ja 5 fb:n välillä, kun A-bosonin massa on vastaavasti 220 ja 400 GeV. Mitatut malliriippuvat ylärajat huomioivat myös A-bosonin tuoton kahden b-kvarkin kautta, toisin sanoen ylärajat asetataan prosessille $\sigma(\mathrm{gg} \to \mathrm{A} + \mathrm{b\bar{b}A})\mathcal{B}(\mathrm{A} \to \mathrm{Zh} \to \ell\ell\tau\tau)$. Kun tulokset tulkitaan hMSSM (low-tb-high) -skenaariossa, ne poissulkevat $\tan\beta$-arvot välillä 1.6 (1.8) ja 3.7 (3.8), kun A bosonin massa on vastaavasti 220 ja 300 GeV.

Avainsanat — Nyckelord — Keywords
Higgsin fysiikka, standardimallin laajennukset, neutraalit Higgsin bosonit, CMS, LHC, CERN

Säilytyspaikka — Förvaringsställe — Where deposited

Muita tietoja — övriga uppgifter — Additional information

To all the women who

have fought,

and still fight,

for equal possibilities and rights for all genders,

did not have a chance to go to school,

break the rules made to constrain them,

create new structures to empower everybody,

and never stop developing themselves.

Contents

Preface

In this thesis, I present a search for a pseudoscalar A in the decay channel $A \to Zh \to \ell\ell\tau\tau$. The search is performed using a data set of proton-proton collisions collected by the CMS experiment at CERN LHC. I am the key analyser, the contact author, and the paper editor of the corresponding CMS Collaboration publication [1], submitted to Journal of High Energy Physics. The preliminary results of the search were presented at the "54th Rencontres de Moriond 2019, Electroweak session". This is the first search targeting the $A \to Zh \to \ell\ell\tau\tau$ decay channel with proton-proton collision data collected at 13 TeV.

As the key analyser of this search, I made significant contributions to the optimisation of the A boson reconstruction. After studying multiple methods to reconstruct the A boson, I concluded to use the likelihood function method (SVFIT algorithm) while utilising for the first time in such an analysis the possibility to give a mass constraint of 125 GeV for the $h \to \tau\tau$ four-vector reconstruction. I optimised the event selection to support this implementation of the SVFIT algorithm. Another contribution of mine was the measurement of the reducible background. I studied different possibilities for estimating the shape and the yield of the reducible background, a crucial step in order to choose the most suitable option for the final results.

In addition to the analysis efforts, I worked on the Level-1 (L1) trigger both as the on-call expert during 2017 and 2018, as well as the L1 trigger Offline Certification

Co-Coordinator. One of my main achievements in two years of trigger work at CERN was to standardise the offline certification of the collected data. I developed certification procedures, which allowed us to perform the L1 trigger data certification at luminosity section level in 2017 and 2018. Due to these efforts on the L1 trigger data certification, combined with successful operation of the trigger system, only 9.8 pb^{-1} (<0.1%) of the data collected in 2018 was not qualified for physics analyses exclusively due to the offline certification of the L1 trigger.

Acknowledgements

I performed the research documented in this thesis at Helsinki Institute of Physics (HIP), and at the Compact Muon Solenoid (CMS) experiment at the European Organization for Nuclear Research (CERN). The research was funded by the University of Helsinki. Travels to multiple schools and conferences, also to CERN, have been funded by HIP and the doctoral programme of Particle and Universe Sciences at the University of Helsinki. Moreover, my 3-year stay at CERN was funded by HIP and the following foundations: Oskar Öflund foundation, Waldemar von Frenckell foundation, Vilho, Yrjö, and Kalle Väisälä foundation, and Magnus Ehrnrooth foundation. I am grateful for all the financial support provided by the aforementioned organisations.

In addition to the funding, I have been lucky to have numerous people in my life and career who have supported me along the way. It truly takes a village to raise a child, but also one to raise a doctoral candidate. Since doctoral studies can make one feel lonely and isolated, no doctoral student can survive such a project without relying on the work and support of others. I am proud to be part of the CMS Collaboration that has had a large impact on me as a researcher, and taught me that during challenging moments kindness and empathy will get one far.

I would like to thank Prof. Paula Eerola for giving me the opportunity to join the Helsinki Institute of Physics group in 2013. Thank you for always listening and sharing your wisdom related to physics analyses and life outside work. I value our

discussions about physics and everything that revolves around it. I have always looked up to you, and I have been able to share my thoughts with you. This marathon they call doctoral studies would have been much more bone-breaking without you guiding me.

I also wish to thank my thesis supervisor, Dr. Giovanni Petrucciani, who chose me as his summer student a long time ago in 2013, and proceeded to supervise also my Master's thesis before my PhD project. I am grateful to have had you on this road with me. During some extremely difficult times of my doctoral studies, you stayed around when nothing made sense, and always were there to mentor and discuss what step I should take next. I appreciate everything you have done, and I will forever be grateful for all the support and patience.

During my three years at CERN, I've had a chance to work with amazing and talented people without who this thesis wouldn't have been possible. Special thanks to Drs. Cecile Caillol, Tyler Ruggles, and Jan Steggemann for sharing their thoughts on my work, challenging my thinking, and helping me when I got stuck.

My stay at CERN was also filled with duties within the Level-1 trigger of the CMS experiment. The people in the trigger world taught me a lot, and I am forever grateful for the possibilities and responsibilities I was given. Special thanks to Drs. Pierluigi Bortignon, Terhi Järvinen, and Alexandre Zabi who first gave me the chance to enter the magical world of the Level-1 trigger. I would also like to thank Drs. Andrew Brikerhoff, Olivier Davignon, Emmanuel Perez, Dinyar Rabady, Alex Tapper, and Alessandro Thea, who helped me to grow into a Level-1 trigger Offline Certification Co-Coordinator. Finally, I would like to thank Dr. Santeri Laurila for sharing the coordinatorship with me - your presence, and our friendship and collaboration ensured the success we achieved.

I would like to thank my fellow PhD students and all my colleagues at the Helsinki Institute Physics, who have filled my days with good conversations, hap-

piness, and great brainstorming. Terhi, Juska, Santeri, Hannu, Joona, and Mikko L, thank you for letting me part of the great PhD student group at the Helsinki Institute Physics, and all the moments at work and outside it, including the nights in Helsinki and Geneva, hiking, roadtrips, and so much more! Special thanks for Asst. Prof. Mikko Voutilainen and Prof. Katri Huitu for mentoring and supporting me during my studies. To the staff at HIP CMS program (Kati, Matti, Tapio, Tomas, Henning), thank you for your advice and help regarding to multiple topics that have popped up during my doctoral studies, varying from tips on living in France, PR questions, or broken code. Thanks to the HIP secretaries, in particular Tuija Karppinen and Taina Onnela, for everything they did to help me to settle in France.

I want to thank Prof. Alexander Read for agreeing to be my opponent in the public defense of the thesis, and the pre-examiners Asst. Prof. Jonas Strandberg and Asst. Prof. Stefania Xella for reviewing my thesis. I would also like to show my gratitude for all the people who took time to give their feedback on my thesis.

To all my other friends and family inside and outside the world of particle physics: thank you for listening my complaints and stories of the academic world, as well as celebrating any successful moments with me. Special thanks to Alex, Chilufya, Chris, Hanna Kaisa, Ilkka, Jenna, Kristina, Martina, Salla, Veronica, and my godparents Ritva and Sakari, for always being there for me.

I believe my route towards this thesis started way before I was selected to a doctoral program. Ever since I was a small girl, I have showed interest in scientific experiments. I would like to thank my parents Virpi and Eetu for always encouraging me to do my thing. Thank you for keeping a good sense of humour and patience, for example when at age 6 I wanted to study if water truly boils at 100 degrees Celsius by sticking a bath-water thermometer to the boiling pot full of lunch potatoes. Eventually the thermometer exploded as the scale ran out (it ended at 80 degrees

Celsius), but you faced the situation with kindness and understanding.

Finally, I want to thank Willem for helping me to find my way in life and during the legendary Bear's trail hike in Finland. No words can possibly describe how grateful I am for your support, love, and proof-reading any text I wrote during my doctoral studies.

Geneva, 7th of November, 2019

Jaana Heikkilä

1. Introduction

The standard model (SM) [2–4] is currently the leading description of particle interactions. Despite of its imperfections, the standard model has survived numerous experimental tests. Perhaps the most important observation to support the standard model was the observation of a Higgs boson by the ATLAS and CMS experiments at CERN Large Hadron Collider (LHC) in 2012 [5–7]. However, theories beyond the standard model could offer explanations for more experimental phenomena compared to the standard model, and often this requires a rich spectrum of new particles. Some of these new particles could produce a signal similar to that of the standard model Higgs boson. Thus, after the discovery of the Higgs boson, two pressing research questions in high energy physics are to measure the properties of the observed particle, and to explore an extended scalar sector described by beyond standard model theories.

Extensive studies have been performed to measure the properties of the observed boson, such as couplings to fermions. All properties are found to be compatible with the SM expectations which constrains models describing physics beyond the standard model. Moreover, it has guided possible searches for new physics, none of which have resulted in discoveries. Two-Higgs-doublet models (2HDMs) form simple extensions of the SM [8, 9]. They predict the existence of five Higgs bosons. Two of these five particles are CP-even Higgs bosons (h and H), and thus either of them could correspond to the observed particle. This further encourages the study of

processes with experimentally accessible signatures and at least one SM-like Higgs boson. Regions of the parameter space of 2HDMs can be excluded by using the mass of the observed state. Searches for the other four Higgs bosons, namely the scalar H, the CP-odd Higgs boson A, and two charged Higgs bosons $H^{\pm}$, can constrain the rest of the parameter space.

The minimal supersymmetric standard model (MSSM), a popular extension of the SM, is a special case of the generic 2HDM [10]. As will be discussed in Chapter 2, the A boson has a large branching fraction for decaying into a SM-like Higgs boson h and a Z boson in certain parts of the parameter space of two MSSM benchmark scenarios, "hMSSM" [11–14] and "low-tb-high" [15]. This has motivated multiple searches, including the one presented in this thesis. Different experimental signatures from the h boson decays are targeted, while Z boson decays into two leptons are usually considered.

This thesis presents a search for the A boson using the Zh decay channel, where we consider the h boson decay into two tau leptons. In total four $\mathrm{h} \to \tau\tau$ decay channels are taken into account, and the Z boson can decay into two light leptons (electrons or muons), resulting in the following final states of the A boson decay: $\ell\ell + \mathrm{e}\tau_{\mathrm{h}}$, $\ell\ell + \mu\tau_{\mathrm{h}}$, $\ell\ell + \tau_{\mathrm{h}}\tau_{\mathrm{h}}$, and $\ell\ell + \mathrm{e}\mu$, where τ_{h} denotes a hadronic decay of the tau lepton. This search primarily targets the gluon fusion production of the A boson.

In order to perform a search of this kind, one naturally needs to try to produce the pseudoscalar A. Particle accelerators, such as the LHC, collide particles at high energies, producing a multitude of particles with varying masses. Since the majority of the heavy particles decay promptly, a great amount of effort has been put into designing and building particle detectors that can observe and measure the properties of the decay products of these interesting particles. This search is performed based on proton-proton collisions at the LHC, recorded using the CMS

experiment. The details of the experimental setup used for this thesis are described in Chapter 3. To understand if a collision event produced a pseudoscalar A, one must reconstruct the collision event as precisely as possible. In the CMS experiment, this is done using the particle-flow algorithm [16], described in detail in Chapter 4.

Once each interesting event has been reconstructed, the search for the pseudoscalar A can be performed. The analysis is presented in Chapter 5, where I discuss how events possibly including an A boson are selected. After careful consideration, the reconstructed mass of the A boson was chosen as the discriminating variable between the signal and background events. However, as the tau lepton decays include neutrinos that escape the detector, the visible mass of the pseudoscalar A is smaller than its true mass. Thus, a proper reconstruction of the A boson four-vector is a challenge to be tackled at the analysis level.

In this analysis, the neutrinos in the final states can be accounted for by using a likelihood function method (the SVFIT algorithm) to reconstruct the four-vector of the h boson. The SVFIT algorithm [17, 18] combines the four-vectors of both τ candidates whilst accounting for the missing energy. As this results in a better estimate of the h boson four-vector, the A boson reconstruction is also improved. For the first time in such an analysis, the possibility to give a mass constraint of 125 GeV for the $h \to \tau\tau$ four-vector reconstruction is exploited. This implementation of the SVFIT algorithm yields a constrained estimate of the h boson four-vector, and thus a better A boson mass resolution. The discrimination power of the reconstructed A boson mass is demonstrated in Section 5.5. The background estimation is discussed in Section 5.6.

In Chapter 6, I introduce the systematic uncertainties, and discuss how they are accounted for in the signal extraction method used to produce the results. Finally, the background prediction from the standard model is compared to the observed data events in Chapter 7, where also the model-independent and model-

dependent 95% confidence level (CL) upper limits are presented. The analysis and the results are summarised in Chapter 8, where an outlook is given.

2. Theory

In this chapter, I describe the necessary tools required to understand the theoretical aspects of searches for heavy neutral Higgs bosons. Beyond standard model (BSM) theories predicting the existence of the heavy neutral Higgs bosons are built upon the standard model (SM) of particle physics, that is introduced in the first part of the chapter. Special attention is paid on the Higgs mechanism, and the motivations for BSM theories are clarified by covering some of the shortcomings of the standard model.

A brief outline of the rest of the chapter is as follows: first, I discuss the production and decay of the standard model Higgs boson. Then, I cover the extended Higgs sector in BSM theories, concentrating on one of the simplest extensions, namely the two-Higgs-doublet models (2HDMs). I will also discuss the production and decay of heavy neutral Higgs bosons in the context of 2HDMs, justifying the process studied more in detail in this thesis. A non-exhaustive review of the experimental status of searches for heavy neutral Higgs bosons of 2HDMs is also presented.

2.1 Standard model of particle physics

The standard model of particle physics describes the elementary particles, categorised into fermions and bosons, and explains how these fundamental building blocks of nature interact with each other [2–4]. Fermions are spin 1/2 particles that respect Pauli exclusion principle and form all known matter, whereas the spin

1 bosons (photons, gluons, and W and Z bosons) mediate the three fundamental interactions described by the standard model: electromagnetic, weak, and strong interaction. Fermions can be further divided into quarks and leptons, that can interact in different ways depending on their chirality. Quarks are categorised into three generations, each consisting of one up-type and one down-type quark; (u, d), (c, s), and (t, b). The same categorisation is applied for leptons: (e, ν_{e}), (μ, ν_μ), and (τ, ν_τ), where ν_ℓ is a neutrino associated with the corresponding charged lepton ℓ.

All particles are represented as excited states of a quantum field, and thus the standard model is described by a Lagrangian density $\mathcal{L}$. As the standard model is a gauge theory, the Lagrangian density is invariant under local SU(3)×SU(2)×U(1) gauge transformations. The requirement for local gauge invariance demands utilising the covariant derivative, which has a specific form for each symmetry group. In general, a covariant derivative includes the gauge vector field(s), charge of the symmetry group, and of course the generators of the symmetry group. Thus, the covariant derivative generates all interactions described by the standard model and introduces the vector boson(s) mediating each interaction.

Photons are the carriers of electromagnetic interaction, whereas W and Z bosons are the carriers of the weak interaction. Gluons, the mediators of strong force, carry the colour charge unique only to them and quarks, as leptons, photons, W, and Z bosons are "colorless". Thus, electrons, muons, and tau leptons can interact by electromagnetic and weak interaction. Neutrinos, on the other hand, do not have an electric charge and thus take part only in the weak interaction. Quarks are the only elementary particles that can interact by strong, electromagnetic, and weak interaction. However, gluons and quarks can never exist as free particles due to colour confinement - they always form colourless particles such as protons. Gravitational force is not described due to the lacking quantum field theory formalism.

Since the Lagrangian is required to be invariant under the local gauge transformations, introducing any mass terms in the Lagrangian is prohibited. This does not cause problems with respect to photons and gluons as they are massless, but W and Z bosons have been measured to be massive. Moreover, it has been shown that leptons and quarks are not massless, and the range of the observed masses vary notably.

2.2 Higgs mechanism in the standard model

To introduce mass terms for W and Z bosons, the SU(2)×U(1) symmetry must be *spontaneously broken*. The Brout-Englert-Higgs mechanism [19–24] includes introducing a new field (the Higgs field) and requiring the local gauge invariance of the updated Lagrangian, where the Higgs field is a SU(2) doublet, and the covariant derivative is written in terms of four SU(2)×U(1) gauge bosons $\bar{W_\mu}$ and B_μ.

By choosing one vacuum state over the others, the symmetry is spontaneously broken. This give rise to mass terms for four eigenstates, namely for the vector bosons $W^\pm$, Z, and γ, out of which only the photon stays massless since the electromagnetic group is not broken. It is immediately noticed that there is a mass term also for the Higgs field, meaning that the standard model now includes a new physical state, so-called Higgs boson with a non-zero mass. By introducing Yukawa couplings in terms of the left-handed SU(2) doublets and right-handed singlets, the same Higgs field is able to explain masses of fermions. Even though the Yukawa coupling can be written for all fermions, the experimental data suggests that right-handed neutrinos do not exist [10], and thus the mass terms for neutrinos are usually neglected.

Nearly 50 years after being first postulated, a Higgs boson has been discovered in ZZ, $\gamma\gamma$, WW, $\tau\tau$, and $b\bar{b}$ decay channels [5–7, 25–30]. So far all the measurements on its properties suggest that it is compatible with the standard model expecta-

tion [31–33], which gives closure for the hunt for particles described by the standard model. Theories beyond the standard model, which can solve several of the open questions in particle physics, can additionally be constrained by these measurements. The mass of the Higgs boson is measured to be $125.26 \pm 0.20\,(\text{stat}) \pm 0.08\,(\text{syst})$ GeV based on data collected by the CMS experiment at a center-of-mass energy of 13 TeV [34]. Other measurements by the ATLAS and CMS experiments, including their combined results, are consistent with this value [35, 36].

2.3 Shortcomings of the standard model

Despite being able to answer perhaps the most critical question - the origin of the mass - the standard model is unable to explain multiple observations. Whether we discuss daily life phenomena such as gravitational force, cosmological measurements, or alternatively the size of the masses of the standard model particles, it becomes clear that standard model cannot be the final word - it must be just a piece of a larger puzzle.

For example, the mass of the Higgs boson is a free parameter of the standard model, meaning that only sophisticated guesses could be made on the size of the mass prior the observation. If anything, the standard model would suggest that the Higgs boson mass has to be rather large: when the higher order corrections to the Lagrangian are taken into account, the corrections to the mass of the Higgs boson become proportional to the cutoff energy scale (usually taken as the *Planck's scale*). This problem is also known as the *hierarchy problem*, as the observed, considerably light Higgs boson mass can be only achieved through some *fine-tuning* of the theory [10, 37].

Another experimental observation, neutrino oscillations, suggest that neutrinos have a small mass while they are considered massless in the SM [10]. As the Yukawa couplings include also the right-handed field, the neutrino masses are not described

by the standard model due to the experimental observation that all neutrinos are left-handed. Thus, according to the standard model neutrinos are massless as no candidate for right-handed neutrinos exist within the standard model.

Imperfections of the standard model are also confirmed in cosmological measurements. The way galaxies rotate suggests that there must be so called dark matter that interacts with the standard model particles at least through gravity. In other words, the standard model does not include a suitable candidate for the dark matter. Moreover, it is considered that at the start of the universe matter and antimatter existed in equal amounts. To explain the current excess of matter particles, it is necessary to introduce *matter-antimatter asymmetry*. CP-violation could partly explain why matter and antimatter decay at different rates, causing not all matter to annihilate away with antimatter. Even though the standard model can account for some of the CP-violation, it is not enough to create the required amount for the observed amount of asymmetry. Thus, there must be another source for the CP-violation.

Most of these problems are solvable by introducing more complex models, usually including more particles and often also more Higgs fields. The standard model relies on the spontaneous symmetry breaking, which can be extended to include for example multiple Higgs doublets. As long as the previous observations - including the standard model-like Higgs boson - are explained, any extended theory can be considered as a more complete theory. One of the extended theories, the supersymmetry (SUSY), introduces a superpartner for each of the standard model particle, with the same quantum numbers but different spin [37]. For example, the superpartner of the electron is *selectron* that is a spin 0 particle. The aforementioned higher order corrections to the Higgs mass would cancel as these new particles and their couplings to the Higgs boson would be taken into account.

Searches for new physics described by an extended theory can be performed

if the theory provides experimentally observable signatures. Moreover, if the already observed Higgs boson can be used as an experimental handle in the searches, exploring the extension of the standard model becomes an even more interesting challenge. Physics beyond the standard model could manifest itself as deviations from the standard model expectations in precision measurements of the Higgs boson properties, or as new particles that are yet to be discovered. In particular, previously unobserved particles could decay into a standard model-like Higgs boson that subsequently decays as described by the standard model. Searching for new physics using either approach requires understanding the properties of the standard model Higgs boson.

2.4 Standard model Higgs boson production and decay

The production and decay processes of the standard model Higgs boson depend on the mass of the boson, but also on the colliding particles and their energies. At the Large Hadron Collider, the main five production mechanisms of the standard model Higgs boson are: the gluon fusion, vector boson fusion, Higgs–strahlung, $b\bar{b}h$ and $t\bar{t}h$ associated productions [38]. *Cross sections* describing probabilities of these processes to occur in proton-proton collisions at 13 and 14 TeV are demonstrated in Fig. 2.1, which demonstrates that all of these processes are known beyond the leading order (LO). The electroweak corrections have been considered up to next-to-LO (NLO), whereas the perturbative quantum chronodynamics (QCD) corrections are often predicted up to next-to-NLO (NNLO).

In the BSM theories, the SM-like Higgs boson can be also produced in decays of heavier Higgs boson(s) of the model. As will be discussed in following sections, the main production modes of the Higgs boson(s) of extended theories may vary

greatly in different parts of the parameter space of the said theory. For example, the $b\bar{b}$ associated production can become the dominant production mode at certain regions of the extended theory's parameter space.

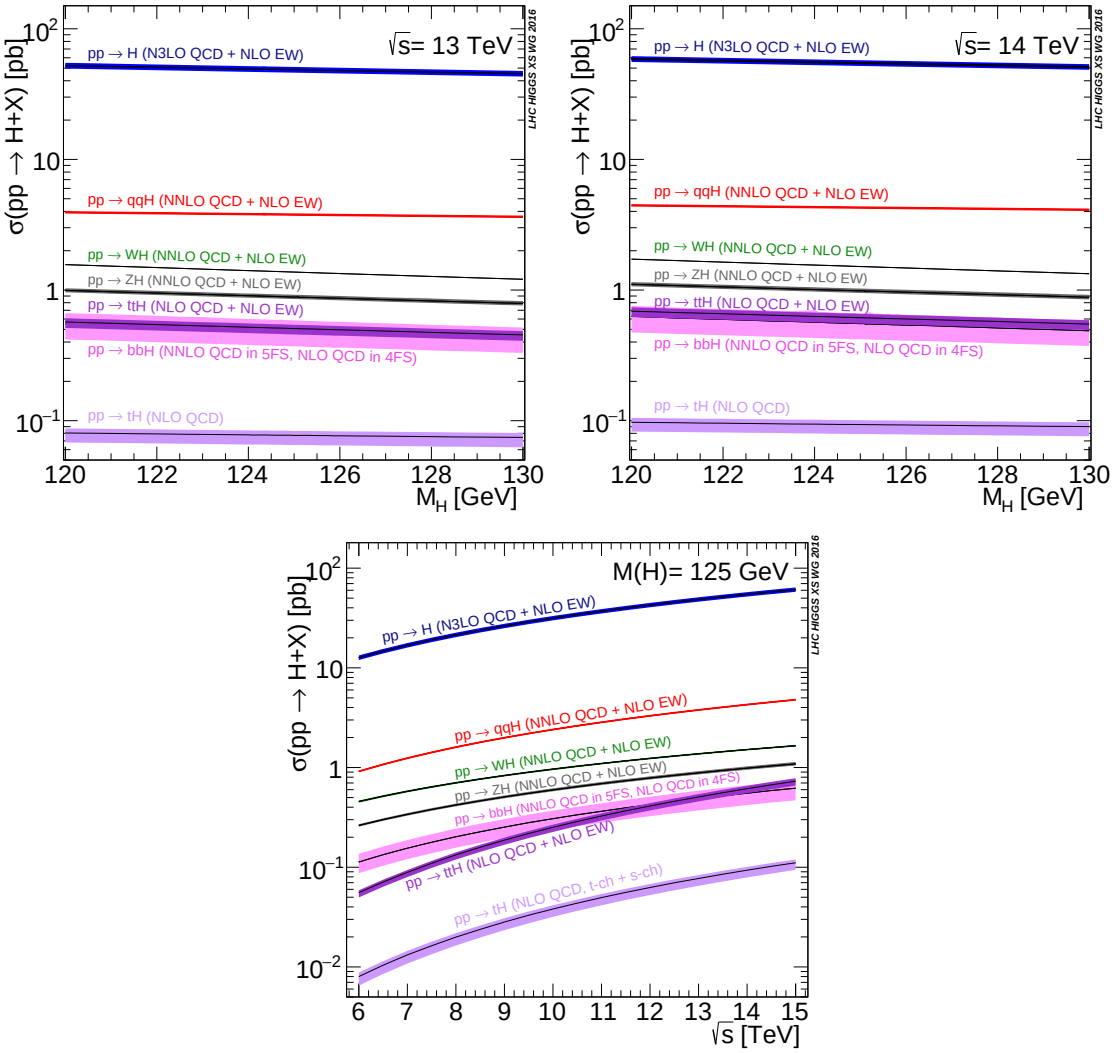

Figure 2.1: The theoretical production cross sections and their uncertainties for the standard model Higgs boson in proton-proton collisions at $\sqrt{s} = 13\,\text{TeV}$ (top left) and 14 TeV (top right) as a function of the Higgs boson mass. The theoretical cross sections for a 125 GeV Higgs boson as a function of center-of-mass energy (bottom). [38]

The decay of the Higgs boson to the standard model particles is similarly allowed as long as all conservation laws are respected. For this reason, the decays

into final states with photons or gluons are possible only via intermediate loops of quarks or vector bosons, while direct decays into fermions and gauge bosons can occur. *Branching fractions* expressing the probability for the Higgs boson decay into the most important final states are shown in Fig. 2.2.

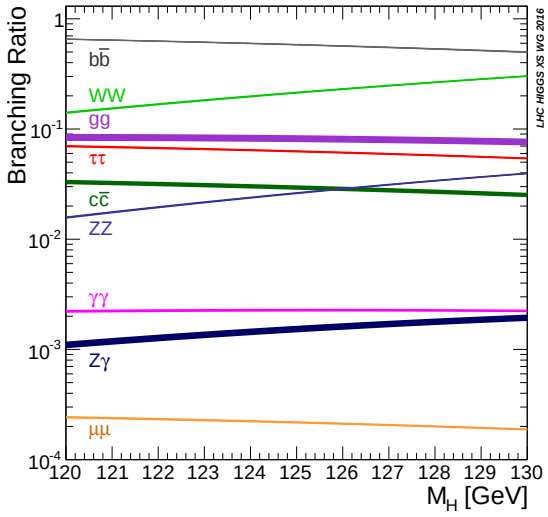

Figure 2.2: Branching fractions for the Higgs boson over the relevant mass range. [38]

The loop-induced Higgs boson decay into a photon pair has a clean experimental signature, and the invariant mass of the diphoton system can be measured with a high resolution. This channel was utilised in the groundbreaking searches that discovered the standard model Higgs boson in 2012 despite of the small amount of data. The process is usually dominated by the top quark and W boson loops.

The Higgs boson decays into two fermions with a probability that is proportional to the Yukawa coupling between the Higgs boson and a given fermion. Considering the observed mass of the standard model Higgs boson ($\sim 125\,\text{GeV}$), the dominating decay channels are $\text{b}\bar{\text{b}}$, $\tau^+\tau^-$, and $\text{c}\bar{\text{c}}$. Perhaps one of the most important decay channel of these three is the decay into two tau leptons, which offers a clean experimental signature unlike $\text{b}\bar{\text{b}}$ that is blurred by an overwhelming QCD background.

The decay channel with two (virtual) gauge bosons can offer another final state with a clean signature. The Higgs boson decay into two Z bosons that each further decay into two leptons (electrons or muons) is the so-called *golden channel* that led the discovery of the Higgs boson. However, the production of two gauge bosons is often one of the main background processes in searches utilising this decay channel of the Higgs boson.

2.5 Extended Higgs sector in the beyond standard model theories

Any extension of the standard model must respect the previous observations, a statement which can be simplified into a single parameter ρ_{EW}. It has been defined in terms of W and Z boson masses and the gauge couplings, but at the tree level, this parameter can be also written in terms of all scalar multiples ϕ_i:

$$\rho_{\mathrm{EW}} = \frac{M_{\mathrm{W}}^2}{M_{\mathrm{Z}}^2 \cos^2 \theta_{\mathrm{W}}} = \frac{\Sigma_{i=1}^{n}[T_i(T_i+1) - \frac{1}{4}Y_i^2]v_i}{\Sigma_{i=1}^{n}\frac{1}{2}Y_i^2 v_i}, \tag{2.1}$$

where T_i is the isospin, Y_i is the weak hypercharge, and v_i is the vacuum expectation value. The measured value of ρ_{EW} is extremely close to unity. [9]

As the parameter ρ_{EW} can be interpreted as an evidence of a theory's scalar structure, one can conclude that the simplest extension of the standard model includes either additional SU(2) doublets or singlets with hypercharges $Y = \pm 1$ and $Y = 0$, respectively, resulting in $T(T+1) = \frac{3}{4}Y^2$. As long as the experimental constraint $\rho_{\mathrm{EW}} \approx 1$ is respected, even more complex extensions are possible.

2.5.1 Two-Higgs-Doublet models

One of the most interesting extensions of the standard model are the two-Higgs-doublet models (2HDMs) that introduce two SU(2) doublets Φ_1 and Φ_2 with hy-

percharges $Y_1 = Y_2 = 1$, resulting in eight degrees of freedom [8, 9]. The vacuum expectation values of the two doublets are chosen as $v_1/\sqrt{2}$ and $v_2/\sqrt{2}$ in the spontaneous symmetry breaking. Moreover, the vacuum expectation values satisfy $v_1^2 + v_2^2 = v_{\mathrm{SM}}^2 \approx (246\,\mathrm{GeV})^2$. After the spontaneous symmetry breaking, five degrees of freedom remain as the physical states instead of a single Higgs boson: two neutral CP-even scalars (h, H), one CP-odd pseudoscalar A, and two charged Higgs bosons $\mathrm{H}^{\pm}$. Either of the CP-even scalars could explain the observed SM-like Higgs boson, but in this thesis the CP-even scalar h is taken as the SM-like state.

In 2HDMs, the couplings of the Higgs bosons to fermions and vector bosons do not only depend on the masses of fermions and vector bosons, but also on other parameters of the models that influence the production cross sections and decay branching ratios. One of the most important parameter of two-Higgs-doublet models is the ratio of the vacuum expectation values, also known as the $\tan\beta$ parameter:

$$\tan\beta = \frac{v_2}{v_1}. \tag{2.2}$$

The mixing angle α is another important parameter, defined for the CP-even scalars h and H. Together with the mixing angle, the parameter β determine the interactions between the Higgs fields and the fermions and vector bosons, offering a categorisation of possible types of 2HDMs. Most of the types give rise to tree level flavour-changing neutral currents (FCNC) that are not supported by the experimental data. Some types, however, introduce a symmetry that banish the FCNC.

The most studied and perhaps the most motivated model with natural flavour conservation is the type II 2HDM, mainly because the minimal supersymmetric standard model (MSSM) contains such a structure. The MSSM is a constrained version of the general type II 2HDM: the mass of the lightest Higgs boson has an upper bound, and the scalar self-couplings and the mixing parameter α are not arbitrary. The tree-level coupling constants of the fermions and the vector bosons with respect to the standard model couplings are shown in Table 2.1 for the type II

2HDM.

	Type II		
	h	H	A
up-type quarks	$\cos\alpha/\sin\beta$	$\sin\alpha/\sin\beta$	$\cot\beta$
down-type quarks and leptons	$-\sin\alpha/\cos\beta$	$\cos\beta/\sin\beta$	$\tan\beta$
vector bosons (W or Z)	$\sin(\beta-\alpha)$	$\cos(\alpha-\beta)$	-

Table 2.1: The tree-level couplings of the fermions and vector bosons to the CP-even (h and H) and CP-odd (A) Higgs bosons in the type II 2HDMs, normalized to the SM couplings. [9]

The measured mass and properties of the SM-like Higgs boson may offer an experimental handle to the parameter space of MSSM, depending on the chosen benchmark scenario. Some parts of the parameter space of a scenario may be immediately excluded by the observed value of 125 GeV. Searches for the four other Higgs bosons can help to constrain the rest of the parameter space. The interesting regions of the parameter space do not only depend on the measured mass of the SM-like Higgs boson, but other parameters of the benchmark scenario, for example the value of m_{A} and $\tan\beta$: the h boson couplings are only similar to the SM couplings at the decoupling or alignment limit. At the decoupling limit the mass difference between the lightest Higgs boson and the other Higgs bosons is large ($m_{\mathrm{h}} \ll m_{\mathrm{A}}, m_{\mathrm{H}}, m_{\mathrm{H}^{\pm}}$), whereas at the alignment limit the couplings of the h boson are strictly those of the SM Higgs boson ($\sin(\beta-\alpha)=1$). This further constrains experimental searches for the additional Higgs bosons.

Previous searches have excluded a large part of the high $\tan\beta$ region (see e.g. Ref. [39, 40]), which encourages us to concentrate on the part of the parameter space with low $\tan\beta$ values. Typical MSSM benchmark scenarios do not allow $m_h \sim 125$ GeV for low $\tan\beta$ values as the radiative corrections depend logarithmically on the SUSY-breaking scale, which is usually set to $\mathcal{O}(1\,\mathrm{TeV})$. However, some benchmark scenarios can accommodate $m_h \sim 125\,\mathrm{GeV}$ even in the region with low $\tan\beta$ values.

Two such MSSM benchmark scenarios are called hMSSM [11–14] and low-tb-high [15]. In the hMSSM scenario, the dominant radiative corrections to the Higgs boson masses become fixed by requiring $m_{\mathrm{h}} = 125\,\mathrm{GeV}$. As a result, the masses and couplings of the other Higgs bosons are determined, and the parameters $\tan\beta$ and m_{A} can describe the Higgs sector to a good approximation. The low-tb-high scenario relies on resumming the large radiative corrections using a standard model effective field theory framework in order to derive the Higgs sector predictions. Tuning the supersymmetric parameters yield the observed value of m_{h} across most of the m_{A}–$\tan\beta$ plane. In the low-tb-high scenario, the SUSY-breaking scale can be up to $\mathcal{O}(100\,\mathrm{TeV})$ for small values of m_{A} and $\tan\beta$. Recent developments on the MSSM benchmark scenarios concluded that a correct resummation of the large radiative corrections would require a 2HDM effective field theory framework, which in turn produces $m_{\mathrm{h}} < 125\,\mathrm{GeV}$ in most of the parameter space of the low-tb-high scenario [41]. An alternative scenario called $\mathrm{M}_{\mathrm{h,EFT}}^{125}$ [41] was proposed to solve the known flaw of the low-tb-high scenario. It uses the 2HDM effective field theory framework with a supersymmetric mass scale that can reach up to $10^{16}\,\mathrm{GeV}$, and produces the observed value of m_{h} in the majority of the m_{A}–$\tan\beta$ plane. At the time of writing, the necessary tools to produce the interpretation of results in the $\mathrm{M}_{\mathrm{h,EFT}}^{125}$ scenario were unavailable, and thus the low-tb-high scenario was included in the interpretation of the results, discussed more in detail in Section 7.[1]

The parameter space of each scenario defines how the additional Higgs bosons are produced in proton-proton collisions, and the branching fraction of each decay mode can vary greatly. Thus, the process utilised in a search for physics of 2HDMs must be selected based on what part of the parameter space is targeted. To study the region with low $\tan\beta$ values, it is instrumental to choose a process that is the most

[1] *Shortly after this thesis was finalised, the necessary tools were released. I utilised the* $\mathrm{M}_{h,\mathrm{EFT}}^{125}$ *scenario instead of the low-tb-high scenario to interpret the results of the corresponding search submitted for publication by the CMS Collaboration [1].*

optimal for constraining this region. At time of writing, more extensive studies on the hMSSM scenario were publicly available compared to the low-tb-high scenario. For this reason, the following subsection describes the details of the production and decay of the additional Higgs bosons in the hMSSM scenario.

2.5.2 Production and decay of the additional Higgs bosons in the context of hMSSM

The theoretical predictions imply that especially the heavier neutral Higgs bosons H and A have sizeable branching fractions into final states with at least one h boson at low $\tan\beta$ region as shown in Fig. 2.3. The process $\mathrm{H} \to \mathrm{hh}$ has higher branching fractions at higher masses compared to the $\mathrm{A} \to \mathrm{Zh}$ decay, which in turn can be used to reach larger $\tan\beta$ values when the mass of the pseudoscalar A is below 240 GeV. When the mass of the heavier Higgs boson exceeds $2m_t$, the decay into two top quark starts to dominate as also demonstrated in Fig. 2.3. This decay channel, however, is not experimentally "pure" due to high background contributions from the standard model production of top quark pair.

Similarly to the branching fractions, the production processes of the heavy neutral Higgs bosons depend on the value of $\tan\beta$. Two production processes dominate the parameter space; the gluon fusion and the $\mathrm{b\bar{b}}$ associated production. As shown in Fig. 2.4, in the hMSSM scenario the heavy neutral Higgs bosons are mainly produced by the gluon fusion production ($\mathrm{gg} \to \mathrm{A/H}$) process in the low $\tan\beta$ region. The $\mathrm{b\bar{b}}$ associated production ($\mathrm{b\bar{b}A/H}$) has similar cross sections to those of the gluon fusion production process in the high $\tan\beta$ region. Moreover, in the region with low $\tan\beta$ values, the gluon fusion production cross sections are larger for the A boson than for the H boson. For the high $\tan\beta$ values the differences in the cross sections are smaller both in the case of gluon fusion and the $\mathrm{b\bar{b}}$ associated production.

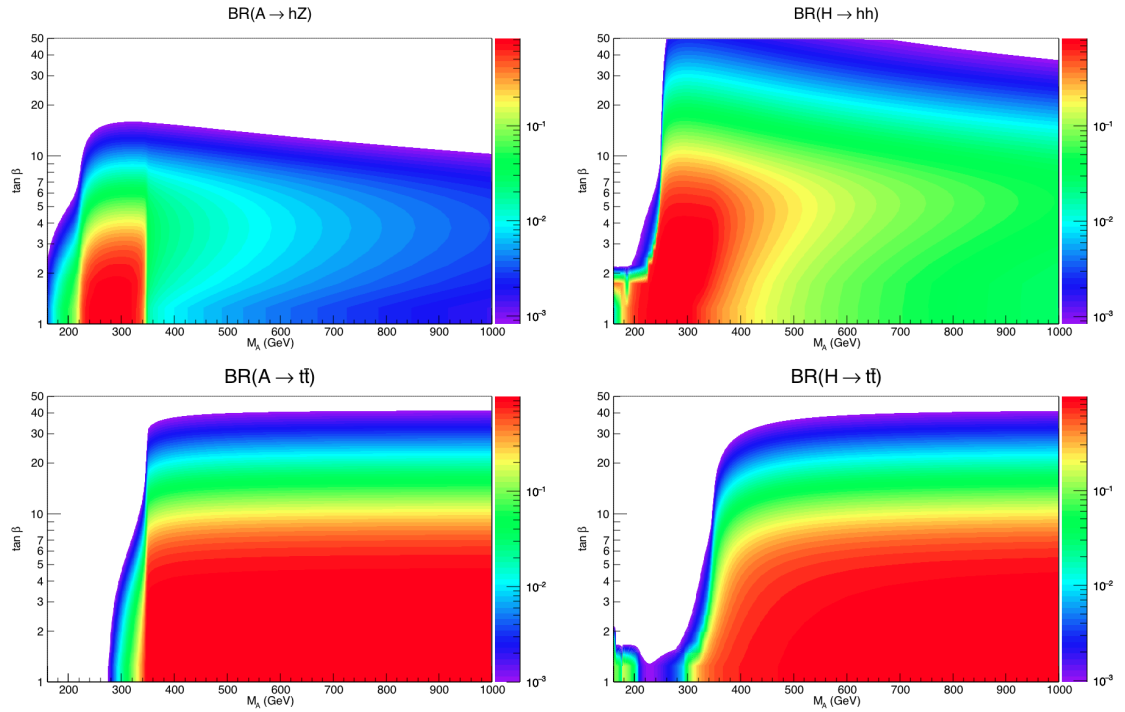

Figure 2.3: Branching fractions for the heavier Higgs bosons A and H in the hMSSM scenario with the constraint $m_h = 125$ GeV: A $\to$ hZ (top left), H $\to$ hh (top right), A $\to$ t$\bar{\text{t}}$ (bottom left), and H $\to$ t$\bar{\text{t}}$ (bottom right). [14]

Combining the information from predictions both for the branching franctions and cross sections, it becomes clear that at low $\tan\beta$ values it is preferred to search for the pseudoscalar boson A produced primarily in the gluon fusion, decaying into a h boson ($m_{\text{h}} = 125\,\text{GeV}$) and a Z boson. The contribution from the associated production with b quarks depends on the sensitivity of the analysis, and should not be fully neglected. The Feynman diagrams for both production processes are shown in Fig. 2.5.

The signatures of this channel can be experimentally easily accessible: one can consider the Z decays only into two light leptons (electrons, muons), and we can choose to study the Higgs boson decays with reasonable branching fractions. As already discussed in Section 2.4, the SM Higgs boson decay into two tau lepton offers a clean signature. Considering both leptonic and hadronic tau decays excluding the

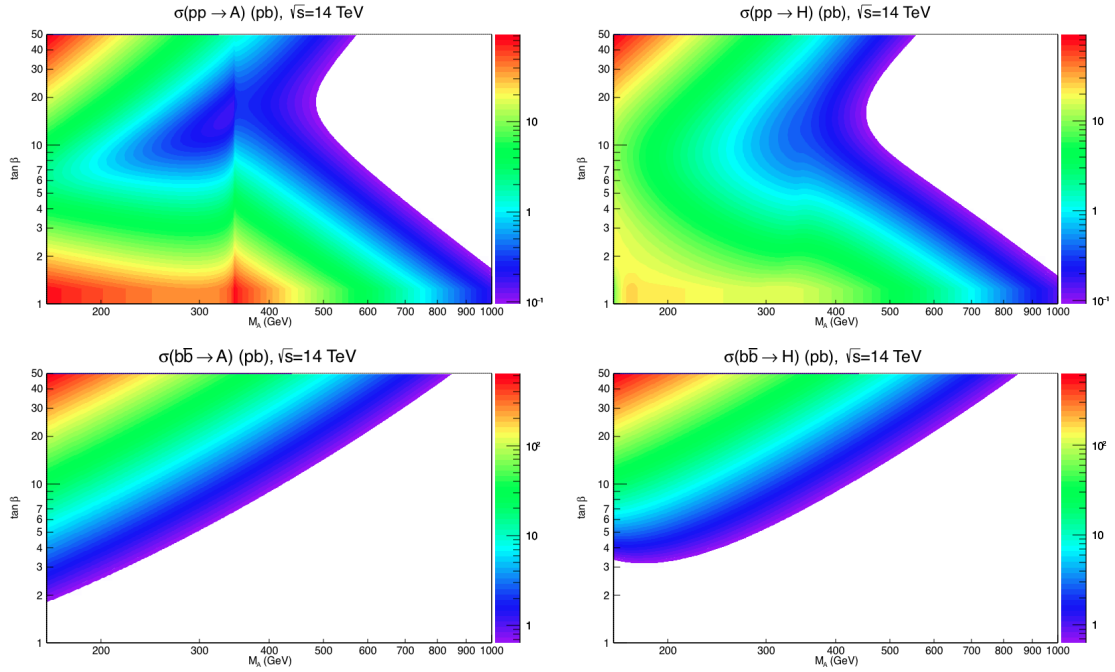

Figure 2.4: Cross sections for the heavier Higgs bosons A and H in the hMSSM scenario at $\sqrt{s} = 14\,\text{TeV}$: gluon fusion production of A (top left) and H (top right), and the $b\bar{b}$ associated production of A (bottom left), and H (bottom right). In the figure titles "pp → A/H" and "$b\bar{b}$ → A/H" denote "gg → A/H" and "$b\bar{b}$A/H", respectively. [14]

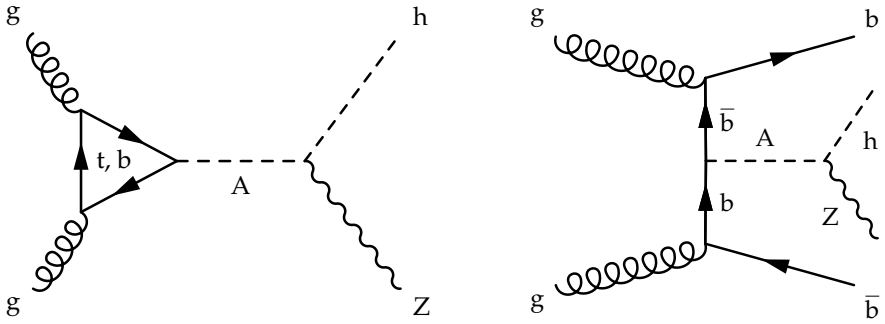

Figure 2.5: Feynman diagrams for two dominant production processes for the pseudoscalar A boson: gluon fusion (left) and associated production with b quarks (right). In both cases the A boson decays into a 125 GeV Higgs boson and a Z boson.

final states with two muons or electrons, one can distinguish possible signal from the background contributions more feasibly. Thus, the process primarily considered

in this thesis is gg $\rightarrow$ A $\rightarrow$ Zh $\rightarrow \ell\ell\tau\tau$. The corresponding Feynman diagram is presented in Fig. 2.6. The same final state is chosen also for constraining the m_{A}–tan β plane in the low-tb-high scenario, in which the branching fractions of the A $\rightarrow$ Zh and H $\rightarrow$ hh decays are similar to those of hMSSM scenario [15].

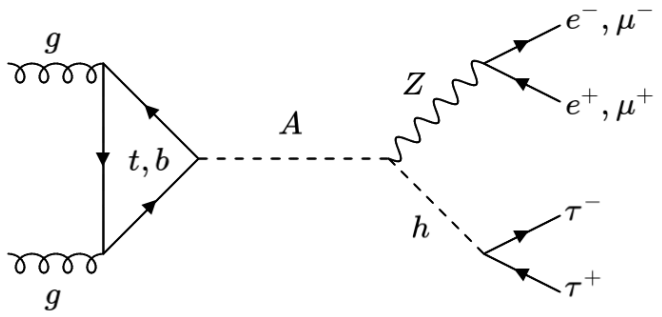

Figure 2.6: Feynman diagram for the process primarily studied in this thesis: gg $\rightarrow$ A $\rightarrow$ Zh $\rightarrow$ $\ell\ell\tau\tau$.

2.5.3 Previous searches and studied MSSM scenarios

As discussed in Section 2.5.1, the parameter space of 2HDMs is described by two parameters, tan β and m_{A}. The results of searches for additional Higgs bosons are interpreted in different MSSM scenarios, yielding an exclusion plot in the m_{A}–tan β plane for each scenario. Alternatively, the model-dependent upper limits are given in the $\cos(\beta-\alpha)$–tan β plane. In this subsection, I will give a brief review of results for the low tan β region, produced in the context of the hMSSM and low-tb-high scenarios that are studied in this thesis.

Previous searches covering the studied process (A $\rightarrow$ Zh $\rightarrow \ell\ell\tau\tau$) have been performed by the ATLAS and CMS Collaborations using pp collisions data collected at $\sqrt{s} = 8$ TeV [42, 43]. Model-independent, and model-dependent limits in the context of 2HDMs, were set by these analyses. The CMS Collaboration also interpreted

the results in the low-tb-high scenario discussed in Section 2.5.2: the observed (expected) limits excluded $\tan\beta$ values up to 2.7 (2.4) at $m_{\mathrm{A}} = 300\,\mathrm{GeV}$. Searches for the A boson decaying into Zh, have also been performed in final states containing a pair of bottom quarks from the h boson decay, by the ATLAS and CMS Collaborations in pp collisions at $\sqrt{s} = 13\,\mathrm{TeV}$ [44, 45]. These analyses studied the generic type-II 2HDMs, and produced model-dependent limits both in the m_{A}–$\tan\beta$ and $\cos(\beta-\alpha)$–$\tan\beta$ planes.

The hMSSM scenario, also described in Section 2.5.2, has not been studied by the previous analyses targeting the $\mathrm{A} \to \mathrm{Zh}$ decay channel. However, the region with lower $\tan\beta$ values has been explored by the CMS experiment using other decay channels, namely $\mathrm{H} \to \mathrm{hh} \to \mathrm{b\bar{b}}\tau\tau$, $\mathrm{A/H} \to \mathrm{t\bar{t}}$, and $\mathrm{H} \to \mathrm{WW}$, in pp collisions at $\sqrt{s} = 13\,\mathrm{TeV}$. The observed (expected) limits for the $\mathrm{H} \to \mathrm{hh} \to \mathrm{b\bar{b}}\tau\tau$ decay channel excluded $\tan\beta$ values up to 1.9 (1.7) at $m_{\mathrm{A}} = 300\,\mathrm{GeV}$, and covered m_{A} values between 230 and 360 GeV with the observed limits [46]. The $\mathrm{A/H} \to \mathrm{t\bar{t}}$ decay channel was used to study m_{A} values between 400 and 700 GeV, and the observed (expected) limits excluded $\tan\beta$ values up to 1.7 (2.5) [47]. The analysis targeting the $\mathrm{H} \to \mathrm{WW}$ decay channel covered m_{A} values between 130 and 390 GeV, and the highest $\tan\beta$ value excluded by the observed (expected) limits was 10 (9) at $m_{\mathrm{A}} = 155\ (165)\,\mathrm{GeV}$ [48]. Beyond $m_{\mathrm{A}} = 220\,\mathrm{GeV}$ where the $\mathrm{A} \to \mathrm{Zh}$ decay has a sizeable branching fraction, the observed (expected) limits exclude $\tan\beta$ values below 3.5 (4.5).

3. Experimental setup

In this chapter the experimental setup used for both precision measurements and searches for new physics are described, including the principles behind accelerator physics, and how to study the collisions.

3.1 Concepts of particle acceleration and collisions

Particle accelerators use either static electric or changing electromagnetic fields to accelerate a beam of particles grouped into so-called bunches, and magnets are used to steer and focus the beam. In collider accelerators each beam consists of multiple bunches, and the colliding beams are being accelerated in opposite directions and directed against each other to produce collisions.

In the collision the energy of the colliding particles can produce particles through a process with a probability proportional to the cross section $\sigma_{process}$. Depending on the process, the cross section can either increase or decrease as a function of the center-of-mass energy $\sqrt{s}$, and it also depends on the type of the colliding particles. As such, increasing the center-of-mass energy is not a straightforward solution to produce more (hypothetical) particles of interest.

To maximise the number of collisions and thus to produce higher amount of possibly interesting processes, one must squeeze the particles in each bunch as close

as possible to each other. To understand how many of the particles in each bunch might collide, we define *instantaneous luminosity* $\mathcal{L}_{inst}$ to describe the particle flux traversing through an area per second as follows:

$$\mathcal{L}_{inst} = f\frac{N^2 N_b}{4\pi\sigma_x\sigma_y}, \tag{3.1}$$

where f is the rotation frequency, N is the number of particles in each bunch of the colliding beams, N_b is the number of bunches, and $\sigma_{x,y}$ are the root-mean-square widths of the bunches in x and y directions. [49]

The expected number of events from a certain process is obtained by first integrating $\mathcal{L}_{inst}$ over time to obtain the integrated luminosity $\mathcal{L}_{int}$, and finally multiplying it with the cross section of the process:

$$N_{expected} = \int \mathcal{L}_{inst}\ dt\sigma_{process} = \mathcal{L}_{int}\sigma_{process}. \tag{3.2}$$

As mentioned above, the cross section also depend on the colliding particles, and in general it is more feasible to try to increase the integrated luminosity over the cross section to increase the expected number of events from an interesting process. [49]

When searching for new physics, in our case a pseudoscalar A produced in gluon fusion, it becomes apparent that using proton-proton collisions to produce this hypothetical particle is the only reasonable approach considering the currently available particle accelerators. However, in the proton-proton collisions the colliding particles are in fact quarks and gluons that carry a fraction of the proton's momentum. As a result, the produced particles are boosted in the beam direction, i.e. the z-axis.

A commonly used variable *rapidity* transforms additively under longitudinal Lorentz transformations, making it more simple to study under such boosts. Rapidity is defined in terms of the projection of the momentum along the beam axis (p_z) and the energy of the particle (E):

$$y = \frac{1}{2}\ln\frac{(E+p_z)}{(E-p_z)}. \tag{3.3}$$

As often the momentum of the produced particle is greater than its mass ($p >> m$), an approximation of rapidity, called pseudorapidity, is defined:

$$\eta = -\ln\left(\tan\frac{\theta}{2}\right), \tag{3.4}$$

where θ is the angle between the total momentum 3-vector $\mathbf{p}$ and the momentum along the beam axis p_z. To account for the component of the momentum perpendicular to the beam axis, we define *transverse momentum* $p_{\mathrm{T}} = \sqrt{p_x^2 + p_y^2}$. [50]

3.2 The Large Hadron Collider and proton-proton collisions

The Large Hadron Collider (LHC) [51] is the world's largest particle accelerator with a circumference of 27 kilometers. LHC is located at CERN on the border between France and Switzerland near Geneva, and has been designed to collide proton beams with $\sqrt{s} = 14\,\mathrm{TeV}$ and an instantaneous luminosity of 10^{34} $\mathrm{cm}^{-2}\mathrm{s}^{-1}$. During the Run I (2009-2013), the highest center-of-mass energy was $\sqrt{s} = 8\,\mathrm{TeV}$, and during the Run II (2015-2018) a center-of-mass energy of $\sqrt{s} = 13\,\mathrm{TeV}$ was achieved. In addition to proton collisions, heavy-ion beams are collided, yet with smaller center-of-mass energy of 5 TeV per nucleon pair.

To collide protons and reach these world-record energies, the beams must be first created and then accelerated in steps. Everything starts by producing the protons out of hydrogen gas. Before sending the protons to LHC, the protons are accelerated to energy of 450 GeV using the pre-accelerator chain that consists of four parts: Linac2, the Proton Synchrotron Booster (PSB), the Proton Synchrotron (PS), and the Super Proton Synchrotron (SPS). The LHC accelerator complex is shown in Fig. 3.1.

LHC uses 16 radiofrequency (RF) cavities to accelerate the protons to target energies. Dipole and quadrupole magnets bend and squeeze the protons while they

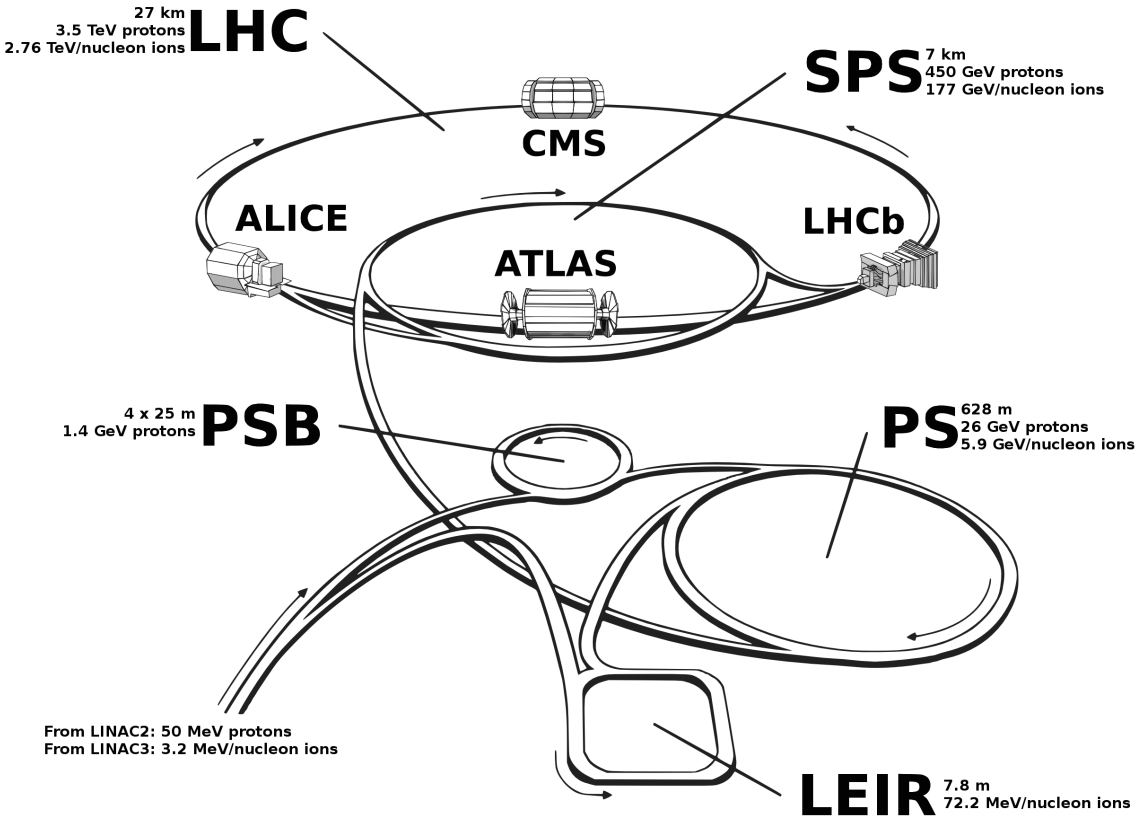

Figure 3.1: A sketch of the LHC accelerator complex and its four largest experiments. [52]

travel within LHC. There are also so-called inner triples that tighten the beams before collisions. The inner triplets are located at each of the four collision points before and after the largest experiments: ATLAS (A Toroidal LHC Apparatus), CMS (Compact Muon Solenoid), ALICE (A Large Ion Collider Experiment), LHC-b (LHC-beauty).

In total seven experiments record the output of collisions. Additionally to ATLAS, CMS, ALICE, and LHCb there are TOTEM (TOTal, Elastic and diffractive cross-section Measurement), LHC-f (LHC-forward) and MoEDAL (Monopole and Exotics Detector At the LHC).

ATLAS and CMS are general-purpose detectors, built in different ways but both designed to investigate similar phenomenon of physics. In addition to studying physics within the standard model, such as the Higgs boson, they search for possible

extensions to the standard model. At the same interaction point as ATLAS there is LHCf that is designed to measure hadronic cross sections in the kinematic regime useful for cosmic ray models. Similarly CMS shares the interaction point with another experiment, TOTEM, designed to measure the total cross section but also elastic scattering and diffractive processes. ALICE is built to investigate the quark-gluon plasma using heavy-ion collisions, whereas LHCb is designed to examine the interactions of b-hadrons. MoEDAL, located close to LHCb, is built to search for the magnetic monopole and other highly ionizing stable massive particles. The data analysed in this thesis was collected using CMS.

During the full Run 2, the LHC delivered $\sim$163 fb^{-1} of proton-proton collisions, and the CMS experiment recorded $\sim$150 fb^{-1}, as illustrated in Fig. 3.2. The same figure shows also the proton-proton collisions delivered by the LHC during the individual data taking years 2015–2018. The data taking efficiency of the CMS experiment was 92.3%, which is a great achievement considering the data taking conditions were more extreme than those for which the CMS experiment had been designed. [53]

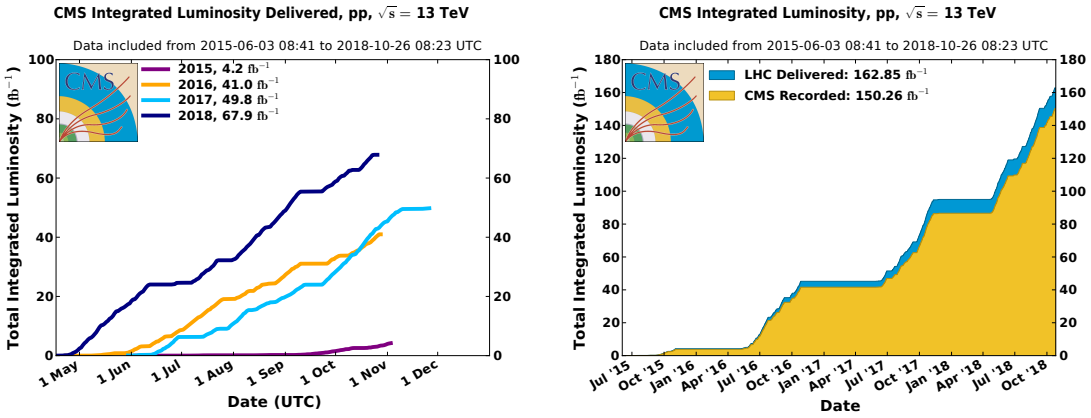

Figure 3.2: Left: Delivered luminosity separately for the data taking years 2015–2018. Right: Cumulative delivered and recorded luminosity for the full Run 2. Both figures show proton-proton collision data only. [53]

The design instantaneous luminosity was exceeded by a factor of two when the instantaneous luminosity reached 20.7 Hz/nb ($2.07 \cdot 10^{34}$ cm^{-2}s^{-1}) in 2017, and in 2018 the peak luminosity delivered was 21.4 Hz/nb ($2.14 \cdot 10^{34}$ cm^{-2}s^{-1}). Moreover, the number of simultaneous inelastic collisions per crossing (pileup, PU) was large compared to the value expected at the design luminosity (∼20); in 2018 the PU averaged 55 at the beginning of each fill. The delivered peak luminosities and average pileup for each data taking year (2015–2018) are shown in Fig. 3.3.

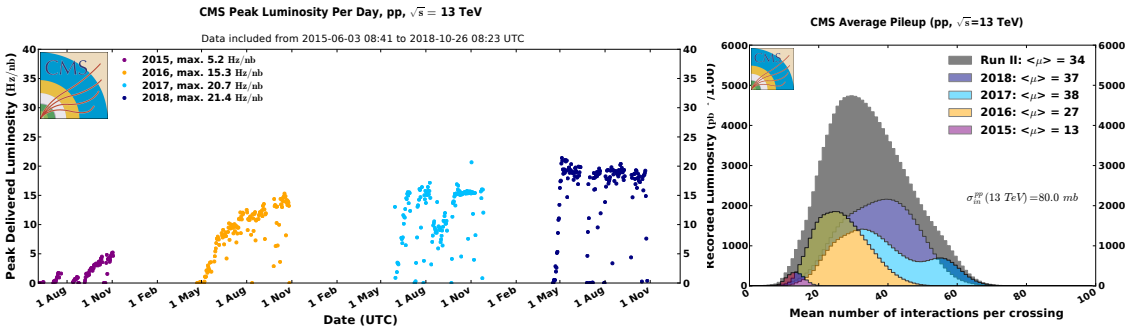

Figure 3.3: Left: Peak luminosity delivered to CMS during stable beams of proton-proton collisions during the data taking years 2015–2018. The design luminosity of LHC is 10^{34} cm^{-2}s^{-1}. Right: The pileup recorded at the CMS experiment separately for the years 2015–2018 and the full Run 2. The overall mean values are shown in the legend. The minimum bias cross section is taken from theoretical prediction. [53]

3.3 The Compact Muon Solenoid

The CMS apparatus [54] is the second largest experiment at the LHC, and its central feature is a powerful superconducting solenoid that offers a magnetic field of 3.8 T to curve each particle's path depending on the charge of the particle. Concentric layers of particle detectors - each made to target specific particles - are placed both inside and outside of the solenoid. The total weight of the CMS experiment is approximately 14000 tonnes. The onion-like structure of the CMS detector enables precise measurements of the properties of produced particles, which is invaluable

information for physics analyses.

The general structure of the CMS experiment is shown in Fig. 3.4. After the collision point there are silicon pixel and strip trackers, followed by a lead tungstate crystal electromagnetic calorimeter (ECAL), and a brass and scintillator hadron calorimeter (HCAL), each composed of a barrel and two endcap sections. The pseudorapidity (η) coverage provided by the barrel and endcap detectors is further extended by the forward calorimeters. Outside the solenoid, gas-ionisation chambers are embedded in the steel flux-return yoke for muon detection. Two-tiered trigger system is used to select events of interest.

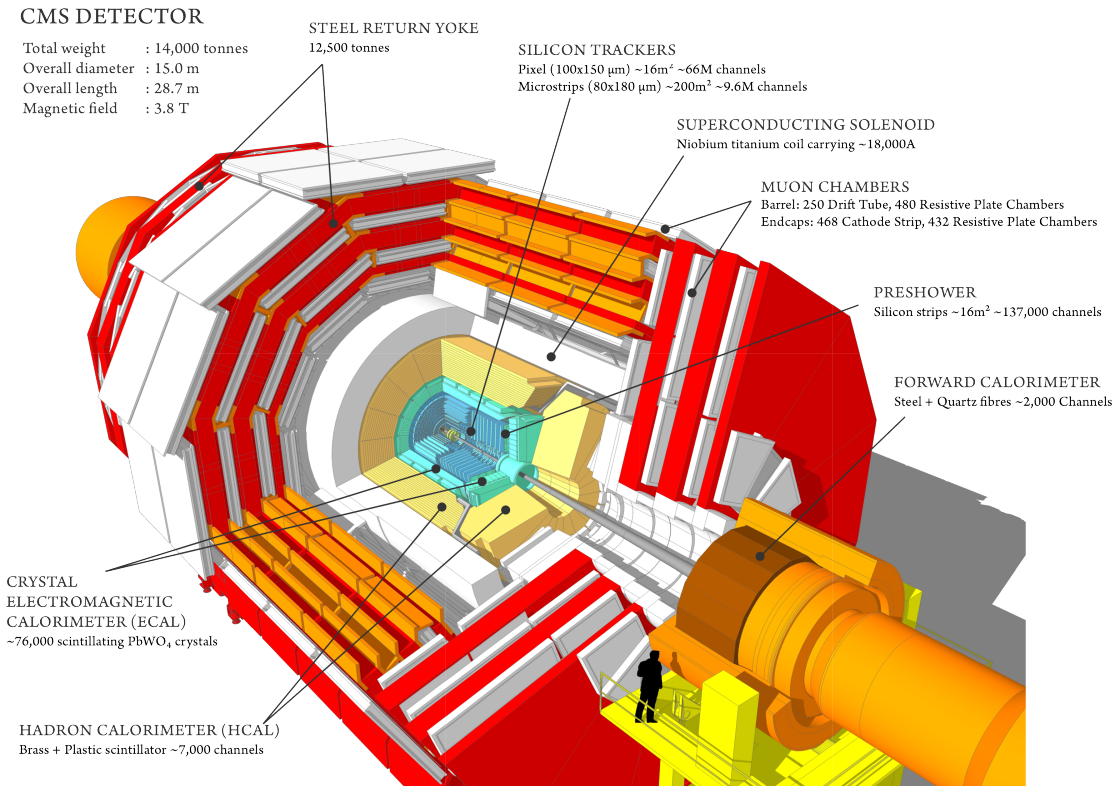

Figure 3.4: A sectional view of the subsystems of the CMS detector. [55]

A coordinate system of CMS origins in the interaction point, the z-axis is selected parallel to the beam line with its direction counter-clockwise along the proton beam. The y-axis points upwards, and the x-axis towards the center of the

LHC ring. Cylindrical coordinate system is preferred: the polar angle θ is defined using the z-axis, whereas the azimuthal angle ϕ is based on the x-y plane. A sketch of the coordinate system can be seen in Fig. 3.5.

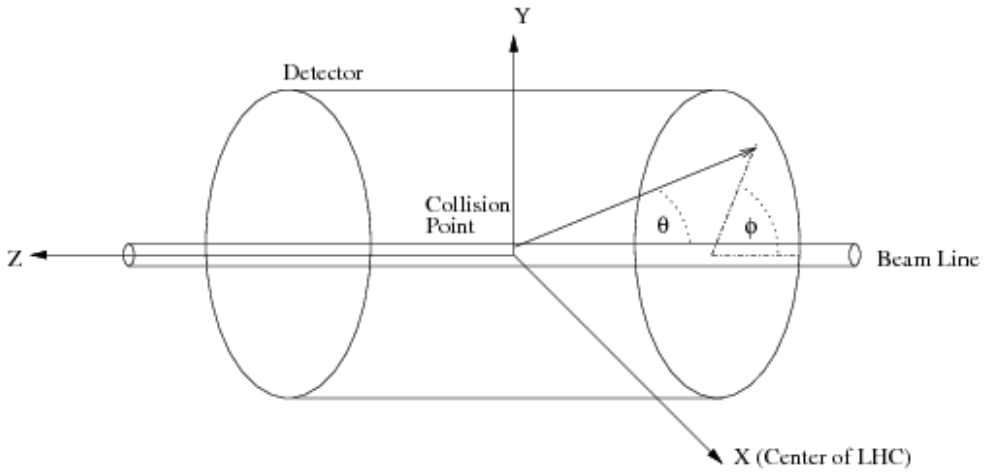

Figure 3.5: The coordinate system of the CMS experiment. [56]

3.3.1 Tracking

The pixel and strip trackers form the tracking system [54, 57] of the CMS detector, which is shown in Fig. 3.6. The tracking system reaches from the interaction point up to 1.1 m and offers acceptance up to a pseudorapidity of $|\eta| < 2.5$. High granularity combined with radiation hardness is achieved using silicon with a total area of about $199\,\mathrm{m}^2$.

The CMS tracking system has 1440 pixel detector modules, covering an area of $\sim 1.1\,\mathrm{m}^2$. The detector modules are placed in three barrel layers (BPix) at radii between 4.4 cm and 10.2 cm, and two forward disks (FPix) extending from 6 cm and 15 cm [54]. BPix has in total 48 million pixels, whereas the number of channels in FPix is 18 million. During the upgrade done in 2017, a fourth barrel layer and third endcap disk were included [58, 59]. After the upgrade, the first tracking layer is at radii 2.9 cm instead of 4.4 cm. As the data analysed in this thesis was collected

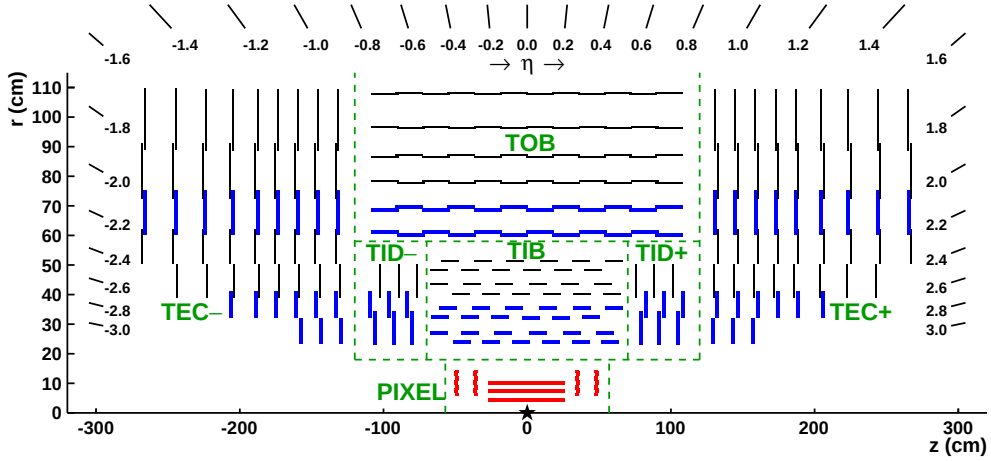

Figure 3.6: A sketch of the tracking system used in the CMS experiment. Only a positive side of the tracking system is shown. [57]

during the year 2016, we will describe any further details on the pixel tracker as it was during the data taking, i.e. before the upgrade.

A single hit resolution of as precise as $10\,\mu$m can be achieved in the $r-\phi$ direction, whereas in the z-direction the resolution is $20\,\mu$m. The reconstruction of secondary vertices from e.g. tau lepton decay relies mostly on the pixel tracker, and benefits greatly from this resolution.

The second part of the tracking system, the strip tracker, covers the rest of the tracker area, i.e. $\sim 198\,\mathrm{m}^2$. The strip tracker consists of 9.3 million strips, divided within the three different subsystems: the tracker inner barrel and disks (TIB/TID) are closest to the interaction point, and are surrounded by the tracker outer barrel (TOB) that is complemented by the tracker endcaps (TECs).

The TIB and TID detectors reach 55 cm in radius, and are able measure up to 4 $r-\phi$ coordinates for each trajectory using 4 barrel layers and 3 disks at each end. The strip pitch is between 80 and $120\,\mu$m in TIB, whereas for TID the mean pitch is between 100 and $141\,\mu$m. The TOB detectors consist of 6 barrel layers that deliver 6 additional $r-\phi$ measurements. First 4 layers of TOB have the strip pitch

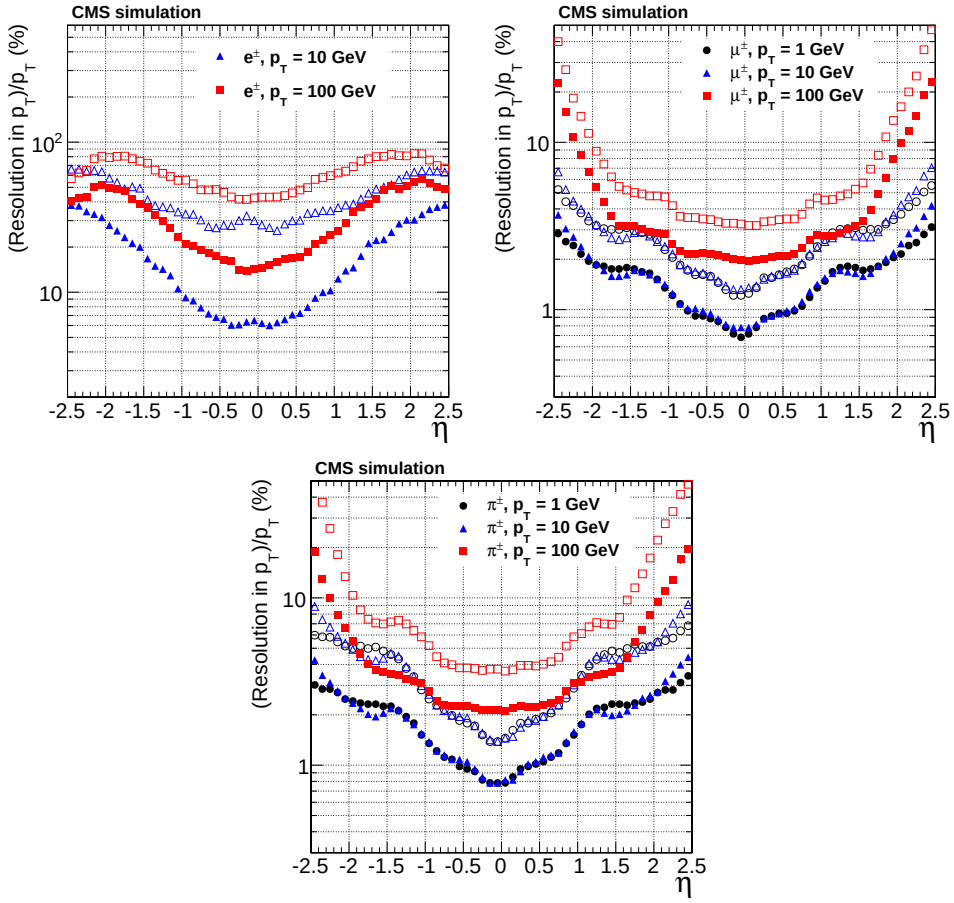

Figure 3.7: Tracking resolutions in transverse momentum over the full η range for electrons (top left), muons (top right), and charged hadrons (bottom). For electrons the GSF algorithm was used. [57]

of 183 μm, and the last two layers have the strip pitch of 122 μm. TIB, TID, and TOB reach up to $\pm$118 cm in z-direction, beyond of which TECs offer a coverage up to $\pm$282 cm. TECs reach in the r-direction up to $\pm$113.5 cm, and deliver up to 9 ϕ measurements per trajectory. The average pitch varies from 97 to 184 μm.

The tracking system of the CMS experiment provides a precise and efficient measurement of the trajectories of charged particles that were produced in the collision at the primary vertex. Extrapolating the trajectories also the secondary vertices from the decays of long-lived particles can be obtained. The track resolutions in transverse momentum are shown in Fig. 3.7 as a function of pseudo-

rapidity for isolated electrons, muons, and charged hadrons. In the search for $gg \rightarrow A \rightarrow Zh \rightarrow \ell\ell\tau\tau$, electrons and muons are required to have a transverse momentum of at least 10 GeV, whereas the reconstructed hadronic taus must pass $p_T > 20\,GeV$. In the barrel region for electrons with $p_T = 10\,GeV$ reconstructed with the GSF algorithm [60], a resolution of 10% is achieved. For charged hadrons from hadronic tau decays and muons the resolution is much better, less than 2% (3%) in the barrel region for transverse momenta of 10 GeV (100 GeV).

3.3.2 Calorimetric systems

The calorimetric system [54, 61] of the CMS apparatus measures the energy of the particles using two types of calorimeters: the electromagnetic calorimeter (ECAL) measures the energies of electrons and photons, whereas the hadron calorimeter (HCAL) collects the energy deposits from hadrons that are not fully contained by ECAL. When a particle passes a calorimeter, it interacts with the material, producing a cascade of shape and length depending on the particle type and energy. Secondary particles in the cascade produce light by scintillation in the ECAL and in the scintillator tiles of the HCAL. The amount of light produced is measured using photodiodes. Precise energy measurements provided by the calorimetric system are necessary for reconstruction of tau leptons that decay for example into electrons and neutral hadrons, but also for jet reconstruction, topics which are discussed more in detail in Section 4.3.

Electromagnetic calorimeter

One of the main goals of ECAL was to offer an excellent diphoton mass resolution of 1%, a crucial feature for Higgs boson searches in final states with two photons, which drove the choice of the material. The electromagnetic calorimeter is made of 75848 lead tungstate ($PbWO_4$) crystals, divided between two subdetectors: barrel

part of the ECAL (EB), and the endcap ECAL (EE). A sketch of the ECAL detector can be seen in Fig. 3.8.

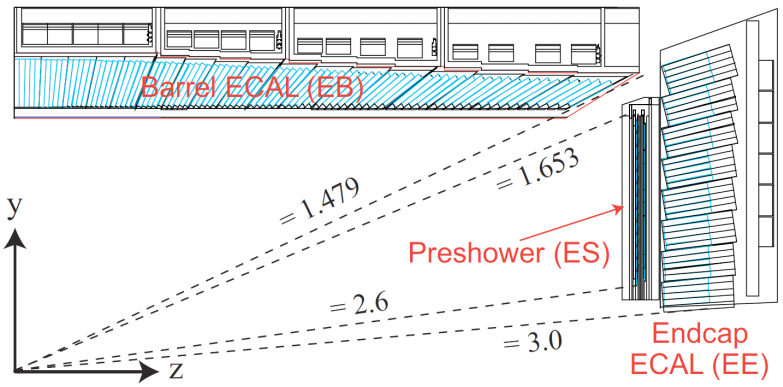

Figure 3.8: A view of the electromagnetic calorimeter of the CMS apparatus, showing its three subsystems: barrel ECAL, endcap ECAL, and the preshower ECAL. [62]

Lead tungstate crystals can offer fine granularity and compact size due to the material properties. It has high density (8.28 g/cm^3) translating to a compact detector, short radiation length of 0.89 cm and relatively small Moliére radius of 2.2 cm which translates into better position resolution as two Moliére radii contain 95% of the shower's energy deposit. The length of each crystal in the barrel is approximately 23 cm, and the cross section at the front face is approximately $22 \times 22\,\text{mm}^2$ (0.0174×0.0174 in $\eta - \phi$ plane), increased to $26 \times 26\,\text{mm}^2$ at the rear. The length corresponds to $25.8X_0$, where X_0 is the distance over which the electron loses 63% of its energy. In the endcap, the crystals are slightly shorter, with a length of 22 cm, corresponding to a radiation length of $24.7X_0$. The cross section at the front face is approximately $29 \times 29\,\text{mm}^2$, increased to $30 \times 30\,\text{mm}^2$ at the rear.

The EB detectors cover $|\eta|$ values up to 1.479, and the EE detectors complement the range from 1.479 to 3.0. When electrons and photons interact with the crystals, the lead tungstate scintillates producing an amount of light proportionally to the energy of the particle. The photodetectors used in the barrel region are avalanche photodiodes (APDs), whereas vacuum phototriodes (VPTs) are used in

the endcaps.

In front of the EE crystals there is a preshower detector (ES) covering the region $1.653 < |\eta| < 2.6$. The ES is a sampling calorimeter made of lead radiators and silicon sensors, and has a total thickness of 20 cm. At $\eta = 1.653$ the material thickness is $2X_0$ before the first sensor plane, and further $1X_0$ follows before reaching the second plane. The ES is designed to separate signals made by neutral pions from the ones made by one highly energetic photon. It also increases the spatial precision of position measurement of electrons and photons. The energy deposited in the preshower detector is added to the total energy from the lead tungstate crystals when reconstructing the energy of the shower.

The energy resolution is described by three terms: the stochastic, noise, and constant terms. The stochastic term includes contributions from event-to-event fluctuations in the shower containment, in the number of photoelectrons produced, and in the energy deposited. The noise term includes electronics, digitization, and pileup noise. Finally, the constant term is irreducible and mainly due to the non-uniformity of the longitudinal light collection. In the barrel, the energy resolution is found to be

$$\frac{\sigma_{\mathrm{E}}}{\mathrm{E}} = \frac{2.8\%}{\sqrt{\mathrm{E}}} \oplus \frac{12\%}{\mathrm{E}} \oplus 0.3\%, \tag{3.5}$$

where the first, second, and third terms are the stochastics, noise, and constant terms, respectively. Studies performed using the test beam showed that in the barrel the noise per channel is approximately 40 MeV in the highest gain range. Overall the energy resolution is found to be less than 1% for electrons with energy more than ~ 25 GeV.

Hadron calorimeter

To measure particles that cannot be stopped by the ECAL, e.g. long-lived neutral and charged hadrons, the hadronic calorimeter (HCAL) is used. HCAL is important

to improve the measurement of jets. Most of the hadron calorimeter is placed behind the electromagnetic calorimeter and before the magnet. The hadron calorimeter, shown in Fig. 3.9, is a sampling calorimeter that covers region up to $|\eta| < 5$ with four subdetectors: hadron calorimeter barrel (HB), hadron calorimeter endcaps (HE), outer hadron calorimeter (HO) and forward hadron calorimeter (HF). Due to the reduced space between the ECAL and magnet, HO is located after the magnet. For $|\eta| < 1.6$, the granularity of the calorimeters is 0.087×0.087 in the η–ϕ plane, whereas for $|\eta| \geq 1.6$ it is 0.17×0.17 in the η–ϕ plane.

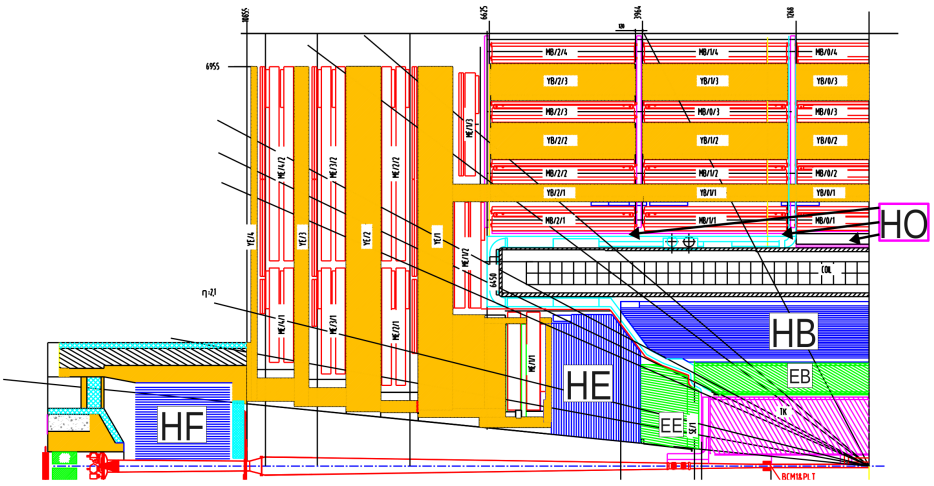

Figure 3.9: The hadron calorimeter subsystems shown in addition to the electromagnetic calorimeter. [63]

The hadron calorimeter barrel reaches up to $|\eta| < 1.3$, and it is made of flat brass absorber plates, divided in to two half-barrel sections HB− and HB+. In total HB consists of 36 identical azimuthal wedges. Plastic scintillators in 16η sectors produce the light, and Hybrid Photodiodes (HPDs) measure the light signals through the photoelectric effect. The interaction length λ_I is defined for hadronc in analogy with a radiation length, to account for the inelastic and elastic scattering experienced by the hadron. Interaction length is often longer than the radiation length. At $|\eta| \sim 0$ the thickness is only $5.39\lambda_I$, but it increases with $|\eta|$. At

$|\eta| = 1.3$ the thickness is $10.6\lambda_I$.

To extend the acceptance in η from 1.3 to 3.0, HE is placed after EE. As the resolution will be in any case reduced due to high pile up, and parton fragmentation, the aim was to minimise any dead areas between HB and HE rather than build a subdetector with high resolution for single particles.

As the barrel calorimeter is thinner than elsewhere at $|\eta| \sim 0$, many particles with higher transverse momentum are not brought to full stop. This causes the shower to "leak" outside the subdetector. To increase the thickness in the barrel region, the outer hadron calorimeter using the solenoid coil as an additional absorber is placed on top of the HB. It reaches up to $|\eta| < 1.3$ and increases the thickness to $11.8\lambda_I$.

The forward hadron calorimeter ($3 < |\eta| < 5.2$) captures most of the particle flux from the proton-proton interactions. While the other parts of the HCAL are exposed to in total 100 GeV per interaction, the two HF detectors receive 760 GeV per interaction. The flux is at its maximum at highest pseudorapidity. To face and stand the harsh conditions, the cylindrical forward hadron calorimeter was made of steel with a full interaction length of $\sim 10\lambda_I$. As a contrast to the rest of the detector, HF uses Cherenkov light from quartz fibres as an active material, that can survive the remarkable amount of radiation.

Due the different detector type, HCAL achieves much worse energy resolution than ECAL. When information from the barrel ECAL and HCAL are combined, the energy resolution for the total response from an isolated single particle (pion) becomes [64]

$$\frac{\sigma_{\mathrm{E}}}{\mathrm{E}} = \frac{110\%}{\sqrt{\mathrm{E(GeV)}}} \oplus 9\%. \tag{3.6}$$

For the forward hadron calorimeter the energy resolution [65] is much poorer, namely

$$\frac{\sigma_{\mathrm{E}}}{\mathrm{E}} = \frac{280\%}{\sqrt{\mathrm{E(GeV)}}} \oplus 11\%, \tag{3.7}$$

which is compensated due to the fact that in the forward region the ratio E/E_T is larger than in the barrel. Typical electronics noise in HCAL is measured to be approximately 200 MeV per tower.

3.3.3 Muon detectors

The muon detectors [54, 66] of the CMS experiment were built to fulfil three purposes. First and foremost, they need to identify muons. Second, the transverse momentum of muons must be measured, and lastly, the muon system must be included in the triggering. To follow the shape of the CMS experiment, the muon system was built to have cylindrical shape. It covers the range $|\eta| < 2.4$ and consists of three subsystems, as is shown in Fig. 3.10, all of them being gaseous detectors. The main working principle of the muon detectors is simple: the trespassing muon ionises the gas, resulting in electrons which are detected.

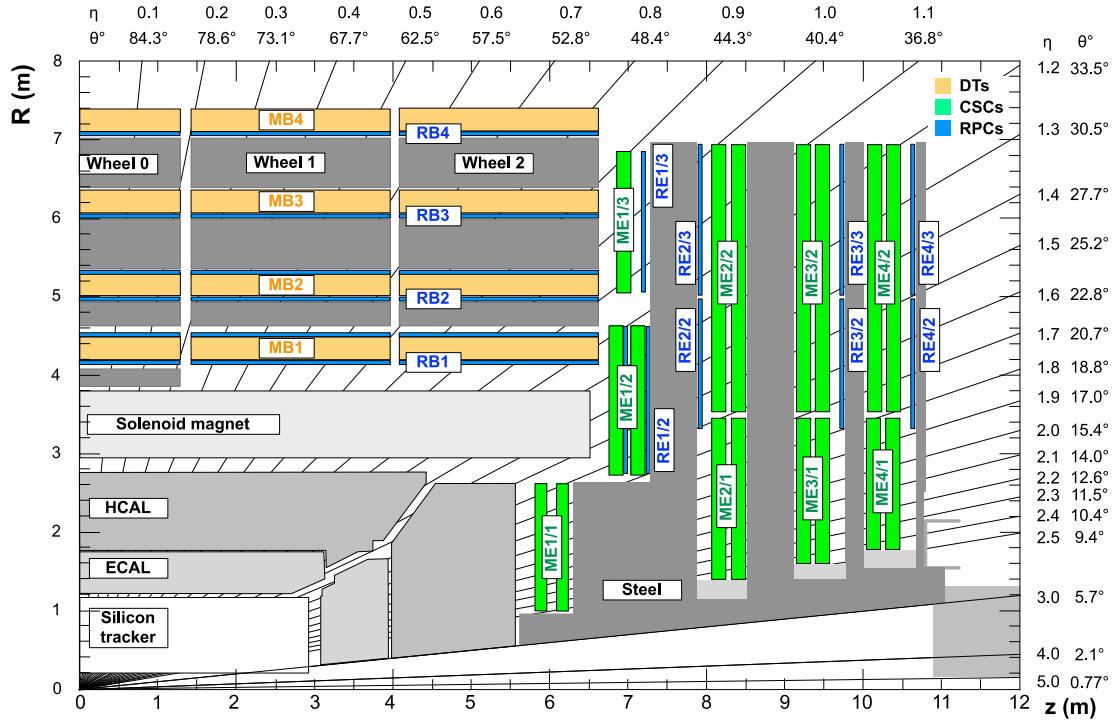

Figure 3.10: Overview of the CMS muon system. [66]

In the barrel region, up to $|\eta| < 1.2$, drift chambers (DTs) contained in the steel yoke are used. As the rate of muons and background is small, and the magnetic field is uniform, DTs serve also as a tracking system. The drift chambers determine the position of the trespassing muon by measuring the drift time of produced electrons to an anode wire of so-called drift cell. In total 172000 wires are contained in the DTs, divided into 250 chambers and four stations called "MBn", where n is the layer number (1-4). Each chamber consists of three "superlayers": two of these provide measurements of the position and bend along the ϕ coordinate, and one the θ measurement. As an exception, chambers in the fourth station (MB4) only have the two superlayers for the ϕ measurement. The drift chambers are filled with a gas mixture consisting of argon ($\sim$ 85%) and carbon dioxide ($\sim$ 15%), which determines the drift velocity of electrons produced by the traversing muons. The design resolution of 100 μm for each chamber is obtained when the pressure is kept at 1 atm and the amount of carbon dioxide is $10 - 20\%$. As a result, the DTs are made air-tight - any contamination from nitrogen affects both the timing and the spatial measurements. The designed single-hit resolution is 250 μm. In 2016, the designed single-hit resolution was achieved for all except the chamber MB4 due to the missing θ measurement. Starting from $|\eta| \sim 0.9$, DTs overlap with cathode strip chambers (CSCs) to avoid any dead areas that could cause inefficiencies in the identification and trigger.

The cathode strip chambers are multiwire proportional chambers with a cathode strip readout that offer a fast response time in addition to fine segmentation and resistance against radiation damage. The rates for muons and background are the highest in the endcap region, where the magnetic field is not uniform as a contrast to the barrel region. Moreover, the cathode strip chambers were used as they can function even if gas, temperature, or pressure is not controlled precisely. The area covered by the CSCs is $5000\,\mathrm{m}^2$, and requires more than $50\,\mathrm{m}^3$ of gas. The CSCs

are used both for measurement and triggering.

In total there are 540 CSC chambers in four stations (ME1-ME4) that cover the range $0.9 < |\eta| < 2.4$. Before Run 2, additional chambers were included to ME4. Each chamber includes six staggered layers, resulting in a position measurement in two coordinates. The cathode strips measure the position in $r - \phi$ coordinates, whereas the anode wires provide a measurement in r coordinate. The ME1/1 chambers offer a more precise spatial measurement (75 μm by design), whereas the 396 other chambers have a resolution below 150 μm.

The η region from 0.9 to 1.9 is equipped with resistive plate chambers (RPCs) to improve the triggering and the time and spatial resolution at high luminosities. RPCs are parallel-plate detectors that function in avalanche mode, and are thus sensitive to changes in temperature and pressure. Originally there were 4 RPC stations in the barrel (RB1-RB4) and 3 stations in the endcap (RE1-RE3), but for Run 2 a fourth endcap station RE4 was added. The number of channels is 480 (567) in the barrel (endcap). Each chamber includes 1 RPC layer, except RB1 and RB2 that have 2 layers. The resistive plate chambers achieve a time resolution of 3 ns, well below the time separation between two bunch crossings (25 ns), which benefits the time resolution. The spatial resolution for a chamber varies between 0.8 and 1.3 cm.

3.3.4 Trigger

The CMS experiments uses a two-tiered trigger system to select event of interest [67]. The hardware-based Level-1 (L1) trigger is the first part of the trigger system. It reduces the collision event rate of 40 MHz delivered by the LHC down to 100 kHz sent to the High Level Trigger (HLT) [68]. The output rate of the L1 trigger is strictly limited by the detector electronics, and cannot be exceeded. The average output rate of the HLT is 1 kHz, limited by the storage space. Foreseeing the challenging

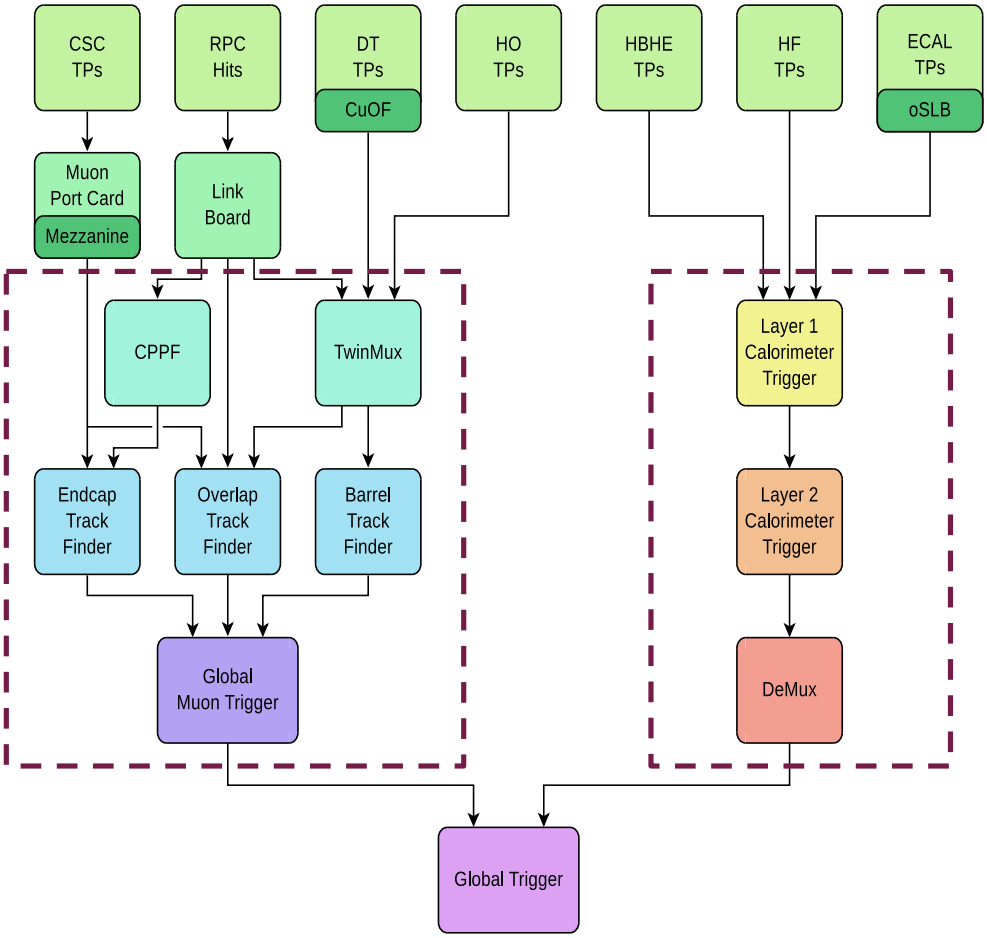

Figure 3.11: Full system of the upgraded CMS L1 trigger. The muon (calorimeter) trigger is shown with the dashed rectangle on the left (right) handside. The HCAL outer barrel part trigger primitives were never sent to the Twinmux as shown here. During the 2016 data taking, the RPC were sent only to the OMTF.

data taking conditions during Run II, the L1 trigger was fully upgraded in the beginning of 2016, and finalised during 2017. Without these changes, it would have been necessary to increase the trigger energy thresholds significantly as the total L1 trigger output rate of 100 kHz is required to be unchanged. Analyses relying on low-p_{T} objects would have naturally suffered from such changes. As the data used in this thesis was recorded in 2016, only the upgraded L1 trigger is described.

The upgraded Level-1 Trigger, shown in Fig. 3.11, receives input from muon systems (DT, RPC, CSC), and from the calorimeters (ECAL, HCAL, HF). The L1

trigger is divided into two parts, the muon and the calorimeter triggers, that both send data to the global trigger (GT). The L1 muon trigger consists of detector input pre-processors (the CPPF and TwinMux), three muon track finders (MTFs), and the global muon trigger (GMT). The calorimeter trigger includes three parts: layer-1, layer-2, and a de-multiplexing (Demux) node.

The trigger boards are custom-made electronic boards that follow the Micro Telecommunications Computing Architecture (μTCA) standard. A high performance stream processing board Master Processor 7 (MP7) [69] based on Virtex-7 field-programmable gate array (FPGA) is used in the GT, GMT, the barrel MTF, the layer-2 as well as the Demux. The overlap and encap MTF boards are based on Modular Track Finder 7 (MTF7) cards [70] using the same Virtex-7 FPGA. The layer-1, Twinmux, and CPPF each have a different design. Further details can be found in Ref. [68].

After the upgrade, an increased sensitivity and richer menu are offered by the global trigger as it can receive more candidate objects and allows at least twice as many algorithms as before (up to 512 algorithms instead of 128). Additionally, there is a possibility to add dedicated cross-triggers[1] adapted to the needs of each physics analysis group, and to implement sophisticated algorithms using correlation conditions.

The L1 muon trigger

The upgraded muon trigger combines hits from DT, RPC, and CSC, resulting in a more accurate transverse momentum calculation, increased efficiency, and much lower rates. This is achieved by using the muon track finders that are independent hardware trigger systems covering the barrel, overlap, and endcap regions. The

[1] A cross-trigger utilises different kinds of physics objects. For example, a cross-trigger can be exploited to select events with a muon and a electron.

MTFs perform the track reconstruction and p_{T} assignment using only the trigger primitives (TPs) that are track segments from the DT and CSC, and hits from the RPC. Depending on the track finder region, the CPPF and Twinmux prepare the trigger primitives for track reconstruction before they are sent to the muon track finders. Each MTF has 12 processors that are required to deliver three best track candidates, and as a result up to 36 track candidates per MTF can be forwarded to the GMT. The number of track candidates is limited by the number of available links in GMT.

All muons are sorted, and any duplicates are removed by the global muon trigger that sends up to eight muons to the GT. As inner tracker information is not used by the L1 trigger, variables sensitive to the measurement of the muon coordinates are not measured as precisely as in the offline reconstruction. Since 2017 the GMT also performs the extrapolation of the muon coordinates to the interaction region. The extrapolation relies on information on the muon p_{T}, η, and charge. Notable improvements are observed for example in the dimuon invariant mass resolution, a variable important in many physics programs.

The barrel muon track finder (BMTF) constructs muon tracks for the region $|\eta| < 0.83$. Each of the 12 BMTF sectors covers 30° in ϕ. First, the Twinmux combines DT track segments and RPC hits in each station into so-called super-primitives. During the 2016 data taking, only the DT track segments were sent to the TwinMux that forwarded the information to the BMTF. The BMTF uses the super-primitives, proceeding from the inner to the outer stations, and searches for compatible segments in an extrapolation window. The track candidate kinematics are based on the ϕ coordinate correlation between the stations, stored in Look-Up Tables (LUTs) implemented in FPGA.

The Twinmux forwards the DT data also to the overlap muon track finder (OMTF) that reaches from $|\eta| = 0.83$ to $|\eta| < 1.23$. Both positive and negative

η regions have 6 sectors (60° in ϕ). DT, RPC, and CSC trigger primitives are combined into single tracks by the OMTF using a Golden Pattern (GP) algorithm. The GP algorithm is based on comparing the hit pattern to a limited number of pre-computed hit patterns (GPs) that hold information about the bending distribution between each layer for a given muon p_{T}. A set of alternative muon p_{T} hypotheses can be obtained by testing each reference hit from different layers. The GP that best matches the hits will be chosen as the final result, and these track parameters are given for the track candidate. Finally, any duplicates are cleaned away.

Information from both CSC and RPC are sent to the endcap MTF (EMTF) once the CPPF has clustered and assigned coordinates (θ, ϕ) for the RPC hits. During the 2016 data taking, the RPC hits were not yet included in the EMTF. The EMTF covers the range $1.23 < |\eta| < 2.4$, using in total 12 sectors that each spand 60° in ϕ. Similarly to the OMTF, all track segments are compared to predefined patterns in a region. A potential track is declared if there are at least two stations with matches. The transverse momentum LUTs are used online to assign the track p_{T} based on 11 input variables. These LUTs were filled offline from a boosted decision tree (BDT), tabulating the output values for all possible input values. In order to store the LUTs, the EMTF has a special MTF7 with a fast and large (2 GB) memory.

The performance of the upgraded muon trigger is constantly monitored. The improvement due to the track extrapolation is demonstrated by the dimuon invariant mass distribution shown in Fig. 3.12. The latest results using data from 2017 showed that the muon trigger rates are reduced by 50% compared to the legacy trigger (2015) while achieving an improved data taking efficiency. The behaviour of the legacy trigger was based on an emulation in software, mimicking the function and performance of the hardware trigger system. These results can be seen in Fig. 3.13, shown for muons passing a p_{T} threshold of 25 GeV, the most common

trigger threshold used in the CMS experiment in 2017.

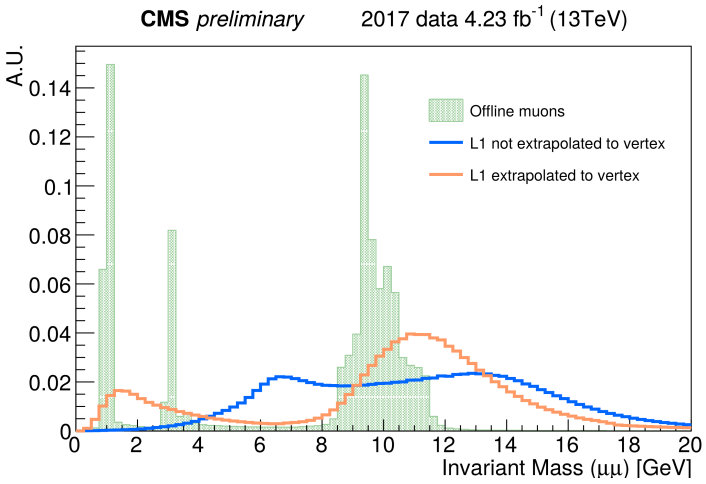

Figure 3.12: The effect of L1 track extrapolation to the vertex demonstrated through the invariant mass spectrum of two muons. The blue (orange) spectrum is made using two online muons without (with) the track extrapolation, displayed on top of the same spectra of two offline muons (green) [71]. Due to implementation of p_{T} offsets designed to make the L1 muon trigger 90% efficient at any given p_{T} threshold, the online spectrum appears shifted compared to the offline spectrum.

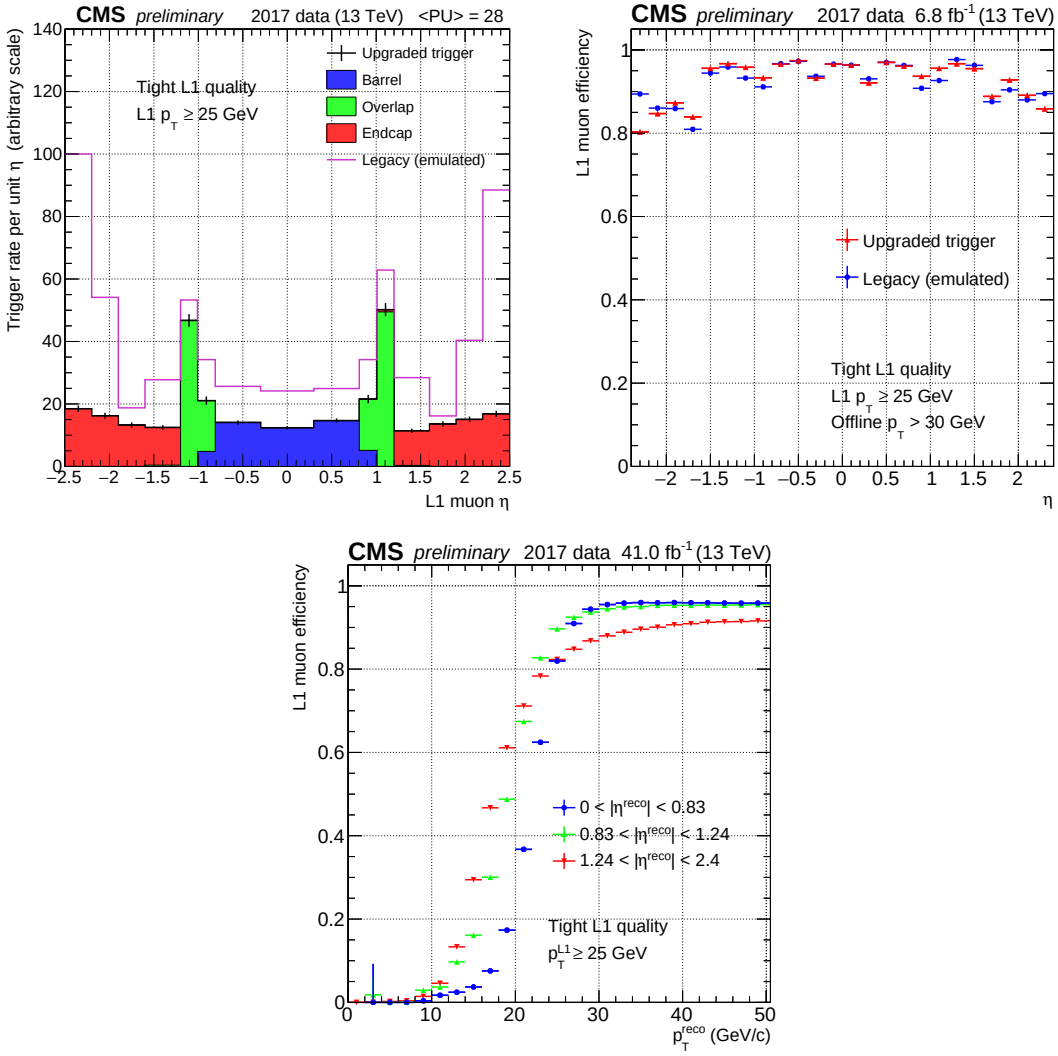

Figure 3.13: Performance of the upgraded L1 muon trigger during 2017, shown for muons passing a p_{T} threshold of 25 GeV. Top left: Trigger rate as a function of muon η, shown for muons built by the three track finders (barrel, overlap, and endcap) in the upgraded L1 muon trigger (2017), and compared with the emulated legacy trigger (2015). The rate reduction is the largest in the endcap, which has the highest rate of background muons from PU. [72]. Top right: Trigger efficiency as a function of the offline muon η, shown for the upgraded and legacy systems. [72] Bottom: Trigger efficiency as a function of muon p_{T} for the barrel (blue), overlap (green), and endcap (red) MTF regions. [73]

The L1 calorimeter trigger

A schematic diagram of the calorimeter trigger design is shown in Fig. 3.14. A Time-Multiplexed Trigger (TMT) design was used to ensure a flexible system with high granularity [74]. The trigger primitives are in this case energy deposits from ECAL and HCAL. In the barrel, each trigger primitive covers a $\Delta\eta \times \Delta\phi$ area of 0.087×0.087 corresponding to 5×5 crystals from ECAL and one HB tower. In the endcap, a TP is larger due to the coarser granularity of the calorimeters.

The information from each TP is first sent to the layer-1, which includes in total 18 Calorimeter Trigger Processor 7 (CTP7) cards, each spanning 4 TPs (20° sector in ϕ) and two calorimeter slices. Thus, the layer-1 is organised in 36 calorimeter slices. Each card receives information of the full η range. A single CTP7 card is able to receive 60 links operating at 5-6.4 Gb/s, and to transmit 48 links at 10 Gb/s. The layer-1 sums the ECAL and HCAL TP transverse energies to form trigger towers (TTs). The trigger towers are calibrated using LUTs. All information is sent to the layer-2 that reconstructs and further calibrates physics objects, such as E_{T} that is the scalar sum of the transverse energies of all calorimeter trigger towers ("energy sum"). For example jets are reconstructed from 9×9 trigger tower transverse energies.

The layer-2 is made of 9 MP7 cards ("nodes"), and each receives full event information for one bunch crossing, i.e. every 9th bunch crossing. This allows implementation of event level pileup subtraction, which results in reduced rates and thus lower trigger thresholds. Redundant nodes are available to replace a node in case of breakage. The Demux node collects the output from the layer-2 nodes, and ranks the input by transverse momentum. Finally, the 12 highest energy objects (electrons, taus, jets and energy sums) are sent to the GT.

Similarly to the L1 muon trigger, a large variety of studies on the performance of the L1 calorimeter trigger have been made. For example, the efficiency as a func-

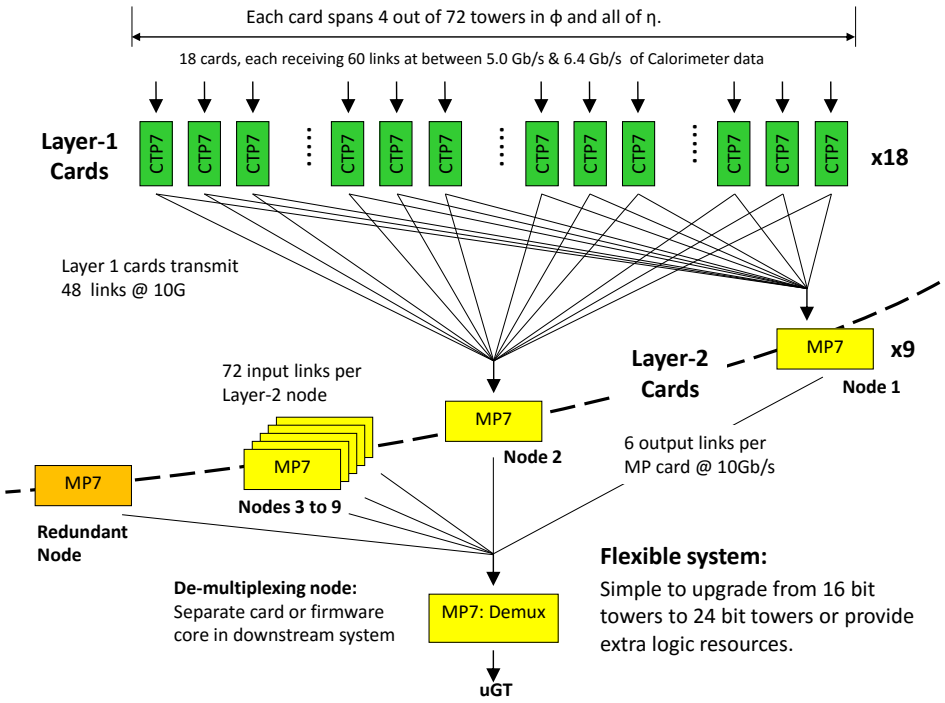

Figure 3.14: The Time-Multiplexed Trigger design used in the upgraded L1 calorimeter trigger. The layer-1 consists of 18 CTP7 processing cards that calibrate and sort trigger primitives. A full event information is sent to the layer-2 that includes nine MP7 cards - each card receives every 9th event. The layer-2 reconstructs and sorts physics objects that are sent to the De-multiplexing node that sums and ranks the input by transverse momentum. In total the 12 highest energy objects of each type (electrons, taus, jets and energy sums) are sent to the global trigger.

tion of reconstructed supercluster transverse energy E_{T} of the electron, shown in Fig. 3.15, demonstrates the sharp turn-on at the desired trigger threshold. Moreover, the integrated selection efficiency as a function of pileup for isolated τ-seeds highlights the stable performance, as seen also in Fig. 3.15. The effect of the pileup subtraction is shown in Fig. 3.16, which confirms that lower trigger threshold can be implemented without an increase in rate when the pileup subtraction is applied at the layer-2.

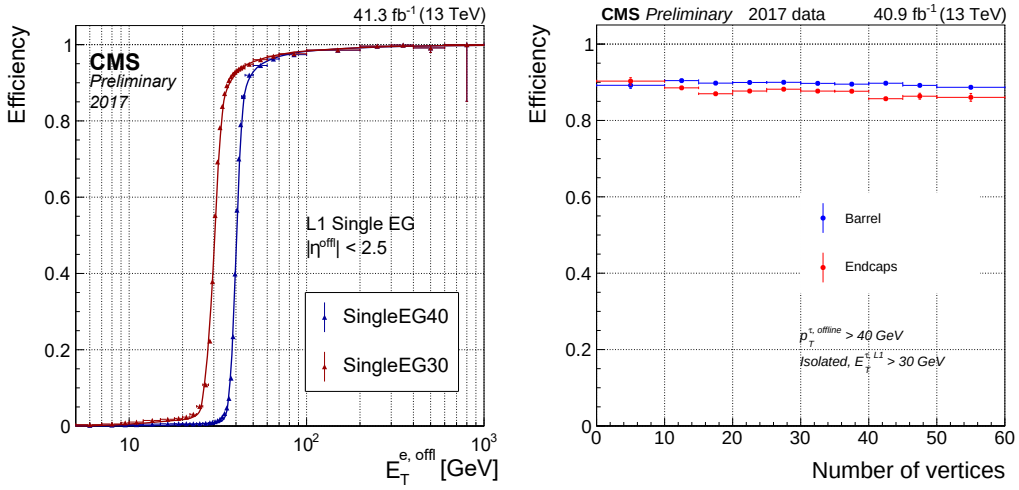

Figure 3.15: Performance of the upgraded L1 calorimeter trigger during 2017 for electrons and tau leptons. Left: L1 trigger efficiency curves for an e/γ object as a function of the offline E_{T} of the electron, measured with tag-and-probe method on data. The efficiency is drawn for an E_{T} threshold of 30 GeV (red) and 40 GeV (blue). Offline reconstructed electrons are required to have $|\eta^{\mathrm{off}}| < 2.5$, and a geometrical matching between the electron supercluster and the L1 candidate is applied. [75] Right: Integrated Level-1 selection efficiency as a function of pileup for isolated τ-seeds with $E_{\mathrm{T}}^{\tau,\mathrm{L1}} > 30$ GeV. The isolated τ-seeds are required to be matched to a well identified tau lepton reconstructed offline with $p_{\mathrm{T}}^{\tau,\mathrm{offline}} > 40$ GeV The pileup is estimated as the number of reconstructed offline vertices. For average PU of 55, the efficiency is approximately 90% both in barrel (blue) and endcaps (red). [76]

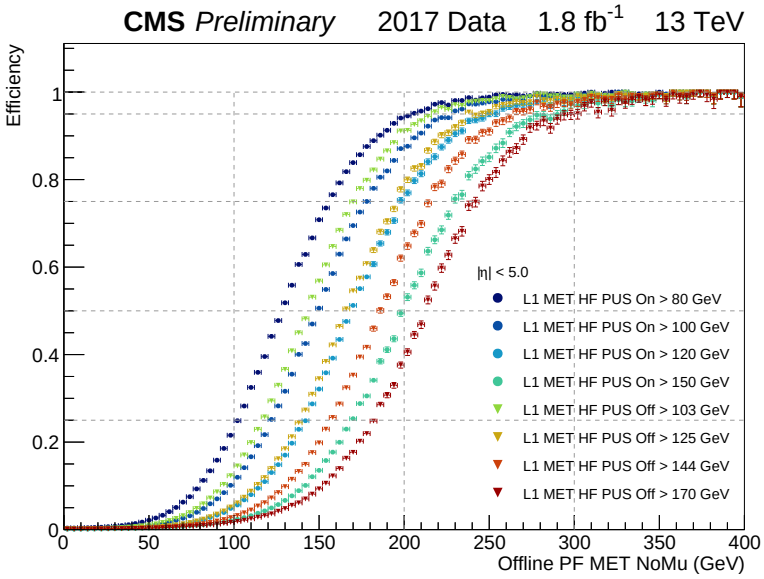

Figure 3.16: Efficiency curves for the upgraded Level-1 missing energy trigger as a function of offline particle-flow missing transverse energy (MET) excluding muons (GeV), based on events with a single offline muon. The efficiency curves for the trigger thresholds with the pileup subtraction (L1 MET HF PUS on) are compared to those for the trigger thresholds without the pileup subtraction (L1 MET HF PUS off). When the pileup subtraction is applied, lower the trigger thresholds produce the same rate, thus L1 MET HF PUS on $> 80/100/120/150$ GeV produce the same rate as L1 MET HF PUS off $> 103/125/144/170$ GeV, respectively. [77]

Operations and offline data validation

To ensure the proper functioning of the L1 trigger, the online operation of the L1 trigger relies on experienced shift-workers and on-call experts who monitor the L1 trigger each moment of the day during the data taking. The monitoring is based on the trigger rates for each algorithm, as well as monitoring plots produced on the fly by the Data Quality Monitoring (DQM) system. These monitoring plots include geometric distributions of muon and calorimeter system inputs ("occupancy distributions"), physics object variables (such as muon η and ϕ), and also the timing of the trigger seeds. In case of any unexpected discrepancy compared to the reference rates or distributions, the shift-worker alarms the on-call expert who investigates the matter promptly and determines any further steps required to return to successful data taking.

After the data taking, the collected data is certified and validated for physics analyses by each subsystem of the CMS experiment. The certification and validation process depends on the subsystem. The collected data is divided into runs[2], and each run undergoes the certification procedure. The data will become available for all physics analyses only if the individual validation procedure of each subsystem confirm a high quality of the data.

The L1 trigger system relies on a two-step process that was developed during the years 2017 and 2018 to its current format. The first step is "express certification", typically performed within 24 hours from collecting the data. The main goal of the express certification is to confirm no anomalous behaviour of the trigger system has gone unnoticed during the data taking. The purpose of the second step ("final certification") is to select the high-quality data, suitable for physics analyses.

Incorrect functioning of some part of the L1 trigger system may lead to ab-

[2]A run is a period of data taking, with a length varying from a few minutes up to multiple hours.

normal rates or DQM distributions. The express certification relies on examining the time evolution of the total output rate of L1 trigger, and performing comparisons between individual rates of different trigger seeds targeting physics objects and their reference rates. As the trigger rates depend on the data taking conditions, the reference rates are studied as a function of pileup in case of collision data, while for cosmic data taking the reference rates are based on previously recorded data. Moreover, the express certification accounts for the beam conditions, status of each subdetector, and dead time[3].

In addition to trigger rates, the express certification is performed based on the DQM plots produced during the data taking. The DQM system also provides comparison between the collected data and a reference run, or an emulator-level information. Statistical tests are done to identify any distributions that might differ from the expectation. Any irregularity is considered also in the final certification.

The DQM system can also produce efficiency and resolution distributions for each type of physics object, that are used together with the information from the express certification for the final certification. The tag-and-probe method [78] is used to calculate the efficiencies for different types of trigger seeds, whereas the resolutions are a result of comparing the trigger-level kinematic variables to their counterparts reconstructed offline. If no significant deviation from the expected performance is observed in the efficiency and resolution distributions, the data is certified as valid for physics analyses from the perspective of the L1 trigger. However, this requires that a successful trigger operation is indicated also by the results of the express certification.

If a certain run fails the certification criteria, prompt actions are taken to identify and understand the source of a performance loss. If the performance loss

[3]Dead time is the fraction of events lost because the trigger system is not ready to accept new events.

is severe, the data is discarded independently of the cause. Most common reasons behind a performance loss include malfunctioning of the L1 trigger itself, and missing or corrupted input from other subsystems. After the recent changes in the certification and validation procedures, the L1 trigger is able to perform the offline certification with luminosity section[4] precision which ensures that the data losses are minimised. Only 9.8 pb^{-1} (<0.1%) of the data collected in 2018 could not be accepted for physics analyses exclusively due to the offline certification of the L1 trigger.

The High Level Trigger

The output of the L1 trigger is forwarded to the HLT which is a software-based trigger implemented on a PC farm consisting up to 32 000 CPU cores. The HLT has access to the full event information from all subsystems, including the tracker, and the software is the same as used in the offline reconstruction. The HLT menu is based on hundreds of HLT paths that are made of alternating reconstruction (production) and filtering modules, seeded by different L1 requirements. The paths run independently and can share common modules. As the HLT has to reconstruct and filter events as soon as possible using basic physics objects, the fastest reconstruction modules are executed first, and the most time consuming operations are performed last. The selected events are output on data streams that may serve different purposes such as physics analysis, offline detector calibration, or online monitoring.

[4]Luminosity section is a subsection of a run during which time the instantaneous luminosity is unchanged. In the CMS experiment one lumi section corresponds to approximately 23 seconds of data taking.

4. Event reconstruction: Particle-flow algorithm

In the CMS experiment, each event is reconstructed using the particle-flow (PF) algorithm [16] in which information from all subdetectors is combined to identify and reconstruct the particles produced in the collisions. This holistic approach, demonstrated in Fig. 4.1, offers an improved event description compared to a traditional event reconstruction that relies on reconstructing *physics objects* (electrons, muons, photons, taus, and jets) and missing transverse momentum from signals collected by a given detector. For example, muon identification in the traditional approach is performed using mainly the information from the muon detectors, whereas the PF algorithm also accounts for calorimeter information. In practice this requires correlating the tracks and clusters of energy from all detector layers, which relies on high granularity of the detector layers.

The PF algorithm was initially designed and used for the ALEPH experiment at the LEP where each event had a much cleaner final state compared to those obtained at the LHC. The CMS detector, however, has characteristics suitable for the PF approach. The magnetic field ensures that the calorimeter energy deposits of neutral and charged particles are separated, and the tracker allows an excellent trajectory reconstruction of charged particles. The ECAL is highly-segmented, resulting in a clear separation between energy deposits from particles in jets. Even

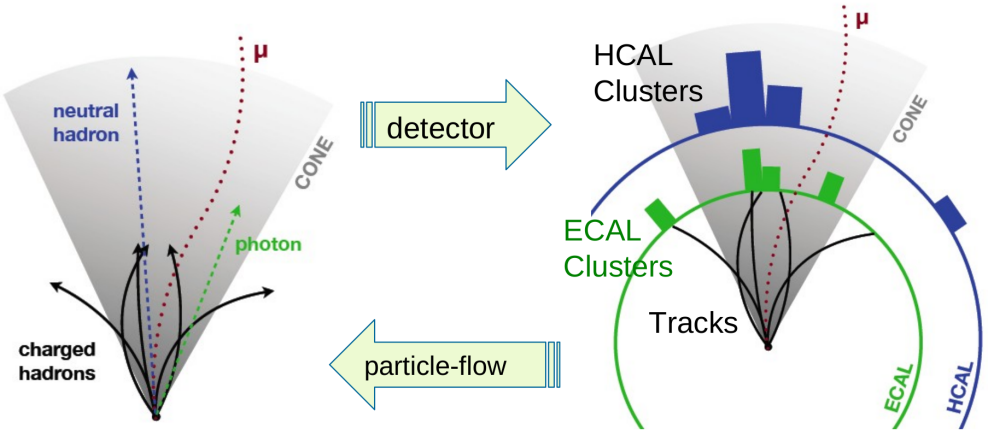

Figure 4.1: The particle flow algorithm identifies and reconstructs physics objects utilising tracks and energy clusters left behind by particles in the CMS detector. [79]

though the HCAL energy resolution is modest compared to the one obtained with the ECAL, it is sufficient to distinguish different energy deposits in jets; the neutral hadron energy deposits from those of the charged hadrons. Finally, the muon tracking system of the CMS provides a pure muon identification.

The event description produced by the PF algorithm seeds all analyses performed by the CMS Collaboration. At very least, the PF algorithm provides the reconstruction of taus, jets, and missing transverse momentum for each analysis. Additionally, it is possible - yet not required - to rely on the PF algorithm for reconstruction and identification of electrons, muons, and photons. Multiple analyses choose to implement a lepton (or photon) identification procedure alternative to the one offered by the PF algorithm, which is also the case in this search for the pseudoscalar A. Using the alternative identification for a lepton often benefits for example the fake rate measurement, described in detail in Section 5.6.

In this chapter I describe the working principles of the PF algorithm. I start by discussing basic elements - tracks and energy clusters - required as an input by the PF, and then cover how these elements are used to identify and reconstruct the physics objects used in physics analysis. Following sections are based on Ref. [16] unless otherwise mentioned.

4.1 Particle flow elements

The PF algorithm uses basic elements to identify and reconstruct physics objects. These elements include tracks in the tracker and in the muon system, and energy clusters in the calorimeter system. In this section the reconstruction of these basic elements are described.

4.1.1 Iterative tracking

Constructing tracks successfully requires a compromise between a tracking efficiency and a misreconstruction rate for a given particle. In general, a high tracking efficiency can be only achieved while allowing a large misreconstruction rate although this depends on the particle type. To ensure an optimal balance between a high tracking efficiency and small misreconstruction rates, iterative tracking is used in the CMS experiment: a Combinatorial Track Finder (CTF) [80] based on Kalman Filtering (KF) [81] is applied in several successive iterations.

The CTF algorithm itself has four steps. First, seeds for tracks are generated using a few hits compatible with a charged particle trajectory. Next, hits from all tracker layers along the said trajectory are gathered by building a trajectory. Before the final track selection based on quality requirements, a fit is performed to the track to determine the properties of the charged particle. These properties include the origin, transverse momentum, and direction.

The iterative tracking of the CMS experiment consists of 10 iterations, each of them aiming at as high purity of the track as possible. The first iterations are simple, and reconstruct easy tracks that would have high purity to start with. As soon as a hit is used for a track, it is masked and thus made unavailable for the next iteration. After each iteration, the operation gets more complex and more time consuming, allowing tracks with initial low-purity to be reconstructed with high efficiency and purity.

The first three iterations (1–3) use triplets of pixel hits as seeds. The targeted tracks thus include prompt particles, and particles from b hadron decays, as these leave clear tracks closest to the beam axis. These first iterations result in an overall efficiency of 80%, and the fraction of hits masked after these iterations is 40% (20%) in the pixel (strip) detector.

As the number of hits in the pixel is reduced, the next two iterations (4–5) are seeded by pixel pairs and pixel+strip triplets, yielding reconstruction of tracks with one or two missing hits in the pixel. This recovers not only detector inefficiencies, but also cases where a particle interacts or decays within the pixel detector volume, causing some hits to be missed.

As very displaced tracks are less likely to have pixel hits, their track reconstruction is performed in the next two iterations (6–7). This ensures that a reasonably small number of leftover hits are present in the strip detector that could otherwise cause misreconstruction of tracks. In these iterations either a strip pair or triplet is used to seed the track.

The eighth iteration targets charged particles inside jets with high transverse momentum. Such collimated jets often include multiple tracks close to each other, causing hits to be merged, reducing the tracking efficiency. Pixel hit clusters are split into several hits that are then paired with one of the remaining hits in the strip detector to form a seed. The last two iterations (9–10) target tracks from muons. They use muon detector information in the seeding step, and increase the muon track reconstruction efficiency.

Without the iterative process, the tracking efficiency would vary greatly for different particles. For example, an isolated muon can have a tracking effiency of 99% when the misreconstruction rate is at the level of a few percent. This is a large contrast to charged hadrons, such as pions, that more likely undergo a nuclear interaction within the tracker. As a result, the efficiency is much lower, approximately

70–80% for similar misidentification rates, as shown in Fig. 4.2. Moreover, as the transverse momentum of the charged pion increases, they are more likely to be inside a collimated jet, causing the efficiency to reduce further as the hits from overlapping particles cannot be disentangled. When all the aforementioned iterations are included, the tracking efficiency for charged hadrons is increased to approximately 90% for p_{T} values below 20 GeV, as also demonstrated in Fig. 4.2. At the same time, the misidentification rates stay within a few percent for the same p_{T} range.

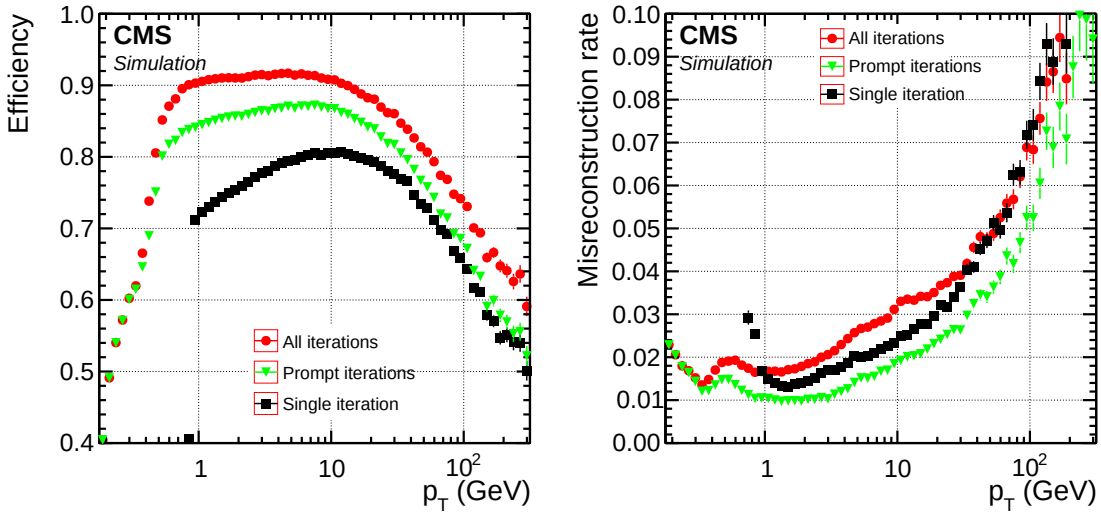

Figure 4.2: Efficiency (left) and misreconstruction rate (right) as a function of track p_{T} for charged hadrons in multijet events without pileup interactions. The results were obtained using the global combinatorial track finder with a single iteration (black), and the iterative tracking method including only prompt iterations (green) and all iterations (red). The prompt iterations are based on seeds with at least one hit in the pixel detector (iterations 1-5, and 8, described in the text). Tracks considered in the efficiency and misreconstruction rate determination must fulfil $|\eta| < 2.5$. Moreover, the tracks used for the efficiency determination are required to originate from within 3.5 cm of the beam axis and ±30 cm of the nominal centre of CMS along the beam axis. [16]

Electron tracks

Before reaching the ECAL, electrons may lose some of their energy due to interactions with the tracker material. The mechanism and the size of the energy loss

depend on the energy of the electron, and on the target material. Bremsstrahlung is the dominant cause of energy loss in silicon, when the electron energy exceeds a few tens of MeV. Changes in electron momentum make the reconstruction of the true path a challenging task for the KF algorithm that can only accommodate small changes in the electron path, thus the algorithm is suitable for nonradiating particles.

The KF algorithm assumes a Gaussian distribution for the energy deposits in the tracker, whereas for radiating electrons the energy loss is non-Gaussian. As a result, the KF algorithm does not manage the changes in the path of the radiating electron, and the tracks are often reconstructed with a small number of hits. To improve the track quality, a set of tracks are selected based on the number of hits and the χ^2 value of the original fit. The tracks are then fit again with a Gaussian-sum filter (GSF) [60], which relies on weighted sums of Gaussians instead of a single Gaussian, allowing large radiative energy losses. The details of electron track reconstruction are described in the following paragraphs.

The tracks are seeded by electron seeds, produced by a combination of two methods used for electron track reconstruction at the CMS experiment. Both methods aim at initiating the tracks from a few first hits in the tracker. The first method is a traditional electron seeding strategy, so-called ECAL-based approach, which relies on energetic ECAL clusters. The energy and position of each cluster guide towards hits in the innermost tracker layers, expected to be left by each electron. Superclusters are formed by multiple clusters from the electron and the bremsstrahlung photons, collected in a small window in η and an extended window in ϕ. A great performance of this method is only achieved if the radiated energy is collected precisely. For electrons in jets, the energy and position of the supercluster is often biased, resulting in a low efficiency of this method. Alternatively misreconstruction occurs as the supercluster is compatible with tracks from other particles. Finally,

electrons with a small transverse momentum are usually neglected as not all energy can be collected due to the large spread over an extended region.

The second method, so-called tracker-based approach, aims at recovering any inefficiency related to the ECAL-based approach. The tracker-based approach uses all tracks from the iterative tracking as seed candidates for electrons, given their transverse momentum is larger than 2 GeV. The candidate tracks are extrapolated towards the calorimeter, where they are matched to a supercluster.

The seeds from the tracker- and ECAL-based methods are combined into a set of electron seeds that are fed to the full electron tracking with GSF. Using information from both methods increases the tracking efficiency especially in the low-p_{T} region. As demonstrated in Fig. 4.3, the absolute efficiency gain for the simulated electrons from the Z boson decays is approximately 10% for electrons with transverse momentum 5–10 GeV. [16]

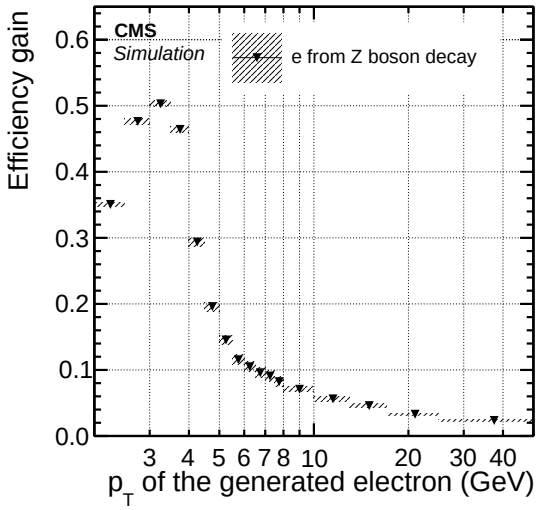

Figure 4.3: Absolute efficiency gain, resulting from including the tracker-based seeding, for electrons from Z boson decays as a function of p_{T}. [16]

Muon tracks

As the majority of the particles (excluding neutrinos) do not reach the muon system, high purity in the muon track reconstruction can be achieved. The final muon physics objects access a collection of three different muon track types. A muon can be classified into one or more of the following categories: a standalone muon, global muon, and tracker muon.

A standalone muon track is based on only the information from the muon detector. The track is seeded from track segments that are clustered hits within each DT or CSC detector. Pattern recognition is used to gather all hits from DT, CSC, and RPC along the trajectory. The muon candidates reconstructed only using the standalone muon track tend to have a lower momentum resolution compared to that of the two other muon categories.

A global muon track uses a standalone muon track that is matched to a track in the inner tracker. If the parameters of the two tracks are compatible when propagated to a common surface, the hits from both tracks are combined and fit further to produce the global muon track. This reconstruction is designed to increase efficiency for muons that pass more than one muon detector plane. For a muon with large transverse momentum ($p_{\mathrm{T}} \gtrapprox 200\,\mathrm{GeV}$), a track in the inner tracker is rather straight, and thus the global muon fit improves the momentum resolution. However, if the muon has a low momentum, it might not penetrate through many detector planes due to multiple scattering in the steel of the return yoke, resulting in lower efficiency.

In these cases the efficiency is usually recovered by using *a tracker muon reconstruction* that requires only one muon segment matched to a track in the tracker. Each track in the tracker is extrapolated to the muon system if the corresponding transverse momentum is larger than 0.5 GeV (total momentum $> 2.5\,\mathrm{GeV}$). A local (x, y) coordinate system transverse to the beam axis is used for the matching. The

local x coordinate is defined as the best measured coordinate in the r–ϕ plane, and the local y coordinate is orthogonal to it. A match is declared if the difference between the x coordinates of the extrapolated track and the segment is smaller than 3 cm, or alternatively if the ratio of this distance to its uncertainty is smaller than 4.

Almost all (99%) of the muons produced within the geometrical acceptance of the muon detector are reconstructed either as a global muon or a tracker muon, if not both. If a global muon and a tracker muon have the same inner track, they are merged into a single candidate. Any misreconstruction caused by charged hadrons reaching the muon systems can be recovered during the PF muon identification that is discussed later in Section 4.2.

4.1.2 Calorimeter clusters and their calibration

Clustered energy deposits in the calorimeter system are the second basic element given as a input to the PF algorithm. The PF reconstruction relies on a specific clustering algorithm that performs the clustering separately in each subdetector except in the HF where each cell offers an HF EM or an HF HAD cluster. The clustering algorithm aims at separating the energy deposits from all particles except muons. This is essential in detecting and measuring the energy and direction of photons and neutral hadrons. Moreover, the calorimeter clusters are used to reconstruct and identify electrons and the possible bremsstrahlung photons. It also benefits the energy measurement of charged hadrons for which the track was mismeasured due to low quality or high transverse momentum.

The clustering algorithm first identifies cluster seeds that are cells with an energy exceeding a given threshold and the energy of the neighbouring cells. Topological clusters are crafted from the seeds by combining cells with at least a corner in common with a cell already belonging in the cluster. The candidate cell must have an energy two times larger than the noise level. In the ECAL endcaps seeds

are required to have E_{T} larger than a given threshold as the noise level increases as a function of θ. Finally, an iterative expectation-maximisation algorithm based on a Gaussian-mixture model is used to reconstruct the clusters within a topological cluster by assuming that each seed causes a Gaussian energy deposit. The cluster parameters are obtained by fitting an amplitude function based on the Gaussian energy deposit.

Both electromagnetic and hadron deposits are calibrated after the clustering to ensure correct reconstruction of photons and neutral hadrons, as described in the following paragraphs.

In the ECAL, a residual energy calibration is performed to correct for an unavoidable underestimation of the photon energy. As the clustering algorithm applies several thresholds to the ECAL cell energies, the measured energy of the incoming photon is smaller than the true energy of the photon. Moreover, it is also smaller than the energy of the superclusters used for the absolute calibration of the ECAL response to electrons and photons, determined from multiple measurements before the data taking.

The residual energy calibration is determined from simulated single photons. In the barrel ECAL, an analytical function is fitted to a two-dimensional distribution of the ratio between the measured and true energy of the photon, and the pseudorapidity of the cluster. At low energies corrections of +20% can be obtained, in contrast to high energies where the threshold effects are negligible. In the endcap, information from the two preshower layers are included to the energy cluster calibration. If there is no information from the preshowers, the calibration is similar to that of the one performed in the ECAL barrel. For large photon energies, the correction is +5%, whereas for the smallest photon energies a correction of +40% is obtained in the preshower region. Across all energies and ECAL regions, the calibrated energy agrees with the true photon energy on average within ±1%. Additionally, specific

electron and photon energy corrections are applied after the reconstruction.

As the ECAL response is different for hadrons and for photons, the HCAL calibration must account for cases where a fraction of the shower energy is deposited in the ECAL. Moreover, the calorimeter response is nonlinear. Measuring the true hadron energy thus requires recalibration of both ECAL and HCAL clusters, which is performed using a sample of simulated single neutral hadrons (K^0_L). The barrel and endcap regions are treated separately due to different thresholds and cell sizes. Hadrons leaving energy only in the HCAL are studied separately from those leaving energy both in the ECAL and HCAL. Hadrons with only ECAL deposits will be considered as photons or electrons by the PF algorithm, and are not recalibrated for this reason. After the calibration, the mean relative difference between the calibrated energy and the true energy is compatible with zero, as shown in Fig. 4.4. In other words, the linearity of the calorimeter response is restored. This leads also to an improved energy resolution.

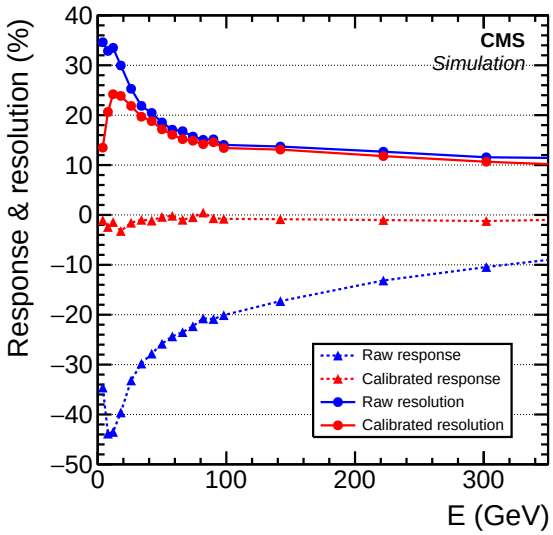

Figure 4.4: The relative energy response (dashed curves and triangles) and resolution (full curves and circles) for single hadrons in the barrel, as a function of their true energy E. The relative raw (calibrated) energy response and resolution are marked with blue (red). [16]

4.2 Particle identification and reconstruction

Once the PF elements have been reconstruced and calibrated, *a link algorithm* is used to connect the PF elements from different subdetectors. This step is a crucial part of the particle reconstruction, as a single particle often results in several PF elements in the subdetectors.

Any pair of elements can be tested by the link algorithm. The probability of linking elements only from a single particle depends on the granularity of the different subdetectors, and by the number of particles that need to be resolved from each other. All elements of a given particle are linked with a probability constrained by the amount of material encountered, which may change the trajectory of the particle or cause secondary particles. Once two elements are linked, a distance between the two elements is defined to quantify the quality of the link. The specific requirements for linking two elements depend on the type of the elements and are as follows:

1. *A track in the central tracker and a calorimeter cluster:* The track is extrapolated to the two layers of preshower, the ECAL, and the HCAL. The extrapolation depth in the HCAL (ECAL) corresponds to one interaction length (the expected maximum of a typical longitudinal electron shower profile). If the track's extrapolated position is within a cluster area, the track is linked to that cluster. The cluster area is defined by the union of the areas of individual cells, enlarged in all directions by the size of a cell. The link distance is the distance between the extrapolated track position and the cluster position in the (η, ϕ) plane. Only one cluster can be linked to a track, and thus the link with the smallest distance is kept in case of multiple configurations. Potential bremsstrahlung photons are linked based on tangents to the GSF tracks extrapolated to the ECAL. Moreover, tracks from photon conversions are treated with a dedicated conversion finder.

2. *Two calorimeter clusters:* A cluster-to-cluster link is searched for only between ECAL clusters and preshower clusters, or between HCAL clusters and ECAL clusters. The former is performed in the preshower acceptance, whereas in the latter case this is done beyond the tracker acceptance. The cluster position in the more granular calorimeter (preshower or ECAL) must be within the cluster envelope in the less granular calorimeter (ECAL or HCAL) to establish a link. The link distance is the distance between the two cluster positions in the (η, ϕ) plane for an HCAL-ECAL link, whereas the (x, y) plane is used for an ECAL-preshower link. The link with the smallest distance is kept.

3. *Multiple charged-particle tracks:* A common secondary vertex is required, necessary for reconstructing nuclear-interactions. The relevant displaced vertices can be considered if they feature at least three tracks. At most one of the these tracks can be an incoming track, reconstructed with tracker hits in between the primary vertex and the displaced vertex. The invariant mass of the outcoming tracks must be larger than 0.2 GeV. If a selected nuclear-interaction vertex is shared by multiple tracks, these tracks can be linked together.

4. *A track in the central tracker and information in the muon detector:* Linking is performed to form global and tracker muons, as explained in detail in Section 4.1.

Once the links have been formed, *PF blocks* are produced out of elements associated either by a direct or an indirect link through common elements. Each PF block undergoes the identification and reconstruction sequence aimed at forming *PF objects* that include muons, electrons, photons, neutral hadrons, and charged hadrons. The sequence starts by identifying and reconstructing muon candidates. Before the next step, the corresponding PF elements are removed from the PF block. After the muons, electrons are identified and reconstructed, with a goal to collect the

energy from all bremsstrahlung photons, in addition to all other photons. As previously done, the corresponding tracks and ECAL or preshower clusters are removed. The last particles to be reconstructed and identified are hadrons and nonisolated photons. Higher-level objects, such as jets and tau leptons, are reconstructed from combinations of the PF objects. Neutrinos are considered through missing transverse momentum, which in turn relies on reconstruction of all the PF objects in an event.

4.2.1 Muons

The PF algorithm uses global and tracker muon properties in order to determine a set of selections resulting in the muon identification process. Isolated global muons are selected first, followed by identification of nonisolated muons that may be used for further analysis given they meet certain conditions.

The isolation of a muon is based on a distance parameter ΔR to the muon direction in the (η, ϕ) plane. Additional inner tracks and calorimeter energy deposits are considered with $\Delta R < 0.3$. If the sum of the p_{T} of the tracks and the E_{T} of the deposits does not exceed 10% of the muon p_{T}, the muon candidate is isolated and will be added to the collection of PF muons.

Nonisolated muons are required to pass the tight-muon selection in addition to selection based on number of track segments in the muon detectors or compatibility of associated calorimeter deposits with the muon hypothesis. If the nonisolated muon does not pass the tight-muon selection, the muon can be still selected if it has a high quality standalone muon track fit and a large number of hits in the muon system. Alternatively, a high quality tracker track fit and associated calorimeter clusters compatible with the muon hypothesis are sufficient for the nonisolated muon to be selected for further analysis.

If the transverse momentum of the inner track is less than 200 GeV, the muon

momentum is chosen to be that of the inner track. For higher p_{T} values, the momentum is chosen to be the most compatible track fit based on different track fits: tracker only, tracker and first muon detector plane, global, and global without the muon detector planes featuring a high occupancy.

Once the muons have been reconstructed, the corresponding PF elements are masked from the PF block. The muon identification and reconstruction is finalised only after the charged hadrons have been identified and reconstructed: if a charged hadron track momentum is significantly larger than the calibrated sum of the linked calorimeter clusters, the algorithm may have neglected a muon. In such case the muon identification and reconstruction is revisited with looser selections than before, and the identification and reconstruction process within the PF block is redone from the beginning.

This search for the pseudoscalar A decaying into a Z boson and an SM-like Higgs boson relies on muons satisfying a so-called PF ID Loose working point, that requires that the muon is either global or tracker muon, and passes the PF muon reconstruction requirements. The reconstruction and identification efficiency is $> 99\%$ for the PF ID Loose working point, and a momentum resolution of 1% (3%) is achieved for muons with $p_{\mathrm{T}} = 100\,\mathrm{GeV}$ in the barrel (endcap) [66].

Additional selection is based on the lepton isolation discriminant I^{ℓ} that is defined for both muons and electrons to reject nonprompt or misidentified leptons:

$$I^{\ell} \equiv \frac{\sum_{\text{charged}} p_{\mathrm{T}} + \max\left(0, \sum_{\text{neutral}} p_{\mathrm{T}} - \frac{1}{2}\sum_{\text{charged, PU}} p_{\mathrm{T}}\right)}{p_{\mathrm{T}}^{\ell}}, \tag{4.1}$$

where p_{T}^{ℓ} stands for the p_{T} of the lepton. The variable $\sum_{\text{charged}} p_{\mathrm{T}}$ is the scalar sum of the transverse momenta of the charged particles originating from the primary vertex and located in a cone of size $\Delta R = \sqrt{(\Delta\eta)^2 + (\Delta\phi)^2} = 0.4\,(0.3)$ centered on the muon (electron) direction, where ϕ is the azimuthal angle in radians. The sum $\sum_{\text{neutral}} p_{\mathrm{T}}$ represents a similar quantity for neutral particles. The scalar sum of the transverse momenta of charged hadrons originating from pileup vertices in the cone,

$\sum_{\text{charged, PU}} p_{\text{T}}$, is used to estimate the contribution of photons and neutral hadrons originating from pileup vertices. The factor of 1/2 corresponds approximately to the ratio of neutral- to charged-hadron production in the hadronization process of inelastic pp collisions. The isolation requirements used in this analysis are based on I^{ℓ}, and are described in Section 5.3.

4.2.2 Electrons and photons

Electrons and photons are reconstructed after muons. They share the same reconstruction step as the basic properties, as well as the tracking and the energy deposition patterns, are similar for electrons and photons. A GSF track seeds an electron candidate in the PF block, given there are no three or more additional tracks linked to the corresponding ECAL cluster. A photon candidate is seeded by an ECAL supercluster with $E_{\text{T}} > 10\,\text{GeV}$ and no link to a GSF track.

For ECAL-based electron candidates, the sum of energies measured in the HCAL cells with a distance to the supercluster position smaller than 0.15 in the (η, ϕ) plane must not exceed 10% of the supercluster energy. This applies also for photon candidates. As the reconstruction process may miss some of the deposited energy, the total energy of the collected ECAL clusters is corrected. At low p_{T} values, for the thickest tracker region ($|\eta| < 1.5$), the corrections can be as large as 25%. The electron direction is taken to be that of the GSF track, whereas the energy is obtained as a combination of the corrected ECAL energy with the momentum of the GSF track. The photon direction is chosen to be that of the supercluster, and an energy calibration similar to the one used for electrons is applied.

Both electrons and photons must fulfil additional requirements to be selected in the PF collection. For electrons, additional identification criteria based on boosted decision trees (BDTs) with up to 14 input variables is used. The BDTs are trained separately for the barrel and endcap regions, and for isolated and nonisolated elec-

trons. Photons, on the other hand, are required to be isolated from other tracks and calorimeter clusters. Moreover, the ECAL cell energy distribution must be compatible with the one expected from a photon shower, as is required for the ratio between the HCAL and ECAL energies.

As done for muons, all PF elements used to reconstruct electrons and photons are removed from the PF block to ensure no element is used twice. Also the tracks identified as a result of photon conversion are masked to prevent misreconstruction of tracks.

The analysis described in this thesis requires that the electron candidates pass an identification criterion which is based on a multivariate (MVA) discriminant instead of the PF identification. Quantities describing the compatibility of the measurements from the tracker and the ECAL, the quality of the tracks, and the shapes of the ECAL energy deposits are given as an input to the MVA discriminant [61]. The MVA working points used in this analyses have efficiencies of 90% and 80%.

4.2.3 Hadrons and nonisolated photons

Jet fragmentation and hadronisation result in other hadrons, (nonisolated) photons, and leptons. Thus, they are reconstructed and identified after muons, electrons, and isolated photons.

The charged and neutral hadrons in each PF block are identified based on the remaining ECAL and HCAL clusters and the tracks linked to these clusters. The charged hadrons are identified first by comparing the calibrated calorimetric energy to the sum of the track momenta. No neutral particles are reconstructed if the calibrated calorimetric energy is compatible with the sum of the track momenta. In this case, the charged hadron momenta are obtained from a fit of the measurements in the calorimeters and the tracker.

If the calibrated energy is larger than the sum of the track momenta, the

presence of photons and neutral hadrons is considered. Each track results in a charged hadron that has momentum and energy of that of the corresponding track momentum, under the charged-pion mass hypothesis. An excess greater than the expected calorimeter energy resolution for hadrons is required.

Clusters not linked to any track give rise to neutral hadrons and nonisolated photons. The identification of neutral hadrons and nonisolated photons can be made simpler based on studies of hadronic jets and how their energy is deposited to the calorimeter system. Since neutral hadrons leave only 3% of the jet energy to the ECAL, all ECAL clusters within the tracker acceptance ($|\eta| < 2.5$) are turned into photons. Similarly all HCAL clusters are turned into neutral hadrons. Beyond the tracker acceptance, $\sim$25% of jet energy is deposited to the ECAL by charged and neutral hadrons. Thus, links between ECAL and HCAL clusters are taken into account: if an ECAL cluster is not linked to an HCAL cluster, it is classified as a photon. If such link exists, an ECAL cluster is assumed to be a result of a hadron shower. Identified photons and hadrons are calibrated as discussed earlier.

As described previously, if the calibrated energy is significantly (3 standard deviations) smaller than the track momentum, a relaxed search for muons is performed. If the relative precision of the reconstructed muon momentum is better than 25%, the additional muon is identified as a PF muon and the track is masked for the next iteration. If the calibrated energy is still significantly smaller than the track momentum sum, the tracks of lower quality can be masked. Once the reduced sum of the track momenta is compatible or smaller than the calibrated calorimetric energy, the charged and neutral hadrons can be identified as discussed above.

4.3 Composite physics objects and event-level quantities

Combinations of the PF objects are used to reconstruct higher-level physics objects, such as jets and tau leptons. In this section, I will concentrate on the reconstruction of tau leptons, since they are present in the final state of the analysis. However, as the reconstruction of tau leptons relies on reconstruction of jets, also their reconstruction is discussed. Event-level quantities, such as primary vertex reconstruction and missing transverse momentum are covered, as they play in important role in the reconstruction of the A boson.

4.3.1 Jets and the primary vertex of the interaction

Jets are reconstructed by clustering neutral and charged PF objects using an anti-k_{T} algorithm, implemented in the FASTJET library [82, 83]. The grouping is performed within a distance parameter of 0.4. Charged PF objects are required to be associated with the *primary vertex of the interaction*.

The primary interaction vertex is chosen out of all possible vertices in the event. First, the tracks assigned to each vertex are clustered into so-called track jets using the jet finding algorithm from Refs. [82, 84]. The momentum of each track jet is the vectorial sum of all particle momenta in the track jet. Moreover, the negative vector sum of the $\vec{p}_{\mathrm{T}}$ of these jets defines *the associated missing transverse momentum*, computed in each vertex. The primary pp interaction vertex is taken to be the reconstructed vertex with the largest value of summed p_{T}^2 of track jets and the associated missing transverse momentum.

The apparent momentum of the jet reconstructed from the PF objects can differ from that of the particle level jet. To account and correct for these differences, jet energy corrections are derived and applied correspondingly. One source

of such difference is pileup, that is observed as additional tracks and calorimetric energy depositions, resulting in increased momentum. The pileup-related jet energy correction is applied both to the data and simulated events. Additional jet energy corrections arise from non-linear detector response to jets. Simulation studies are used to derive jet energy corrections for both the data and simulated events, resulting in the average measured response of jets identical to that of particle level jets. Finally, any residual differences between the jet energy scale in data and in simulation are determined from in situ measurements of the momentum balance in dijet, photon+jet, Z+jet, and multijet events, yielding corrections that are applied correspondingly to the data events [85].

Identification of jets originating from bottom quarks

Many processes include jets that are likely to have originated from a bottom quark ("b-tagged jets"). In this analysis, the signal events contain no b jets ($gg \rightarrow A$), or only b jets with a relatively soft p_T distribution ($b\bar{b}A$). Contributions from such background processes, especially $t\bar{t}$ and $t\bar{t}Z$, can be reduced by discarding all events with one or more b-tagged jets ("b jet veto"). As will be demonstrated in Section 5.3, this selection does not decrease the signal selection efficiency.

B-tagged jets are identified using the combined secondary vertex algorithm [86] that is based on an MVA discriminant. As b jet hadronisation results in b-hadrons with relatively long lifetime, the MVA receives as an input the secondary vertices associated with the jet and the track-based lifetime information. A set of p_T - dependent correction factors are applied to the simulated events [86] to account for differences in the b tagging efficiency between data and simulation. Genuine b jets have an identification efficiency of about 70%. Meanwhile, light-flavour or gluon jets have a misidentification probability of approximately 1%.

4.3.2 Tau leptons

The tau lepton has a mass of 1.7 GeV, making it nearly 3500 times heavier than the electron. Due to this large mass, a tau lepton decays in a prompt manner within the detector material. Tau leptons decay hadronically in 64.8% of all decays. The hadronic decay channels include one or more charged hadrons, and can include also neutral hadrons (π^0). Each hadronic final state contains a neutrino. The rest of total branching fraction (35.2%) is covered by the leptonic decay modes, where a tau lepton decays into an electron or a muon, accompanied by two neutrinos. The majority of the decay channels are shown in Table 4.1. In this thesis, τ_{h} denotes a tau lepton decaying hadronically.

Table 4.1: Branching fractions of tau leptons for the most common decay modes. The symbol for a hadron, h^-, represents either a pion or a kaon. The branching fractions for τ^+ leptons are obtained by inverting the charge in each decay mode.

Decay mode	Meson resonance	$\mathcal{B}$[%]
$\tau^- \to \mathrm{e}^- \bar{\nu}_e \nu_\tau$		17.8
$\tau^- \to \mu^- \bar{\nu}_\mu \nu_\tau$		17.4
$\tau^- \to \mathrm{h}^- \nu_\tau$		11.5
$\tau^- \to \mathrm{h}^- \pi^0 \nu_\tau$	$\rho(770)$	26.0
$\tau^- \to \mathrm{h}^- \pi^0 \pi^0 \nu_\tau$	$\mathrm{a}_1(1260)$	9.5
$\tau^- \to \mathrm{h}^- \mathrm{h}^+ \mathrm{h}^- \nu_\tau$	$\mathrm{a}_1(1260)$	9.8
$\tau^- \to \mathrm{h}^- \mathrm{h}^+ \mathrm{h}^- \pi^0 \nu_\tau$		4.8
Other modes with hadrons		3.2
All modes containing leptons		35.2
All modes containing hadrons		64.8

Reconstructing the hadronic decays of a tau lepton is a major challenge, as quark and gluon jets can be easily misidentified as a τ_{h} candidate. However, as shown in Table 4.1, the number of particles produced in a hadronic tau decay is small, unlike in quark and gluon jets. The end products of a hadronic tau decay

also deposit their energies in more narrow regions than those from energetic quark or gluon jets.

The hadrons-plus-strips (HPS) algorithm [87, 88], that is used to reconstruct hadronic decays of tau leptons, accounts for the aforementioned differences. Anti-k_{T} jets seed the HPS algorithm that takes the constituents of reconstructed jets, and combines information from charged hadrons ("prongs") and the π^0 candidates ("strips") to form τ_{h} candidates as described below. A single τ_{h} candidate per jet is saved for further analysis. The selected τ_{h} candidate is required to have a charge of ± 1. Moreover, the τ_{h} candidate must not have charged particles or centers of strips outside the signal cone, defined as

$$R_{sig} = 3.0\,\mathrm{GeV}/p_{\mathrm{T}}, \tag{4.2}$$

where p_{T} is the transverse momentum of the hadronic system. The signal cone is further required to have a size between 0.05 to 0.10. Finally, if there are multiple τ_{h} candidates, the one with the largest p_{T} is kept.

Reconstruction of charged hadrons and π^0 candidates

The charged hadrons considered for the τ_{h} reconstruction must origin from the primary vertex of the event, and are required to have $p_{\mathrm{T}} > 0.5\,\mathrm{GeV}$ to ensure sufficient track quality. The reconstruction of π^0 candidates relies on clustering PF photons and electrons into strips in the $\eta - \phi$ plane.

Each photon and electron with $p_{\mathrm{T}} > 0.5\,\mathrm{GeV}$ within the reconstructed jet is considered as a possible part of a strip. If the total transverse momentum of the strip exceeds 2.5 GeV, it is kept as a π^0 candidate for further processing. Photons produced in the pion decay often undergo photon conversion, which results in electrons and photons. As the electrons are bent in the magnetic field, the calorimeter signatures of neutral pions are broadened. To contain all the energy deposits, the strips are elongated in the ϕ direction. Originally the strips were of constant size

$(0.05\eta \times 0.20\phi)$, but for the Run II, the algorithm was updated to use a dynamic strip reconstruction.

In the dynamic strip reconstruction, the size of a strip is varied to ensure a more effective collection of the π^0 decay products, which allows a larger or a smaller strip size depending on the situation. The first strip is seeded by the highest p_{T} electron or photon in the jet. A strip with an initial position of the electron or photon in the $\eta - \phi$ plane is formed. The transverse momentum of the strip is the vectorial sum of momenta of all the strip constituents, i.e. at this stage just the transverse momentum of the highest p_{T} electron or photon.

Next, the rest of the strip constituents are determined by studying all electrons or photons in the jet in order of decreasing transverse momentum, i.e. starting from the subleading electron or photon. Any electron or photon can be merged into the existing strip as long as the candidate is within a strip size defined by the transverse momenta of the existing strip and the candidate electron or photon. Simulated events of single tau leptons were used to derive functions describing the strip size so that it includes 95% of all electrons and photons from the hadronic tau decays. The obtained functions at given transverse momenta of the strip and the candidate are:

$$\begin{aligned} \Delta\eta &= 0.20 \cdot p_{\mathrm{T},e/\gamma}^{-0.66} + 0.20 \cdot p_{\mathrm{T,strip}}^{-0.66} \\ \Delta\phi &= 0.35 \cdot p_{\mathrm{T},e/\gamma}^{-0.71} + 0.35 \cdot p_{\mathrm{T,strip}}^{-0.71}, \end{aligned} \tag{4.3}$$

where the value of $\Delta\eta$ is required to lie between 0.05 and 0.15, whereas for $\Delta\phi$ the range is 0.05–0.3. If the strip size would not be of the required size, the considered electron/photon is removed from the strip. If the considered electron/photon is added to the strip, the strip position is recomputed as a p_{T} weighted average of all electron/photon constituents of the strip. This iterative process is repeated until there are no electrons or photons that are within the allowed $\Delta\eta \times \Delta\phi$ window. A new strip is seeded by the next highest p_{T} electron or photon within the considered jet, as long as it is not yet associated with any strip.

Forming the hadronic tau candidates

The number of tracks and the number of strips, which respectively represent the number of charged hadrons and the number of π^0 present in the decay, determine the decay mode of the hadronic tau candidate. When a strip is considered for the τ_{h} reconstruction, the center of the strip must be within the signal cone. However, a part of the strip can lie outside the signal cone. Up to 6 charged hadrons and the 6 strips with the highest p_{T} are given to the HPS algorithm that reconstructs the τ_{h} candidates based on this information. The HPS algorithm generates all possible combinations of hadrons, categorised into three decay modes: 1-prong ($\mathrm{h}^{\pm}$), 1-prong+π^0s ($\mathrm{h}^{\pm}\pi^0$ and $\mathrm{h}^{\pm}\pi^0\pi^0$), and 3-prong ($\mathrm{h}^{\pm}\mathrm{h}^{\mp}\mathrm{h}^{\pm}$). Only the decay mode with a final state of $\mathrm{h}^-\mathrm{h}^+\mathrm{h}^-\pi^0\nu_\tau$ is not included, as the branching fraction is small (4.8%) and it is contaminated by jets. The reconstructed decays of tau leptons and the corresponding decay mode categorisation are demonstrated in Fig. 4.5.

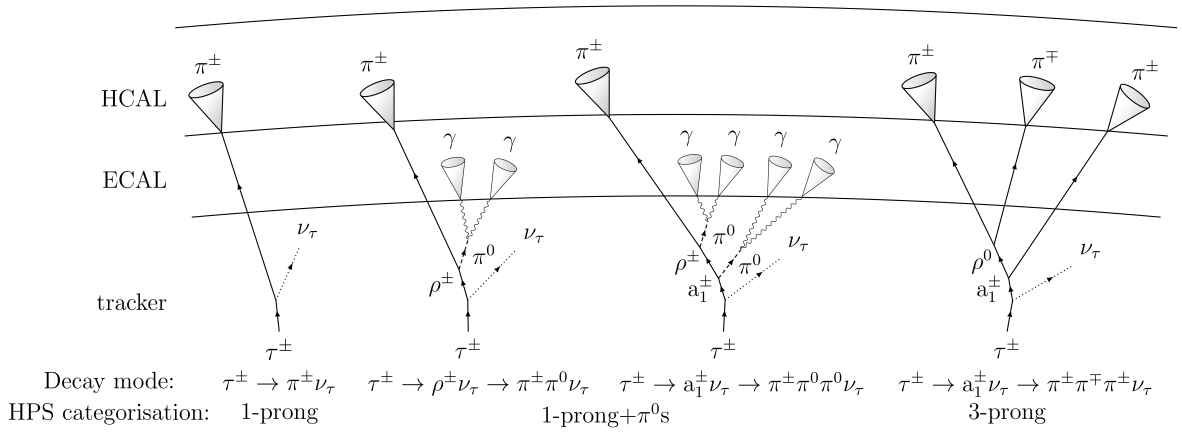

Figure 4.5: Hadronic decays of tau leptons reconstructed with the hadron-plus-strips algorithm. The corresponding decay mode categorisation of the hadron-plus-strips algorithm is also indicated. Image: Izaak Neutelings

Each reconstructed decay mode must have a visible mass compatible with intermediate meson resonance given it is present in the decay mode. Thus, the 1-prong decay without an intermediate meson resonance must have a mass compatible

with that of the charged pion, i.e. 140 MeV. For the other decay modes with either $\rho(770)$ or $a_1(1260)$ mesons, the mass constraints are as follows:

1. 1-prong+π^0: $0.3\,\text{GeV} - \Delta m_{\tau_h} < m_{\tau_h} < 1.3\,\text{GeV} \cdot \sqrt{p_T^{\tau_h}/(100\,\text{GeV})} + \Delta m_{\tau_h}$, and the upper limit on the mass window is between 1.3 and 4.2 GeV,

2. 1-prong+$\pi^0\pi^0$: $0.4\,\text{GeV} - \Delta m_{\tau_h} < m_{\tau_h} < 1.2\,\text{GeV} \cdot \sqrt{p_T^{\tau_h}/(100\,\text{GeV})} + \Delta m_{\tau_h}$, and the upper limit on the mass window is between 1.2 and 4.0 GeV, and

3. 3-prong: $0.8 < m_{\tau_h} < 1.5\,\text{GeV}$,

where Δm_{τ_h} is the change in the mass of the τ_h object through the addition of the electron or photon of the dynamic strip.

Discriminating against jets, electrons, and muons

Quark or gluon jets, as well as electrons and muons, can be misidentified as τ_h candidates. Calorimetric information, isolation sums, and lifetime information is given to an MVA discriminant [88] that combines the corresponding variables to provide the best possible discrimination between jets and hadronically decaying tau leptons. The MVA discriminant is implemented using a BDT, trained with simulated τ_h candidates with $p_T > 20\,\text{GeV}$ and $|\eta| < 2.3$. The working points for the reconstructed τ_h candidates are chosen to have isolation efficiencies between 40 and 95% for τ_h candidates passing the decay mode reconstruction described above. The working point chosen for this analysis, Medium Tau MVA, has an efficiency of 70% for selecting τ_h candidates passing the HPS reconstruction discussed above. At the same time, a misidentification rate as low as 1% is achieved.

Isolated electrons and muons can be misreconstructed as hadronic tau leptons especially in the 1-prong decay mode. Electrons can also mimic the 1-prong+π^0 decay mode. To suppress misidentification rates from electrons and muons, we apply criteria on the consistency between the measurements in the calorimeters, the

tracker, and the muon detectors. For example, signals in the muon detector found near the τ_h direction can be used to veto τ_h candidates.

Multivariate BDT and cut-based discriminants are utilised to discriminate against electrons and muons, respectively [88]. Two working points to reject muons misidentified as τ_h candidates are available and used in this analysis: AGAINST-μ LOOSE, and AGAINST-μ TIGHT. The working points developed to reject electrons misidentified as τ_h candidates vary from very loose to very tight: AGAINST-E VLOOSE, AGAINST-E LOOSE, AGAINST-E MEDIUM, AGAINST-E TIGHT, and AGAINST-E VTIGHT. The working points used in this analysis are AGAINST-E VLOOSE and AGAINST-E TIGHT.

The efficiencies for the aforementioned working points are estimated from simulated $Z \to \tau\tau$ events. The misidentification probabilities for the AGAINST-E VLOOSE and AGAINST-E TIGHT working points, measured in simulated $Z \to ee$ events, are <10 and $<0.5\%$, while efficiencies of about 85% and 75% are achieved. A notably higher efficiency is obtained for both AGAINST-μ discriminants, $>99\%$, whilst the loose (tight) working point offers a misidentification probability of $\sim$0.4 (0.1)% (estimated using simulated $Z \to \mu\mu$ events).

4.3.3 Missing transverse momentum

Neutrinos are the only particles described by the standard model that cannot be detected directly at the CMS experiment as they do not interact with the detector material. However, neutrinos contribute to the missing transverse momentum. The missing transverse momentum vector, $\vec{p}_T^{miss}$, is computed as the negative vector sum of the transverse momenta of all the PF objects in an event, and its magnitude is denoted as p_T^{miss} [89]. Corrections to the energy scale of the reconstructed jets in the event are further accounted for in the computation of the $\vec{p}_T^{miss}$, resulting in an adjusted missing transverse momentum vector ("type-1" corrected $\vec{p}_T^{miss}$) which is

used in this analysis.

5. Data analysis

In this chapter, I describe the details of a search for the pseudoscalar A boson decaying into an SM-like Higgs boson h and a Z boson. This chapter is largely based on Ref. [1], the corresponding search performed by the CMS Collaboration, for which I was the key analyser, the contact author as well as the paper editor. A data set of proton-proton (pp) collisions is used for this search. The data set was collected by the CMS experiment at $\sqrt{s} = 13\,\text{TeV}$ during 2016. The Feynman diagram of the studied process is shown in Fig. 5.1. The search targets primarily the gluon fusion production of the A boson, but the associated production with b quarks is also accounted for in the interpretation of the results. Decays of the SM-like Higgs boson into a pair of tau leptons are considered in four possible $\tau\tau$ decay channels ($\text{e}\tau_\text{h}$, $\mu\tau_\text{h}$, $\tau_\text{h}\tau_\text{h}$, and $\text{e}\mu$) along with Z boson decays into two light leptons, i.e. $\text{Z} \to \ell^+\ell^-$ ($\ell = \text{e}, \mu$). Combining the decay channels of the h and Z bosons results in eight distinct final states of the A boson decay. Throughout this chapter, neutrinos present in the final states are omitted from the notation.

The reconstructed mass of the A boson candidate is used to discriminate between signal- and background-like events. The A boson reconstruction relies on the SVFIT algorithm [17, 18] that accounts for the missing transverse momentum stemming from the neutrinos in the final states. As a novel approach for this type of analysis, a mass constraint of 125 GeV has been applied when reconstructing the four-vector of the SM-like Higgs boson using the SVFIT algorithm. The new

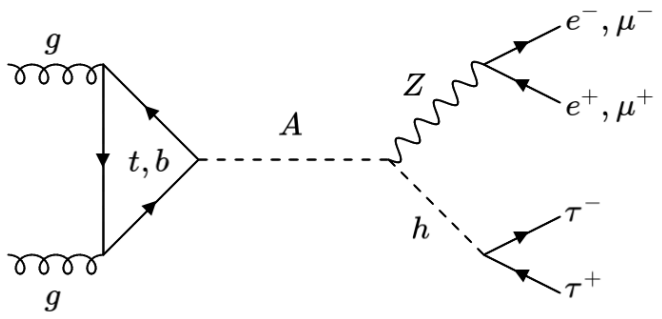

Figure 5.1: The Feynman diagram for the process gg → A → Zh → $\ell\ell\tau\tau$ targeted in this search.

mass reconstruction method presented in this chapter offers improved discrimination against the dominant background processes (qq → ZZ, gg → ZZ, $t\bar{t}$, Z + jets, and WZ + jets). As a result, this approach significantly increases the sensitivity of the search compared to the previous result presented by the CMS Collaboration [43].

This chapter is structured as follows. First, I will introduce the data set, the simulated samples, and the signal models used in this study. After I have discussed the event selection and event weights, I describe the reconstruction of the A boson, and the optimisation of the event selection. Finally, the estimation of the contribution from background processes is discussed. The systematic uncertainties and the signal extraction are discussed in Chapter 6, while the results are presented in Chapter 7.

5.1 Data set

This search is based on a data set of proton-proton (pp) collisions, collected in 2016 by the CMS experiment at $\sqrt{s} = 13\,\text{TeV}$, corresponding to an integrated luminosity of $35.9\,\text{fb}^{-1}$. This data set is a result of a careful offline certification, and thus is slightly smaller than the one initially recorded: during the data taking in 2016, LHC delivered $41\,\text{fb}^{-1}$ of pp collisions, and the CMS experiment recorded $37.8\,\text{fb}^{-1}$.

5.2 Simulated samples and signal models

Signal and background processes are studied using simulated events. Different Monte Carlo (MC) generators are available, and allow for modelling of the full proton-proton collisions. Producing simulated events requires multiple steps [90, 91]:

1. *Producing the hard-scattering process*, which is the process of interest,
2. Accounting for the substructure of colliding hadrons, which in practice means deciding which *Parton Distribution Function (PDF)* to use,
3. *Including the underlying event*, i.e. the interactions not associated with the hard-scattering event, resulting in additional particles,
4. *Describing parton showers*, i.e. how soft gluons, radiated from color charged particles, decay. Parton showers are matched and merged with the hard-scattering process,
5. *Hadronization*, where quarks and gluons form hadrons,
6. *Simulation of the particle interactions in the detector*,
7. *Adding pileup* (includes both in-time and out-of-time pileup),
8. *Simulation of the detector response*, and
9. *Event reconstruction* (same as for data).

The most commonly used MC generators in the CMS experiment are MadGraph5_aMC@NLO [92] and POWHEG [93–95]. This analysis also relies on these MC generators, as discussed in Subsections 5.2.1 and 5.2.2. To model the parton showering and fragmentation, as well as the decay of the tau leptons, the generators are interfaced with PYTHIA 8.212 [96]. The PYTHIA parameters affecting the

description of the underlying event are set to the CUETP8M1 tune [97]. The set of PDFs used in the simulation is NNPDF3.0 [98].

Before the generated events can be analysed, they must be processed through a simulation of the CMS detector. In the CMS experiment, the simulation of the detector is based on GEANT4 [99]. The event reconstruction of the simulated events is identical to that of the data events. The simulated samples include additional pp interactions per bunch crossing, considering the main bunch crossing, and the preceding and subsequent bunch crossings. These are referred to as in-time pileup and out-of-time pileup, respectively. The pileup reweighting is described more in detail in Subsection 5.4.2.

5.2.1 Signal samples

Simulated events for the signal process $gg \to A \to Zh \to \ell\ell\tau\tau$ are generated at LO using MadGraph5_aMC@NLO v2.4.2. The simulated events include the Z boson decay into two leptons (electrons, muons, or taus). The considered A boson mass points are motivated by the theoretical predictions discussed in Section 2.5.2, and vary between 220 and 400 GeV. The lowest signal mass point is 220 GeV, because the A boson must be massive enough to decay into the considered Zh state. The mass range extends up to 400 GeV, slightly above where the mass of the A boson exceeds twice the top quark mass, and the $A \to t\bar{t}$ decay channel becomes dominant. The signal samples are based on the m_h^{mod+} model [100], and a low value of $\tan\beta$ ($\sim$2) is assumed. The generated width of the A boson is small compared to the instrumental resolution for all masses. Additional signal events are simulated for a 300 GeV A boson produced in association with b quarks ($b\bar{b}A$), and are only necessary for studying the selection efficiency, required to set model-dependent limits. The details of the study are discussed in Chapter 7.

5.2.2 Samples for background processes

Higgs boson production through processes predicted in the SM (e.g., Zh, Wh, $t\bar{t}h$) are considered as background processes, in addition to all other SM processes that result in nonnegligible yield in the studied final states. The contribution from Higgs boson events produced via gluon fusion or vector boson fusion and decaying into two tau leptons is negligible.

Background processes with a Higgs boson, produced in association with a W or Z boson (Wh or Zh), where the h boson decays into two tau leptons, are generated at NLO in QCD with the POWHEG 2.0 [101, 102] generator, extended with the MiNLO procedure [103]. The transverse momentum (p_{T}) distribution of the Higgs boson simulated by POWHEG is tuned to match the NNLO plus next-to-next-to-leading-logarithmic prediction of the HRes 2.3 generator [104, 105]. The production cross sections and branching fractions for the SM Higgs boson production and their corresponding uncertainties are taken from Refs. [38, 106, 107].

The background samples for $t\bar{t}h$, $t\bar{t}$, WZ, and $qq \to ZZ$, as well as $Wh \to WWW$, $Wh \to WZZ$, $Zh \to ZWW$, $Zh \to ZZZ$, and $gg \to h \to ZZ$ processes, are generated at NLO with POWHEG 2.0. The MCFM [108] programme is used to generate the $gg \to ZZ$ process at LO. Simulations of the $qq \to ZZ$ and $gg \to ZZ$ processes include all SM events with two Z bosons in the final states, excluding the ones from the $gg \to h \to ZZ$ process. The MadGraph5_aMC@NLO 2.2.2 or 2.3.3 generator is used for triboson, $Z + \text{jets}$, $t\bar{t}W$, and $t\bar{t}Z$ production, with the jet matching and merging scheme applied either at NLO with the FxFx algorithm [109] or at LO with the MLM algorithm [110].

5.2.3 Signal models

To produce model-dependent interpretations of the results described in Chapter 7, we compute production cross sections and branching fractions of the pseudoscalar

A. In the low-tb-high scenario, Higgs boson masses, mixing parameters and effective Yukawa couplings were calculated with FeynHiggs 2.10.2 [111–115]. In the hMSSM scenario, analytical functions were used as described in Ref. [15].

In both benchmark scenarios, inclusive gluon-gluon fusion process cross sections are obtained with SusHi 1.4.1 [116], which includes supersymmetric NLO QCD corrections [117–122], NNLO QCD corrections for the top quark contribution in an effective theory of a heavy top quark [123–127] and electroweak effects from light quarks [128, 129]. Inclusive $b\bar{b}A$ production cross sections at NNLO QCD accuracy in the five-flavor scheme are calculated with SusHi, based on bbh@nlo [130]. These $b\bar{b}A$ cross sections are combined with the $b\bar{b}A$ cross section calculation at NLO in QCD in the four-flavor scheme [131, 132] using the Santander matching scheme [133].

The branching fractions are computed differently for the two benchmark scenarios. In the hMSSM scenario, branching fractions are solely computed with HDECAY 6.40 [134–136], whereas in the low-tb-high scenario the most precise results of HDECAY, FeynHiggs and PROPHECY4f [137–139] are combined.

5.3 Event selection

The primary datasets used in this analysis consist of events selected by multiple HLT paths. Events are selected online using dilepton or single-lepton triggers targeting leptonic decays of the Z bosons: the double electron, double muon, single electron, and single muon triggers. This approach provides a great efficiency without the need of relying also on triggers with hadronic taus, that would introduce complications in estimating the trigger efficiencies and the reducible backgrounds from data. The trigger paths remained unprescaled throughout 2016 data taking. The HLT paths used in the analysis are shown in Table 5.1.

The trigger and offline selection requirements for the Z boson decay modes are

Table 5.1: The dilepton or single-lepton triggers, and the corresponding HLT paths used in this analysis.

Trigger	The HLT path(s)
The double electron	HLT_Ele23_Ele12_CaloIdL_TrackIdL_IsoVL_DZ
The single electron	HLT_Ele27_WPTight_Gsf
The double muon	HLT_Mu17_TrkIsoVVL_Mu8_TrkIsoVVL_DZ, or
	HLT_Mu17_TrkIsoVVL_TkMu8_TrkIsoVVL_DZ
The single muon	HLT_IsoMu24 or HLT_IsoTkMu24

presented in Table 5.2. Each lepton selected by the trigger is required to be geometrically matched to a corresponding lepton selected in the analysis. An additional criterion based on the distance parameter ΔR is applied to ensure that leptons in an event are separated from each other. Two light leptons must fulfil $\Delta R > 0.3$, while the distance parameter between τ_h candidates and any other lepton is required to be larger than 0.5. Events with additional identified and isolated electrons or muons are discarded to ensure that the resulting event samples are mutually exclusive.

Table 5.2: Trigger and offline selection requirements for the different Z boson decay modes. The events are selected using either dilepton triggers with lower-p_T thresholds or single-lepton triggers with higher-p_T thresholds. The subscripts 1 and 2 indicate the higher- and lower-p_T leptons associated with the Z boson, respectively.

Decay channel	$\mathrm{Z} \to \ell\ell$ trigger selection	$\mathrm{Z} \to \ell\ell$ offline selection
$\mathrm{Z} \to \mathrm{ee}$	$[p_\mathrm{T}^{\mathrm{e}_1} > 23\,\mathrm{GeV}$ & $p_\mathrm{T}^{\mathrm{e}_2} > 12\,\mathrm{GeV}]$	$[p_\mathrm{T}^{\mathrm{e}_1} > 24\,\mathrm{GeV}$ & $p_\mathrm{T}^{\mathrm{e}_2} > 13\,\mathrm{GeV}]$
	or $p_\mathrm{T}^{\mathrm{e}_1} > 27\,\mathrm{GeV}$	or $p_\mathrm{T}^{\mathrm{e}_1} > 28\,\mathrm{GeV}$
$\mathrm{Z} \to \mu\mu$	$[p_\mathrm{T}^{\mu_1} > 17\,\mathrm{GeV}$ & $p_\mathrm{T}^{\mu_2} > 8\,\mathrm{GeV}]$	$[p_\mathrm{T}^{\mu_1} > 18\,\mathrm{GeV}$ & $p_\mathrm{T}^{\mu_2} > 10\,\mathrm{GeV}]$
	or $p_\mathrm{T}^{\mu_1} > 24\,\mathrm{GeV}$	or $p_\mathrm{T}^{\mu_1} > 25\,\mathrm{GeV}$

The nontriggering electrons and muons are required to have $p_\mathrm{T} > 10\,\mathrm{GeV}$, whereas τ_h candidates are required to have $p_\mathrm{T} > 20\,\mathrm{GeV}$. The $|\eta|$ constraints from

detector geometry are $|\eta^{e}| < 2.5$, $|\eta^{\mu}| < 2.4$, and $|\eta^{\tau_h}| < 2.3$ for electrons, muons, and τ_h candidates, respectively. Triggering and nontriggering electrons and muons have the same $|\eta|$ boundaries. Moreover, muons and electrons must be originating from the primary vertex. This is ensured by requiring that the distance to the primary vertex along the beam direction (transverse plane) fulfils $|d_z| < 0.2\,\text{cm}$ ($|d_{xy}| < 0.045\,\text{cm}$). The reconstructed τ_h candidates are expected to be further than electrons and muons in the transverse plane, and thus only must satisfy $|d_z| < 0.2\,\text{cm}$ along the beam direction.

The Z boson is reconstructed from a pair of opposite-charge, same-flavor light leptons that fulfils $60 < m_{\ell\ell} < 120\,\text{GeV}$. If an event has more than one Z boson candidate, the one with the mass closest to the Z boson mass is selected. A high signal acceptance is maintained by applying loose identification and isolation selection criteria to the leptons associated to the Z boson. The electrons (muons) forming the Z boson candidate are required to pass the loose working point of the electron (muon) identification, corresponding to an average efficiency of 90 (>99)%. The muons must pass an isolation requirement of $I^{\mu} < 0.25$, where the isolation discriminant has the form as defined in Eq. 4.1 for muons.

The leptons associated with the h boson decay are required to have opposite charge. The specific signal selections, listed in Table 5.3, are a result of optimisation studies, and yield the best signal sensitivity. The τ_h candidates associated with the SM-like Higgs boson must satisfy the MEDIUM TAU MVA working point of the τ_h identification and isolation. As described in Subsection 4.3.2, this working point corresponds to an average efficiency of 70%. The contributions from the Z+jets process, and other reducible backgrounds, are decreased by applying tighter selection criteria to the light leptons in case of the $e\tau_h$, $\mu\tau_h$, and $e\mu$ decay channels. Electrons from tau lepton decays must pass the tight working point of the electron identification, corresponding to an average efficiency of 80%. The isolation requirements

are $I^{\mathrm{e}(\mu)} < 0.15$ for electrons (muons) associated to a tau lepton decay. The specific definition of the isolation discriminant depends on the lepton type, as defined in Eq. 4.1.

Table 5.3: Kinematic selection requirements for each A boson decay channel, applied on top of the looser selections and b jet veto described in the text. The muons associated with the Z boson must also pass the identification requirement that has an efficiency of > 99%. The identification (and isolation) requirements are described by $\epsilon^{\ell}_{\mathrm{id.}}$ that stands for the efficiency of the identification requirement for a given lepton type. The leptons assigned to the SM-like Higgs boson are required to have opposite charge. In the $\ell\ell + \tau_{\mathrm{h}}\tau_{\mathrm{h}}$ channel, we additionally require $L_{\mathrm{T}}^{\mathrm{h}} > 60\,\mathrm{GeV}$, where $L_{\mathrm{T}}^{\mathrm{h}}$ is the scalar p_{T} sum of the visible decay products of the SM-like Higgs boson.

Channel	Z boson selection	h boson selection
$\ell\ell + \mathrm{e}\tau_{\mathrm{h}}$	Opposite-charge, same-flavor light leptons, $60 < m_{\ell\ell} < 120\,\mathrm{GeV}$	$\epsilon^{\mathrm{e}}_{\mathrm{id.}} = 80\%$, $I^{\mathrm{e}} < 0.15$, $\epsilon^{\tau_{\mathrm{h}}}_{\mathrm{id.+iso.}} = 70\%$
$\ell\ell + \mu\tau_{\mathrm{h}}$		$\epsilon^{\mu}_{\mathrm{id.}} > 99\%$, $I^{\mu} < 0.15$, $\epsilon^{\tau_{\mathrm{h}}}_{\mathrm{id.+iso.}} = 70\%$
$\ell\ell + \tau_{\mathrm{h}}\tau_{\mathrm{h}}$		$\epsilon^{\tau_{\mathrm{h}}}_{\mathrm{id.+iso.}} = 70\%$, $L_{\mathrm{T}}^{\mathrm{h}} > 60\,\mathrm{GeV}$
$\ell\ell + \mathrm{e}\mu$		$\epsilon^{\mathrm{e}}_{\mathrm{id.}} = 80\%$, $I^{\mathrm{e}} < 0.15$, $\epsilon^{\mu}_{\mathrm{id.}} > 99\%$, $I^{\mu} < 0.15$

The signal events contain relatively high-p_{T} decay products due to the large h boson mass, unlike the events from the Z + jets ("reducible") background process which include lower p_{T} jets misidentified as leptons. Selecting events based on the scalar p_{T} sum of the visible decay products of the SM-like Higgs boson, $L_{\mathrm{T}}^{\mathrm{h}}$, suppresses the reducible background process. The relative ratio of reducible to irreducible backgrounds is the largest in the $\ell\ell + \tau_{\mathrm{h}}\tau_{\mathrm{h}}$ final states, as is demonstrated in Fig. 5.2 that shows the $L_{\mathrm{T}}^{\mathrm{h}}$ distribution in the $\ell\ell + \mu\tau_{\mathrm{h}}$ and $\ell\ell + \tau_{\mathrm{h}}\tau_{\mathrm{h}}$ final states for the signal and background processes. The measurement and grouping of the background processes are discussed in Sections 5.6 and 7, respectively. A selection based on $L_{\mathrm{T}}^{\mathrm{h}}$ is placed on events in the $\ell\ell + \tau_{\mathrm{h}}\tau_{\mathrm{h}}$ final states: requiring $L_{\mathrm{T}}^{\mathrm{h}} > 60\,\mathrm{GeV}$ removes approximately 60% of the events from the reducible background process without compromising the signal selection efficiency.

We further suppress the contributions from background processes, especially

$t\bar{t}$ and $t\bar{t}Z$, by rejecting all events with one or more b-tagged jets ("b jet veto"). The signal selection efficiency is not significantly reduced since the signal events contain no b jets ($gg \to A$), or only b jets with a relatively soft p_T distribution ($b\bar{b}A$). The fraction of $gg \to A$ signal events lost due to the b jet veto is negligible, while for the $b\bar{b}A$ process approximately 17% of events are removed with this selection. The $gg \to A$ ($b\bar{b}A$) signal events with $m_A = 300\,\text{GeV}$ have a total acceptance of 3.9 (3.0)%.

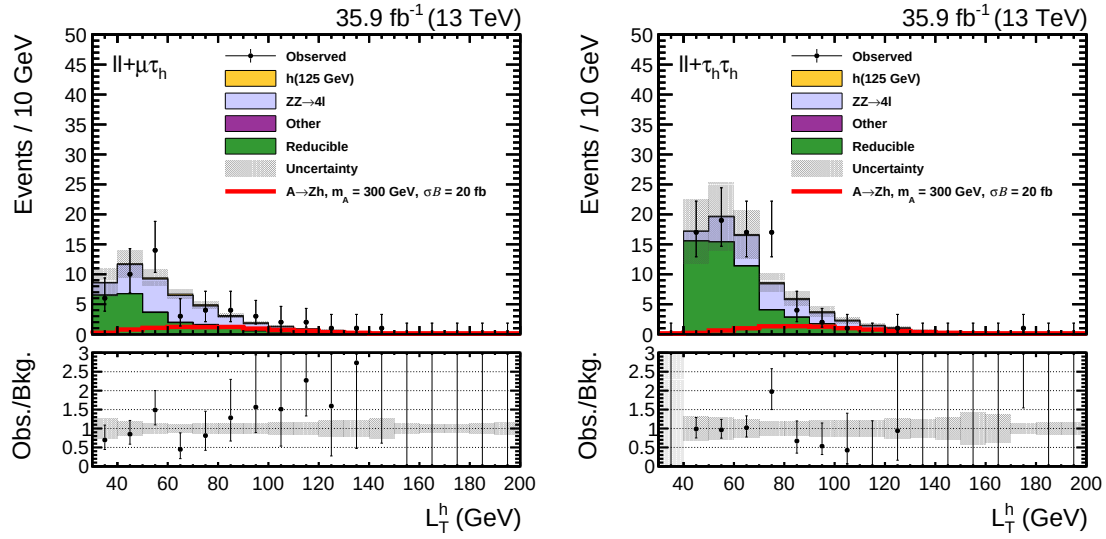

Figure 5.2: The L_T^h distribution and uncertainties in the $\ell\ell + \mu\tau_h$ (left) and $\ell\ell + \tau_h\tau_h$ (right) final states before a background-only fit is performed simultaneously in all eight final states. All signal region selections were applied, except $L_T^h > 60\,\text{GeV}$ in the $\ell\ell + \tau_h\tau_h$ channel. The two $Z \to \ell\ell$ decay channels are combined together only for visualization purposes. The uncertainties include both statistical and systematic components. The expected contribution from the $A \to Zh$ signal process is shown for a pseudoscalar Higgs boson with $m_A = 300\,\text{GeV}$ with the product of the cross section and branching fraction of 20 fb and is for illustration only.

5.4 Corrections to the simulation

As the detector response cannot be perfectly simulated, there are multiple discrepancies between the data and the simulated events. Theoretical predictions used in the

simulation are limited to a certain degree, forming another source of such discrepancies. To improve the agreement between the observed and simulated events, various corrections are applied on an event-by-event basis to simulated events. The derivation and application of these corrections is described in the following paragraphs. Most of these corrections are applied as weights to the simulated events.

5.4.1 Trigger efficiencies

Small differences in trigger selection efficiencies are observed between data and simulation. The tag-and-probe method [78] is used to measure the trigger efficiencies for electrons (muons) from a sample of $Z \to ee$ ($Z \to \mu\mu$) events. The efficiency is defined for all the six HLT paths utilised in this analysis. The tag lepton passes the identification and isolation criteria, and is selected by a monitoring trigger. The probe lepton is required to fulfil the same identification and isolation criteria as the tag lepton. The trigger efficiency is computed both for the data and simulated events as a ratio of events with all probe leptons and those that pass also the trigger used in this analysis. The efficiencies are measured as a function of lepton p_{T} and η. A scale factor, defined as the ratio between the two efficiencies, is applied to simulated events.

5.4.2 Pileup reweighting

Pileup reweighting is performed to ensure the distribution of the number of pileup interactions per event in simulation matches the one of the data. As the simulated events are produced before the end of the data taking, only an initial estimate of the luminosity spectrum of the year is available at the time of simulation. To take the effect of pileup into account, concurrent minimum bias collision events are generated with the recommended minimum bias cross section of 69.2 mb [53]. The measured instantaneous luminosity for each bunch crossing is used to estimate the

pileup distribution of the data, while assuming a minimum bias cross section of 69.2 mb. This procedure results in an average of approximately 23 interactions per bunch crossing [53]. The simulated events are weighted such that the distribution of the number of pileup interactions matches with that observed in data.

5.4.3 NNLO cross section estimation factor for diboson samples

The qq $\rightarrow$ ZZ and gg $\rightarrow$ ZZ samples are generated at NLO and LO, but higher-order calculations of the cross sections of the qq $\rightarrow$ ZZ and the gg $\rightarrow$ ZZ processes have been performed. A more precise estimate of the background prediction can be obtained by using a κ-*factor* [140], i.e. by multiplying the prediction by the ratio of the higher-order and the previously computed lower-order cross sections, neglecting the impact of higher order corrections on the shape of the background distributions. Each event of the simulated qq $\rightarrow$ ZZ sample is weighted with a factor of 1.1 that provides the NLO-to-NNLO scaling [141–143]. In the case of the simulated gg $\rightarrow$ ZZ sample, the LO-to-NNLO scaling is obtained by applying a weight of 2.1 to each event [38].

5.4.4 Corrections related to electrons and muons

The identification and isolation efficiencies measured for electrons and muons differ in data and simulated events. Discrepancies exist also in the electron track reconstruction efficiencies. For muons, an additional correction factor related to the impact parameter selections is applied.

The electron and muon efficiencies are determined from a tag-and-probe measurement in Z $\rightarrow$ ee [144] and Z $\rightarrow \mu\mu$ [145] events, respectively. The correction factors are derived as a function of both lepton p_{T} and η. The overall correction factor can be as low as 0.72 (0.88) for low transverse momentum electrons (muons)

in the endcap region.

The correction factor related to the electron identification (corresponding to an average efficiency of 80%) varies between 0.87 and 0.93 in the barrel, whereas in the endcap the correction factor is between 0.8 and 0.9 for $10 < p_{\mathrm{T}} < 100\,\mathrm{GeV}$. The correction factor related to the electron track reconstruction has been measured for electrons with $25 \leq p_{\mathrm{T}} \leq 500\,\mathrm{GeV}$. The correction factor is 0.95–1.05 for $|\eta| < 2.4$, but for $-2.5 < \eta < -2.4$ ($2.4 < \eta < 2.5$) the correction is 1.11 (0.91). [144]

The correction factor related to the muon identification (corresponding to an average efficiency of $> 99\%$) and isolation ($I^{\mu} < 0.15$) are > 0.99 both in the barrel and endcap for muons with $p_{\mathrm{T}} \geq 20\,\mathrm{GeV}$. The muon impact parameter selection correction factor is 99.5% for each muon candidate. [145]

5.4.5 Tau lepton identification efficiencies

The identification efficiencies for τ_{h} candidates have been determined using the tag-and-probe method in $\mathrm{Z}/\gamma^{*} \to \tau\tau \to \mu\tau_{\mathrm{h}}$ events [88]. The invariant mass of the visible $\mu\tau_{\mathrm{h}}$ is reconstructed, and a maximum likelihood fit is performed on the invariant mass distribution to extract the data-to-simulation correction factor for each of the τ_{h} identification working points. The correction factors are valid for $p_{\mathrm{T}}^{\tau_{\mathrm{h}}}$ up to $\approx 60\,\mathrm{GeV}$, and work is ongoing to provide correction factors as a function of $p_{\mathrm{T}}^{\tau_{\mathrm{h}}}$. The Medium Tau MVA used in the analysis has a correction factor of 0.97 ± 0.05. The correction factor is applied for each τ_{h} candidate matched to a generated hadronically decaying tau lepton.

5.4.6 Tau lepton energy correction

The energy scale of τ_h candidates was measured using $\mathrm{Z}/\gamma^{*} \to \tau\tau$ events in the $\mathrm{e}\tau_{\mathrm{h}}$ and $\mu\tau_{\mathrm{h}}$ final states [88]. The distribution of the visible mass of the $\ell\tau_{\mathrm{h}}$ system was fitted to extract a correction factor for each decay mode. The obtained correction

factor is applied to each simulated τ_h candidate matched to a generated hadronically decaying tau lepton. The corrections in the $h^{\pm}$, $h^{\pm}\pi^0$s, and $h^{\pm}h^{\mp}h^{\pm}$ decay modes are -0.5%, $+1.1\%$, and $+0.6\%$, respectively. All correction factors have an uncertainty of 1.2%.

The energy scale of electrons and muons misidentified as τ_h candidates was also measured with a similar method using $Z \to \ell\ell$ events where one of the leptons is misidentified as a τ_h candidate. The obtained corrections are applied to simulated events with a τ_h candidate reconstructed in the $h^{\pm}\pi^0$s decay mode, if the τ_h is matched to a generator level electron or muon (prompt or from a tau decay). The correction is 9.5 (1.5)% for electrons (muons) misidentified as a τ_h candidate.

5.4.7 Generator event weight and expected number of events

Each simulated event is weighted by the weight computed for it by the matrix element generator. For samples produced at LO or with the POWHEG generator, the weight is a positive integer, but samples produced with the MadGraph5_aMC@NLO can contain both positive and negative event weights. Moreover, each simulated event is weighted according to the expected number of events for the given process. This weight is defined in terms of the sum of the weights on all the events of the sample (before any selection), the most precise estimate of the cross section for the process, and the integrated luminosity of the modelled data set.

5.5 Reconstruction of the A boson

Multiple methods to reconstruct the A boson were considered for this search, and three of them are described below. The resulting mass distributions are shown in Fig. 5.3.

The simplest reconstruction of the A boson relies on the visible decay products.

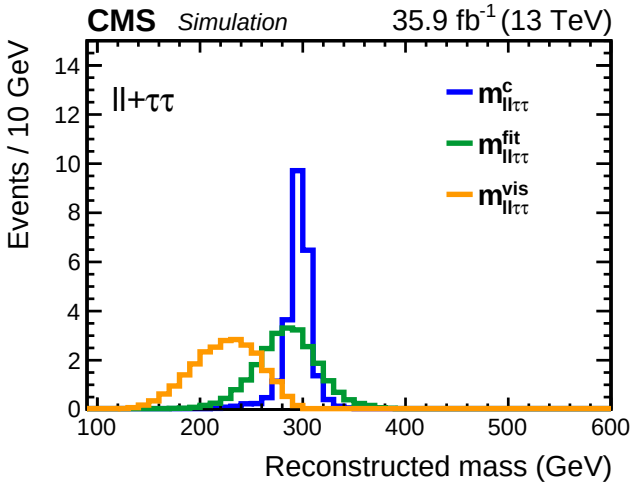

Figure 5.3: The distribution of the A boson mass for the three studied mass reconstruction methods at 300 GeV: using only the visible decay products ($m^{\text{vis}}_{\ell\ell\tau\tau}$, orange), using the SVFIT algorithm ($m^{\text{fit}}_{\ell\ell\tau\tau}$, green), and using the SVFIT algorithm with a mass constraint of 125 GeV for the SM-like Higgs boson ($m^{\text{c}}_{\ell\ell\tau\tau}$, blue). The eight final states of the A boson decay are combined for visualization purposes.

The reconstructed $\text{Z} \to \ell\ell$ four-vector is combined with the $\text{h} \to \tau\tau$ four-vector based only on the visible τ decay products. The reconstructed visible mass, $m^{\text{vis}}_{\ell\ell\tau\tau}$, has a mass resolution of approximately 15% for an A boson with a mass of 300 GeV in all final states.

Accounting for the neutrinos associated with the leptonic and hadronic tau decays improves greatly the mass resolution of the reconstructed A boson candidate. In this search, the SVFIT algorithm [17, 18] provides an estimate of the four-vector of the SM-like h boson by marginalising a likelihood function that includes the matrix elements for the decays of the two tau leptons and the detector response for $\vec{p}^{\,\text{miss}}_{\text{T}}$. In this way the algorithm also determines the mass of the SM-like Higgs boson, denoted as $m^{\text{fit}}_{\tau\tau}$. A more accurate estimate of the A boson candidate mass $m^{\text{fit}}_{\ell\ell\tau\tau}$ stems from the improved estimate of the four-vector of the SM-like h boson: the mass resolution of $m^{\text{fit}}_{\ell\ell\tau\tau}$ is 10% for an A boson with a mass of 300 GeV.

A significant improvement in the mass resolution is achieved by giving the

measured mass of the SM-like Higgs boson (125 GeV) as an input to the SVFIT algorithm. As a result, we obtain a constrained estimate of the four-vector of the SM-like h boson that leads to a constrained value of its mass $m^{\mathrm{c}}_{\tau\tau}$. An even more precise estimate of the A boson candidate mass, denoted as $m^{\mathrm{c}}_{\ell\ell\tau\tau}$, is obtained by utilising this constrained estimate of the four-vector of the SM-like h boson. The mass resolution of $m^{\mathrm{c}}_{\ell\ell\tau\tau}$ is as good as 3% at 300 GeV.

The distributions of $m^{\mathrm{fit}}_{\ell\ell\tau\tau}$ and $m^{\mathrm{c}}_{\ell\ell\tau\tau}$ are displayed in Fig. 5.4 for the signal and background processes, and demonstrate the increased discrimination power of the reconstructed mass $m^{\mathrm{c}}_{\ell\ell\tau\tau}$. The measurement and grouping of the background processes are discussed in Sections 5.6 and 7, respectively. Moreover, the expected 95% confidence level (CL) model-independent limits are improved by approximately 40% by using $m^{\mathrm{c}}_{\ell\ell\tau\tau}$ instead of $m^{\mathrm{vis}}_{\ell\ell\tau\tau}$ to discriminate between the signal and background events. As a conclusion, we choose to produce the final results using $m^{\mathrm{c}}_{\ell\ell\tau\tau}$ as the discriminating variable between the signal and the background processes.

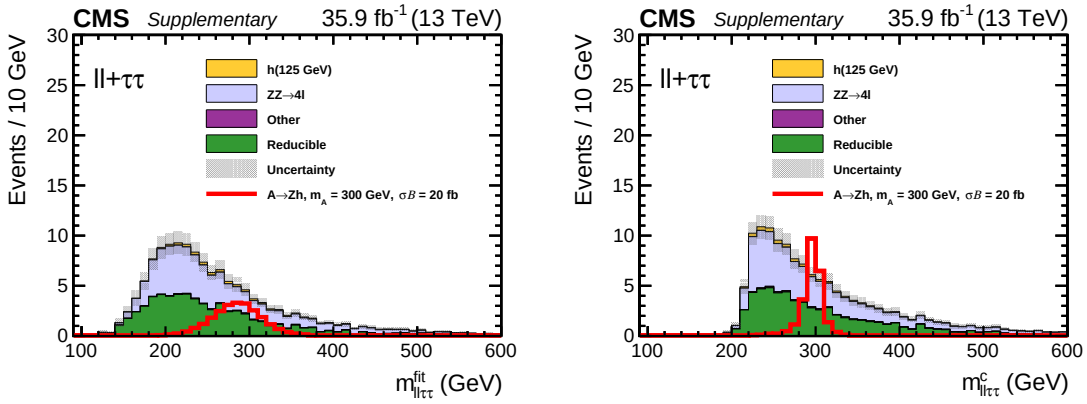

Figure 5.4: The reconstructed mass $m^{\mathrm{fit}}_{\ell\ell\tau\tau}$ (left) and $m^{\mathrm{c}}_{\ell\ell\tau\tau}$ (right) distributions and uncertainties before a background-only fit is performed simultaneously in all eight final states. All signal region selections except the requirement for the SM-like Higgs boson mass $m^{\mathrm{fit}}_{\tau\tau}$ to be within 90–180 GeV were applied. The eight final states are combined together only for visualization purposes. The uncertainties include both statistical and systematic components. The expected contribution from the A $\rightarrow$ Zh signal process is shown for a pseudoscalar Higgs boson with $m_{\mathrm{A}} = 300$ GeV with the product of the cross section and branching fraction of 20 fb and is for illustration only.

5.5.1 Optimisation of event selection

The event selection is optimised to further improve the high sensitivity of the analysis, obtained with the chosen A boson reconstruction. Additional information regarding the SM-like Higgs boson candidate is used to reduce the number of background events.

To gain sensitivity, the distribution of the chosen variable must provide discrimination between the signal and background processes. Selecting events based on the value of the constrained estimate of the h boson mass $m_{\tau\tau}^{\mathrm{c}}$ does not improve the sensitivity, because the shape of its distribution is similar for the signal and background events. Removing the mass constraint from the SVFIT algorithm results in the most likely mass of the SM-like Higgs boson candidate $m_{\tau\tau}^{\mathrm{fit}}$ that has a distinguishable shape for the signal processes with a resonance present at 125 GeV, whereas the reducible backgrounds have a broad distribution due to their nonresonant nature. Additionally, the dominant irreducible background from $\mathrm{ZZ} \to 4\ell$ ($\mathrm{qq} \to \mathrm{ZZ}$ and $\mathrm{gg} \to \mathrm{ZZ}$) is suppressed. This background has a $m_{\tau\tau}^{\mathrm{fit}}$ distribution concentrated near the Z boson mass, in contrast to the signal, as demonstrated in Fig. 5.5.

The signal sensitivity is increased by an additional 20% by requiring $m_{\tau\tau}^{\mathrm{fit}}$ to be within 90–180 GeV, because the contribution from $\mathrm{ZZ} \to 4\ell$ is considerably reduced, as also shown in Fig. 5.5. Approximately 60% of the events from the reducible and $\mathrm{ZZ} \to 4\ell$ background processes, selected as described in Section 5.3, are removed by this optimisation of the selection.

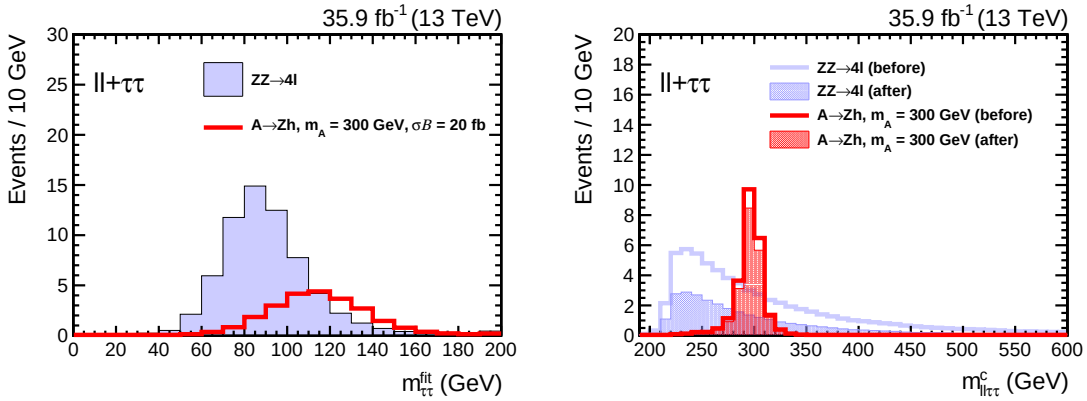

Figure 5.5: The reconstructed $m_{\tau\tau}^{\text{fit}}$ (left) and $m_{\ell\ell\tau\tau}^{\text{c}}$ (right) distributions for the dominant irreducible background from ZZ $\to 4\ell$ (blue), and for the A $\to$ Zh signal process (red). On the right, the reconstructed $m_{\ell\ell\tau\tau}^{\text{c}}$ distribution is shown before (line) and after (dashed) requiring $m_{\tau\tau}^{\text{fit}}$ to be within 90–180 GeV. The expected contribution from the A $\to$ Zh signal process is shown for a pseudoscalar Higgs boson with $m_{\text{A}} = 300$ GeV with the product of the cross section and branching fraction of 20 fb.

5.6 Background estimation

Estimating the background contribution plays an important role in every search: if the background contribution is not understood and modelled as correctly as possible, one can either lose a possibility for an observation, or alternatively, declare a false observation.

In this search, the irreducible and reducible backgrounds have similar contributions to the total background yield, i.e. approximately 50% of the total background contribution comes from the reducible backgrounds. The irreducible backgrounds have a final state indistinguishable from that of the signal process. The reducible backgrounds instead have at least one jet misidentified as an electron, muon, or τ_{h} candidate. Thus, the final state only appears to have the same components.

The dominant irreducible background contribution comes from the ZZ $\to 4\ell$. Other important background sources are the $\text{t}\bar{\text{t}}\text{Z}$, WWZ, WZZ, and ZZZ processes. As the final states include genuine leptons, they can be estimated from simulation.

The contributions from these processes are scaled by their theoretical cross sections calculated at the highest order available [38].

The production of the 125 GeV Higgs boson via the processes predicted by the SM form a small, yet important, irreducible background. These processes are also estimated from simulation, and the obtained yields scaled to the theoretical cross sections calculated at the highest order available. Their most accurate branching fractions are also included in the scaling. [38]

The dominant reducible background processes are $\mathrm{t\bar{t}}$, $\mathrm{Z}+\mathrm{jets}$, and $\mathrm{WZ}+\mathrm{jets}$. These processes result in jets that can be misidentified as τ candidates from the Higgs boson decay. Since the behaviour of jets is not perfectly simulated, the reducible background contribution is estimated using a data driven method, called "fake rate method".

The fake rate method is based on an assumption that the probability for a jet to be misidentified as a lepton is independent of the rest of the event. The method relies on studying how often a jet is misidentified as a lepton, i.e. on measuring the misidentification probabilities that are also called as *misidentification rates*. Weights based on the misidentification rates are applied to events with τ candidates failing the signal region identification and isolation criteria. This produces an estimate of the contribution from the reducible background processes in the signal region.

Estimating the contribution from the reducible background process is performed using in total three different event samples. All three event samples are independent from the signal region. First, the misidentification rates are measured in a "measurement region". Then, so-called closure tests are performed in a "validation region". The closure tests compare the observed and the estimated reducible background yields in a region enriched with the reducible background processes, without signal contamination. This is done to understand if the measured misidentification rates describe the jets misidentified as leptons outside of the measurement region.

Moreover, the closure tests help to derive systematic uncertainties that account for possible differences between the true and the estimated reducible background yields in the signal region. Finally, an "application region" is formed by events that fail the identification and isolation criteria required in the signal region. The misidentification rates are applied to these events to estimate the yield and the shape of the reducible background contribution. In the following subsections, I describe the details of the fake rate method used in this analysis.

5.6.1 Measuring the misidentification rates

In this analysis the measurement region is formed by a sample of Z + jet events. The estimation of misidentification rates relies on reconstructing an opposite-charge, same-flavor lepton pair compatible with a Z boson. One additional loosely defined lepton (electron, muon, or τ_{h} candidate) is required for measuring the misidentification rates.

The requirements on the leptons associated with the Z boson are the same as defined in Section 5.3, but they must fulfil a more stringent dilepton mass requirement, $81.2 < m_{\ell\ell} < 120\,\mathrm{GeV}$. This rejects especially electrons resulting from converted photons of final state radiation, and improves the purity of the measurement of the misidentification rates. The selection for the additional lepton is shown in Table 5.4 for each lepton type.

Once the $\mathrm{Z} \to \ell\ell$ decay has been reconstructed, the jet-to-lepton misidentification rate is estimated. The lepton algorithm is applied to the additional loosely defined lepton in the event to study how often these loosely defined leptons pass also the tighter identification and isolation criteria introduced in Section 5.3. Ideally, the misidentification rate would be computed as a ratio of the number of leptons passing the tight identification and isolation criteria, and the number of all loosely defined leptons. In reality the measurement is more complex due to contamination from

the WZ process, that results in lepton candidates that arise from genuine leptons. This reduces the purity of the measurement, as the genuine leptons often pass the tight identification and isolation criteria. To ensure that the misidentification rates are measured only for lepton candidates from jets ("fakes"), arising mainly from the Z + jets process, the WZ contribution is estimated and subtracted from data using a fit.

Table 5.4: Additional baseline selection applied to each lepton fake rate estimation. The event selections highlighted with blue are added to increase the purity of the measurement, and are not used when applying the fake rates.

Lepton	Additional denominator cuts
Electron	relative isolation (0.3) < 0.6,
	$81.2 < m_{\ell\ell} < 120\,\text{GeV}$,
	$min(m_{2l}) > 5\,\text{GeV}$,
	$max(iso_{\text{Z}_1}, iso_{\text{Z}_2}) < 0.14$, and
	$p_{\text{T}}^{\text{miss}} < 55\,\text{GeV}$ for $\lvert\eta\rvert < 1.479$
Muon	relative isolation (0.4) < 1.0,
	$81.2 < m_{\ell\ell} < 120\,\text{GeV}$,
	$m_{3l} < 250\,\text{GeV}$, and
	$p_{\text{T}}^{\text{miss}} < 55\,\text{GeV}$ for $\lvert\eta\rvert < 1.2$
τ_{h}	VVLoose Tau MVA ($\epsilon_{\text{id.+iso.}}^{\tau_{\text{h}}} = 95\%$)

The aim of the fit is to estimate the number of genuine and nongenuine leptons in two regions consisting of events that pass and fail the tight identification and isolation criteria. This information is necessary to extract the misidentification rates from the numbers of nongenuine leptons both in the passing and failing region:

$$f = \frac{\text{Number of nongenuine leptons in the passing region}}{\text{Number of nongenuine leptons in the passing and failing regions}}. \quad (5.1)$$

Templates formed by the simulated events with genuine and nongenuine leptons are utilised in the fit. Moreover, the transverse mass m_{T} of lepton and missing

transverse momentum is used to discriminate between the templates for distributions of genuine and nongenuine leptons. The discriminating variable is defined as $m_{\mathrm{T}} = \sqrt{2p_{\mathrm{T}}^{\ell}p_{\mathrm{T}}^{\mathrm{miss}}(1-\cos(\phi_{\ell}-\phi_{miss}))}$. In this fit p_{T}^{ℓ} is set to 35 GeV to avoid any bias in the measurement from correlations between the misidentification probability, that depends on p_{T}, and the fitted variable. Only the lepton's direction is used.

The misidentification rates are measured as a function of lepton p_{T}, and the fit is performed simultaneously to the passing and failing regions in each p_{T} bin. Since the lepton reconstruction can result in different misidentification rates depending on the detector region, the measurement of misidentification rates is performed in two bins of lepton $|\eta|$, corresponding to the barrel and endcap regions. For the τ_{h} candidates, reconstructed decay modes are used instead of the tau lepton η. The misidentification rates derived using the fit are compared to the ones from simulated events. As shown in Fig. 5.6 for electrons and muons in the barrel region, and taus with 1-prong+π^0s decay mode, the obtained misidentification rates are compatible within the statistical uncertainties. The obtained misidentification rates for electrons (muons) are <5 (10)% both in barrel and endcap regions for lepton $p_{\mathrm{T}} > 10$ GeV, whereas for τ_{h} candidates the misidentification rates vary between 15–30% for τ_{h} candidate $p_{\mathrm{T}} > 20$ GeV depending on the decay mode.

5.6.2 Estimating the yield and the shape of the reducible background processes

To estimate the reducible background contribution in any region, a weight is applied on events where at least one of the τ candidates fail the identification and isolation criteria. Since the studied final states can have up to two τ candidates faked by jets, we will consider cases where either one or both of the the τ candidates do not fulfil the identification and isolation criteria.

The precise formulation of the weight depends on how many τ candidates fail

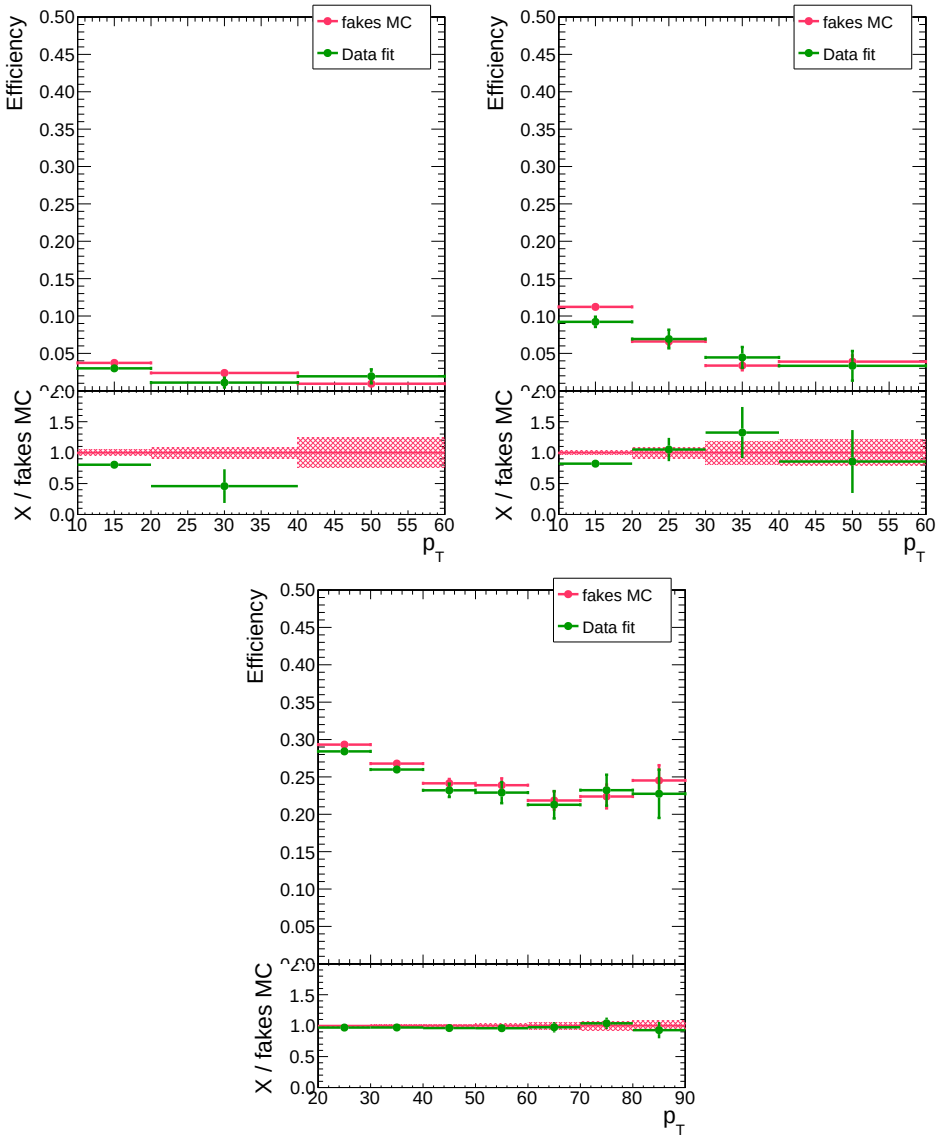

Figure 5.6: Misidentification rates as a function of p_{T} (GeV) for electrons (top left) and muons (top right) in the barrel region, and for τ_{h} candidates with 1-prong+π^0s decay mode (bottom). Here "fakes MC" stands for the misidentification rates measured from simulated Z + jets and $\mathrm{t\bar{t}}$ events, whereas the "Data fit" stands for the misidentification rates obtained as a result of the fit described in the text.

the identification and isolation criteria. These weights can be derived by studying the number of events with certain number of τ candidates failing the identification and isolation criteria: N_{2F}, N_{1F}, N_{0F} standing for two, one, and zero τ candidates

failing the required criteria. Assuming that the efficiency for prompt leptons is 100%, these event yields can be written in terms of the event numbers from Z + jets (N_{jj}) and WZ (N_j) processes, and misidentification rate f. Our goal is to derive an expression for N_{0F} to understand the reducible background contribution in the signal region that has two τ candidates passing the criteria:

$$N_{0F} = \text{Both } \tau \text{ candidates pass the criteria} = N_{2\ell} + fN_j + f^2 N_{jj}. \tag{5.2}$$

Let us start by solving the number of events with two jets, i.e. N_{jj}, which is related only to N_{2F}:

$$\begin{aligned} N_{2F} &= \text{Both } \tau \text{ candidates fail the criteria} = (1-f)^2 N_{jj} \\ \Rightarrow N_{jj} &= \frac{1}{(1-f)^2} N_{2F}. \end{aligned} \tag{5.3}$$

Using this information, we can also solve N_j from the equation for N_{1F}:

$$\begin{aligned} N_{1F} &= \text{Either of the } \tau \text{ candidates fail the criteria} \\ &= (1-f)N_j + f(1-f)N_{jj} + f(1-f)N_{jj} \\ &= (1-f)N_j + 2f(1-f)N_{jj} \\ &= (1-f)N_j + \frac{2f}{(1-f)} N_{2F} \\ \Rightarrow N_j &= \frac{1}{(1-f)} N_{1F} - \frac{2f}{(1-f)^2} N_{2F}. \end{aligned} \tag{5.4}$$

Using Eqs. 5.3 and 5.4, the number of events in the signal region becomes

$$\begin{aligned} N_{0F} &= N_{2\ell} + fN_j + f^2 N_{jj} \\ &= N_{2\ell} + \frac{f}{(1-f)} N_{1F} - \frac{2f^2}{(1-f)^2} N_{2F} + \frac{f^2}{(1-f)^2} N_{2F} \\ &= N_{2\ell} + \frac{f}{(1-f)} N_{1F} - \frac{f^2}{(1-f)^2} N_{2F}. \end{aligned} \tag{5.5}$$

In order to estimate the yield, events with exactly one object failing the identification and isolation criteria must receive a weight $f/(1-f)$. This includes the contribution from the WZ + jets process, where the Z boson candidate is expected

to be accompanied by one genuine lepton and one jet misidentified as a lepton. As shown in Eq. 5.4, also $\mathrm{t\bar{t}}$ and $\mathrm{Z}+\mathrm{jets}$ processes contribute to N_{1F} when either of the two jets passes the identification and isolation criteria even if neither of them is a genuine lepton. As a result, the estimate from weighted N_{1F} events introduces double counting of events from $\mathrm{t\bar{t}}$ and $\mathrm{Z}+\mathrm{jets}$ processes:

$$\frac{f}{(1-f)}N_{1F} = fN_j + 2f^2N_{jj}. \tag{5.6}$$

A weight with a negative sign is thus necessary for events with both objects failing the identification and isolation criteria, $-f_1f_2/[(1-f_1)(1-f_2)]$. This removes the double-counted events from $\mathrm{t\bar{t}}$ and $\mathrm{Z}+\mathrm{jets}$ processes.

The subtraction, however, introduces increased statistical uncertainties on the estimated yield of the reducible background. The statistical uncertainties further complicate the estimation of the distribution of the reducible background, when individual bins are used in the signal extraction described more in detail in Section 6.2. Two methods were evaluated to control the statistical uncertainties: taking the shape from another region, or removing the subtraction causing the large uncertainties. For this analysis, extensive studies were performed to select the most optimal approach. In the following subsections I introduce these methods more in detail.

Taking the shape from alternative control region

Since the yield is estimated correctly by the derived weights, it is possible to estimate the shape of the $m^{\mathrm{c}}_{\ell\ell\tau\tau}$ distribution of the reducible background from data in another region with negligible signal and irreducible background contributions. In this analysis, the region is defined similarly to the signal region but with same-sign τ candidates. Identification and isolation requirements are also partially relaxed, yielding a higher number of events available for the shape estimation. The resulting $m^{\mathrm{c}}_{\ell\ell\tau\tau}$ distribution, with a smooth shape, is normalised to the estimated yield of the reducible background contribution in the signal region.

In the signal region, the constituents of the reducible background contribution depend on the final state. In the $\ell\ell + \tau_h\tau_h$ final states, the dominant source of the reducible background is $t\bar{t}$ and Z+jets processes. In $\ell\ell+\ell\tau_h$ final states, the reducible background contribution consist of approximately 60% of WZ + jets and 40% of $t\bar{t}$ and Z + jets. However, the region used for the shape of the reducible background is enriched mainly with $t\bar{t}$ and Z + jets processes, and negligible contribution from WZ + jets process. As a consequence, the estimated shape of the distribution can be biased.

The bias was studied by producing model-independent 95% CL upper limits in the signal region to quantify how sensitive the final result is to the exact shape of the reducible background. Two different shapes were compared. The first shape is estimated as described above from data events with loose selection ("SS data"). The second shape comes from a combination of the data events and simulated WZ + jets events with opposite-sign τ candidates, weighted to the expected contributions: 40% data events with loose selection, and 60% of simulated WZ + jets events ("40% SS data + 60% WZ").

In this study, the observed data were replaced by pseudo-data, i.e. the expected background contribution. The shape of the reducible background was initially taken from the same-sign data events. Next, the shape of the reducible background contributing to the pseudo-data was replaced by the second shape ("40% SS data + 60% WZ"). Both expected and observed 95% CL upper limits were produced to reveal the level of a possible bias. The expected limits rely on the same-sign data events for the shape of the reducible background, whereas the observed limits are obtained using the second shape for the reducible background.

The obtained upper limits are shown in Fig. 5.7. Some differences are observed especially in the low masses, but the differences at higher masses are relatively small. These lower masses were studied more closely by checking the relative difference be-

tween the limits and comparing them to the 68(95)% confidence intervals of the upper limit obtained with the shape from the same-sign (SS) data events. The observed differences are much smaller than the confidence intervals, and thus acceptable.

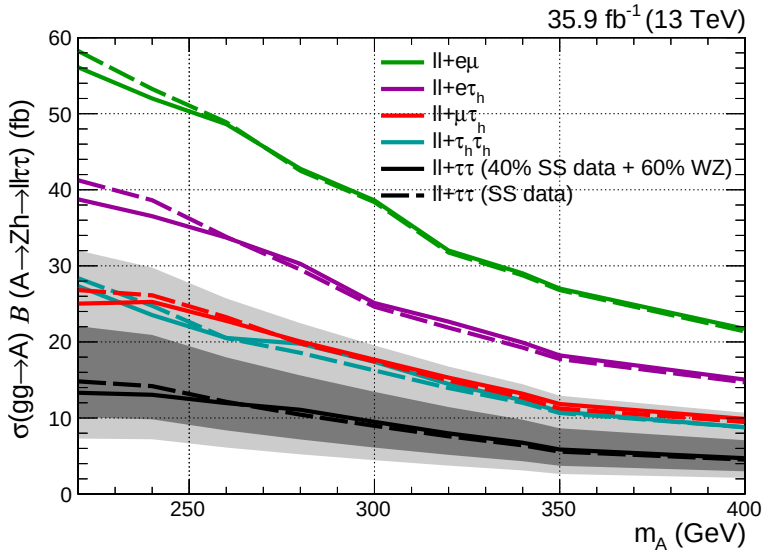

Figure 5.7: Model-independent 95% CL upper limits obtained with two different possible shapes for the reducible background: 40% SS data + 60% simulated WZ + jets events (solid line) and SS data (dashed line). The 68 (95)% confidence intervals are shown in dark (light) grey for the upper limit obtained using the SS data events for the shape.

Using simulated events for the WZ process

Large statistical uncertainties are caused by the double counting of events with two misidentified τ candidates, introduced in the weight given in Eq. 5.4. The statistical uncertainties can be reduced considerably by removing the weight responsible for the double counting, and by only estimating the contribution from processes with two misidentified τ candidates by the fake rate method. As a result, only events with two misidentified τ candidates receive a suitable nonzero weight, i.e. $f_1 f_2/[(1-f_1)(1-f_2)]$. Since the events with a single object failing the identification and

isolation criteria are not predicted by this alternative method, these events must be predicted from simulation.

As the statistical uncertainties are smaller, same events that provide the estimated yield of the reducible background can be also used to extract the shape of the $m^{c}_{\ell\ell\tau\tau}$ distribution. Thus, there is no bias on the background shape prediction unlike in the aforementioned method.

The alternative approach, however, is expected to slightly underestimate the yield of the reducible background contribution. This is a result of the decision to not to predict events with a single τ candidate failing the identification and isolation criteria. The case where either of the Z boson decay products is in fact a misidentified jet is not covered by this method as the simulated WZ process has a genuine Z candidate. This flaw could be covered for by implementing the fake rate method also for the leptons associated with the Z boson. The level of the underestimation is further demonstrated in the next subsubsection, where these two methods are compared.

Comparison of the two methods

As both methods are known to provide a reasonable estimate of the shape of the reducible background, the comparison between the two methods is performed studying the predicted yield of the reducible background contribution in both cases. In the following, the method predicting also the cases with a single τ candidate failing the selection is called "Fully data driven", whereas the alternative method relying on the simulated WZ process is called "Data driven+WZ MC". *This comparison was done before finalising the systematic uncertainties of the analysis. However, the conclusions presented below remain reliable, as only small modifications entered the analysis for the final results.*

An additional systematic uncertainty of 20% is added to the WZ contribution

in the Data driven+WZ MC method for all final states except $\ell\ell + \tau_h\tau_h$ where the contribution is close to negligible. Otherwise only the statistical uncertainties are considered. The yields and their difference is shown in Table 5.5. As expected, the fully data driven method has larger statistical uncertainties, as well as larger predicted yield (except in $\ell\ell + \tau_h\tau_h$ channels).

Table 5.5: Comparison of the predicted yields of the reducible background contribution for two methods: fully data driven and data driven+WZ MC. As the WZ process contributes up to 60% in the $\ell\ell + \ell\tau_h$ and $\ell\ell + e\mu$ channels, an additional systematic uncertainty of 20% is added to the WZ contribution. The statistical uncertainties in these channels are given in the parenthesis.

Final state	Fully data driven	Data driven+WZ MC	Difference of yields
$ee + e\tau_h$	3.11 ± 0.91	1.16 ± 0.16 (0.11)	1.96 ± 0.92
$\mu\mu + e\tau_h$	2.71 ± 0.93	1.74 ± 0.18 (0.13)	0.97 ± 0.95
$ee + \mu\tau_h$	4.0 ± 1.2	2.63 ± 0.26 (0.23)	1.4 ± 1.3
$\mu\mu + \mu\tau_h$	5.2 ± 1.4	3.61 ± 0.30 (0.27)	1.6 ± 1.4
$ee + \tau_h\tau_h$	3.3 ± 1.6	4.34 ± 0.59	-1.0 ± 1.7
$\mu\mu + \tau_h\tau_h$	4.2 ± 2.1	7.63 ± 0.86	-3.4 ± 2.3
$ee + e\mu$	0.77 ± 0.22	0.19 ± 0.13 (0.04)	0.58 ± 0.25
$\mu\mu + e\mu$	1.00 ± 0.26	0.14 ± 0.12 (0.03)	0.85 ± 0.29

For most channels, the yields are in agreement within the uncertainties. There are, however, large differences in channels where the h boson decays into at least one light lepton (electron or muon). To understand better where the minor differences in the yields arise, a tight selection on the Z boson mass was placed for these final states, i.e. $81.2\,\text{GeV} < m_{\ell\ell} < 101.2\,\text{GeV}$. This is done to account for the fact that the Data driven+WZ MC method is expected to underestimate the yield in cases where either of the Z boson decay products is a misidentified jet. The result of this study is shown in Table 5.6. Since applying the selection on the Z boson mass improves the agreement, we can conclude the majority of the differences in the yields are due to the known flaw in the Data driven+WZ MC method. This gives confidence that

the Data driven+WZ MC method can be further improved by implementing the fake rate method also for the leptons associated with the Z boson, as previously discussed.

Table 5.6: Comparison of the predicted yields of the reducible background contribution for two methods: fully data driven and data driven+WZ MC. The difference in the yields are shown before and after the tight Z boson mass selection. As the WZ process contributes up to 60% in the $\ell\ell+\ell\tau_{\mathrm{h}}$ and $\ell\ell+\mathrm{e}\mu$ channels, an additional systematic uncertainty of 20% is added to the WZ contribution. The statistical uncertainties in these channels are given in the parenthesis.

Final state	Fully data driven	Data driven+WZ MC	Difference of yields	
			$\lvert m_{\ell\ell} - m_{\mathrm{Z}}\rvert < 30\,\mathrm{GeV}$	$\lvert m_{\ell\ell} - m_{\mathrm{Z}}\rvert < 10\,\mathrm{GeV}$
$\mathrm{ee}+\mathrm{e}\tau_{\mathrm{h}}$	2.04 ± 0.79	1.01 ± 0.16 (0.10)	1.96 ± 0.92	1.03 ± 0.81
$\mu\mu+\mathrm{e}\tau_{\mathrm{h}}$	1.47 ± 0.70	1.57 ± 0.18 (0.13)	0.97 ± 0.95	-0.10 ± 0.72
$\mathrm{ee}+\mu\tau_{\mathrm{h}}$	3.2 ± 1.1	2.24 ± 0.24 (0.21)	1.4 ± 1.3	1.0 ± 1.1
$\mu\mu+\mu\tau_{\mathrm{h}}$	2.8 ± 1.1	3.09 ± 0.28 (0.25)	1.6 ± 1.4	-0.3 ± 1.1
$\mathrm{ee}+\mathrm{e}\mu$	0.40 ± 0.16	0.13 ± 0.12 (0.03)	0.58 ± 0.25	0.27 ± 0.20
$\mu\mu+\mathrm{e}\mu$	0.83 ± 0.23	0.11 ± 0.12 (0.03)	0.85 ± 0.29	0.72 ± 0.26

As a final comparison, we produce the expected 95% CL model-independent limits. The upper limits are shown for all eight final states combined in Fig. 5.8, demonstrating that the two methods result in consistent expected 95% CL model-independent limits. However, since the fully data driven method is expected to give a more accurate estimate of the yield of the reducible background, the final results are produced using the said method.

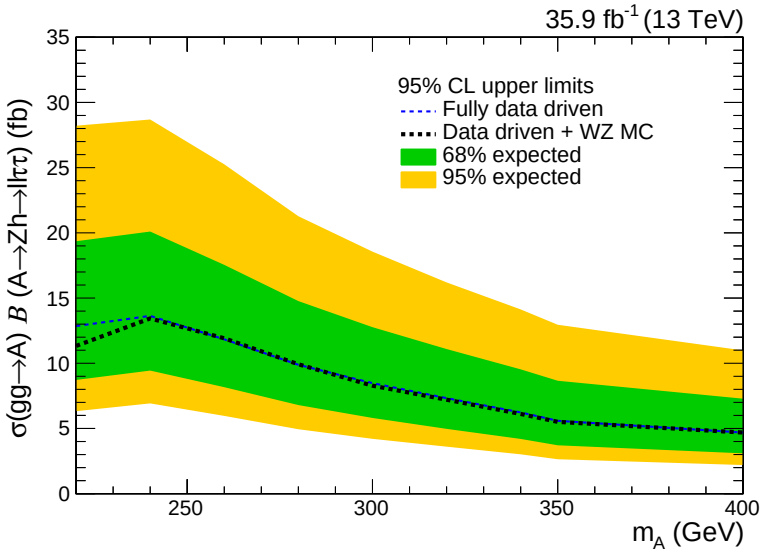

Figure 5.8: Model-independent combined 95% CL upper limits obtained with two different fake rate methods: fully data driven (blue dashed line) and data driven +WZ MC (black dashed line). The 68(95)% confidence intervals are shown in dark (light) grey for the upper limit obtained with fully data driven method. The limits are given for all eight final states combined.

5.6.3 Validation of the measured misidentification rates

The measured misidentification rates, and the chosen method used to apply them with, are validated in a region enriched by jets. In this analysis, the validation region is defined similarly to the signal region but with same-sign τ candidates to ensure that the validation region is independent of the signal region. This requirement also reduces contributions from the irreducible background contributions, making the region ideal for understanding how well the measured misidentification rates describe the behaviour of jets.

The reconstructed $m^c_{\ell\ell\tau\tau}$ distribution in this validation region is shown in Fig. 5.9 before and after a background-only fit. The grouping of the background processes are discussed in Section 7. Modest differences in observed versus predicted reducible background yields are observed, resulting in a systematic uncertainty in the yield. A uncertainty in the yield is taken to be 40% which is conservative enough

to cover the observed nonclosure, as shown in Fig. 5.9. This uncertainty is uncorrelated between the $\ell\ell + \mathrm{e}\tau_\mathrm{h}$, $\ell\ell + \mu\tau_\mathrm{h}$, $\ell\ell + \tau_\mathrm{h}\tau_\mathrm{h}$, and $\ell\ell + \mathrm{e}\mu$ channels. Further studies confirmed that the final results of this analysis are not sensitive to the exact size chosen for this systematic uncertainty.

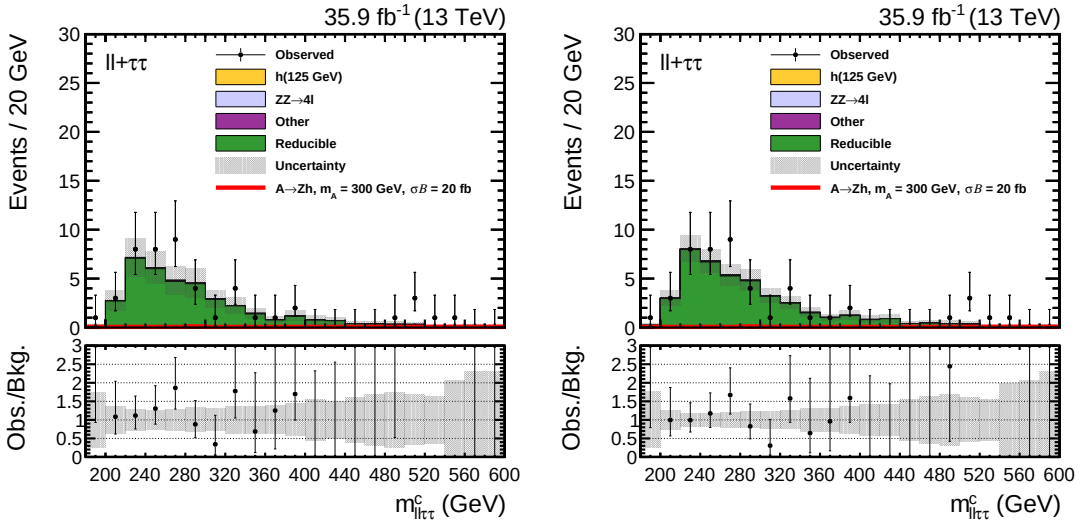

Figure 5.9: The reconstructed $m^c_{\ell\ell\tau\tau}$ distribution before (left) and after (right) a background-only fit in the validation region. The optimisation of the selection based on $m^{\mathrm{fit}}_{\tau\tau}$ was removed. The uncertainties include both statistical and systematic uncertainties. The expected contribution from the $\mathrm{A} \to \mathrm{Zh}$ signal process is shown for a pseudoscalar Higgs boson with $m_\mathrm{A} = 300\,\mathrm{GeV}$ with the product of the cross section and branching fraction of 20 fb and is for illustration only.

Another validation region can be defined based on the signal region, but with inverted selection on the reconstructed Higgs boson mass $m^{\mathrm{fit}}_{\tau\tau}$. Requiring $m^{\mathrm{fit}}_{\tau\tau} < 90\,\mathrm{GeV}$ produces a region where also the contribution from the irreducible background processes can be studied together with the reducible background processes. The reconstructed $m^c_{\ell\ell\tau\tau}$ distribution in this alternative validation region is shown in Fig. 5.10 before and after a background-only fit. A good agreement between the data and the predicted background contribution is confirmed.

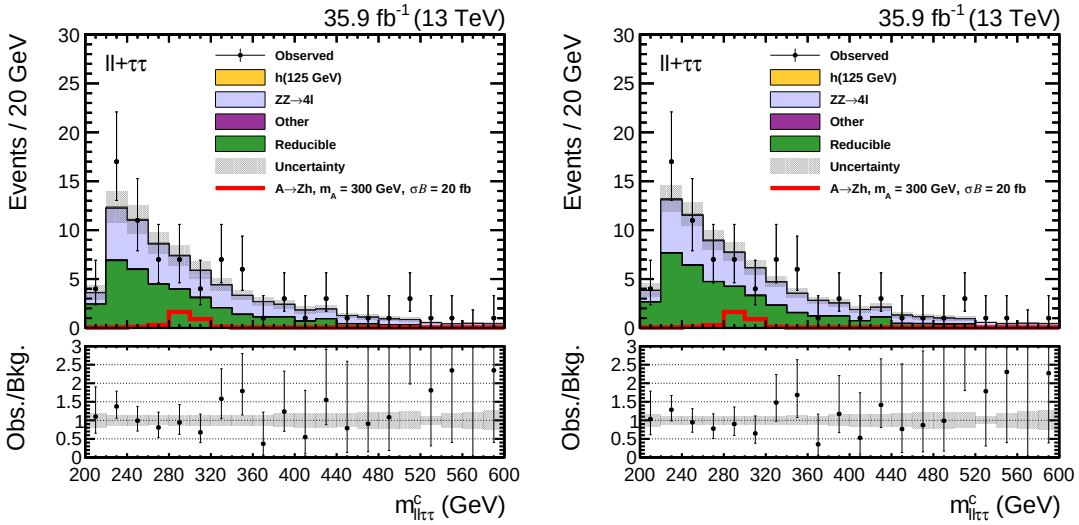

Figure 5.10: The reconstructed $m^{c}_{\ell\ell\tau\tau}$ distribution before (left) and after (right) a background-only fit in the validation region defined based on the signal region, but requiring $m^{\text{fit}}_{\tau\tau} < 90\,\text{GeV}$. The uncertainties include both statistical and systematic uncertainties. The expected contribution from the A $\rightarrow$ Zh signal process is shown for a pseudoscalar Higgs boson with $m_{\text{A}} = 300\,\text{GeV}$ with the product of the cross section and branching fraction of 20 fb and is for illustration only.

6. Systematic uncertainties and the signal extraction

In this search for the pseudoscalar A, results are produced based on the chosen discriminating variable, i.e. the reconstructed mass distribution of the pseudoscalar A in all eight final states. The reconstructed mass $m^{c}_{\ell\ell\tau\tau}$ distributions are used to compare the compatibility of the observed data and the estimated background, as well as setting 95% CL upper limits in multiple scenarios that constrain the models used to interpret the results.

To understand how well the observed data is described by the estimated background, it is important to account for the systematic uncertainties present in the analysis. This relies on estimating the systematic uncertainties and including them in the signal extraction. The finite number of events in the simulated samples result in statistical uncertainties, whereas systematic uncertainties arise for example from the experimental setup, or the choice of models in the MC simulations. Albeit this analysis is mostly limited by the statistical uncertainties, estimating the systematic uncertainties is a crucial task that is not to be overlooked.

This chapter consists of two parts. The systematic uncertainties present in this analysis are discussed first, followed by a description of the signal extraction method.

6.1 Systematic uncertainties

Systematic uncertainties can be divided into two categories: those that only scale the event yield (normalisation uncertainties), and those that affect both the yield and the shape of the studied distributions. In this section, I will introduce the uncertainties considered in this analysis. All uncertainties are summarised in Table 6.1. Unless otherwise mentioned, each uncertainty is assumed correlated between different final states and processes. Different uncertainties are treated as uncorrelated.

6.1.1 Normalisation uncertainties

Finite number of simulated events

The finite number of simulated events result in uncertainties that are treated using the Barlow-Beeston-lite method [146]. These uncertainties are taken into account in all bins of the background distributions used in the signal extraction. They are uncorrelated for bins of a single distribution, and across different samples.

The luminosity measurement

The uncertainty in the integrated luminosity amounts to 2.5% [147].

Lepton identification, isolation, and trigger efficiencies

Each identification and isolation efficiency measurement, performed to produce data-to-simulation correction factor, results in a systematic uncertainty to this analysis. The τ_{h} identification and isolation efficiency for genuine τ_{h} leptons results in the overall uncertainty of 5% [88], which includes also the usage of AGAINST-μ and AGAINST-E discriminants. A normalisation uncertainty of 2% for each electron or muon in the final state results from the uncertainties in the electron and muon identification and isolation efficiencies. As the effect of the uncertainty in the electron

and muon energy scales is negligible, those uncertainties are not considered in this analysis. The measurement of the trigger efficiency yields an uncertainty of 2% for both electron and muon triggers.

Vetoing events with a b-tagged jet

Efficiencies related to b jet identification differ for the data and simulated events. In principle, this results in a correction factor applied to simulated events, but in this analysis these corrections factors were not applied as the possible effect to final results would be minuscule. However, the systematic uncertainties related to vetoing events with a b-tagged jet are considered. For the background processes with heavy-flavor jets (from charm or bottom quarks), i.e., $t\bar{t}$, $t\bar{t}Z$, and $t\bar{t}W$, an uncertainty of 4.5% is applied. All other processes, including the signal process, are dominated by light-flavor jets (from other quarks or gluons). For these processes the uncertainty is 0.15%.

Theoretical uncertainties for signal and background processes

The only theoretical uncertainty applied to the simulated signal events is the uncertainty coming from the calculations of the SM $h \to \tau\tau$ branching fraction. The total size of this uncertainty is approximately 2% [38]. In addition to both the $gg \to A$ and $b\bar{b}A$ signal samples, this uncertainty is applied to all backgrounds that include the $h \to \tau\tau$ process.

The PDFs, and the renormalisation and factorisation (RF) scales, result in uncertainties that affect both the cross section and acceptance of the background processes estimated from simulation. In general, two separate uncertainties are derived from the PDFs, and the RF scales: one describing the uncertainty in the cross section, and the other for the uncertainty in the acceptance that followed from the change in the shape of the kinematic distributions. These uncertainties

are estimated from simulation, separately for each process. The uncertainty from the RF scales is evaluated by varying both scales by factors of 0.5 and 2.0, and computing the change in the process cross section and the acceptance. The extreme variations of (0.5, 2.0) and (2.0, 0.5) are excluded. These uncertainties are applied to $qq \to ZZ$, Zh production, and the subleading h boson processes (Wh, $gg \to h \to ZZ$, and $t\bar{t}h$).

In this analysis, the uncertainty in the cross section is assumed dominant compared to the uncertainty on the acceptance. Thus, the uncertainty in the acceptance is either considered correlated with the uncertainty in the cross section and thus estimated together, or fully neglected, as described below.

The $qq \to ZZ$ process has an uncertainty of 4.8%, obtained by combining the RF scale uncertainties with the PDF set uncertainty [148]. This uncertainty covers both uncertainties in the cross section and the acceptance. For Zh production, and the subleading h boson processes, the uncertainties take into account only the uncertainty in the cross section. For Zh (Wh) production, the uncertainty related to the PDFs is 1.6 (1.9)%, whereas the uncertainty for the variation of the RF scales amounts to 3.8 (0.7)% [38]. For the $gg \to h \to ZZ$ and $t\bar{t}h$ processes the uncertainties related to the PDFs are 3.2 and 3.6%, whereas the uncertainties for the variation of the RF scales amount to 3.9 and 7.5%, respectively [38].

The usage of the κ-factor to estimate the NNLO cross section results in an uncertainty of 10% for the $gg \to ZZ$ process. This uncertainty covers the PDF, RF scale uncertainties, and the uncertainty on the strong coupling constant. An additional 10% uncertainty is included to account for the assumptions used to estimate the NNLO cross section [140]. The uncertainties on rare processes ($t\bar{t}Z$, $t\bar{t}W$, and triboson production) are assumed to be 25%. This is a conservative estimate in the case of $t\bar{t}Z$ and $t\bar{t}W$ processes, for which the PDF, RF scale uncertainties, and the uncertainty on the strong coupling constant has been computed to amount to less

than 15% at NLO [38].

Uncertainties related to the fake rate method

The subtraction of the prompt lepton contribution results in uncertainties in the misidentification rates. Each uncertainty includes both a statistical and systematical component due to the limited number of events, and the templates used in the measurements, respectively. As the statistical uncertainty is much smaller compared to the systematical uncertainty, the uncertainties in the misidentification rates are propagated to the reducible background distributions as normalisation uncertainties, correlated across each bin in p_{T}. Thus, the statistical uncertainties, independent in each (p_{T}, η) bin, are neglected.

Another statistical uncertainty rises from the limited number of events forming the application region. However, since the shape of the reducible background distribution is estimated from same-sign data events, the statistical uncertainty in each bin represents the region from which the shape is taken, instead of the application region. In the nominal method, the statistical uncertainty related to the application region is neglected. In the alternative fake rate method, introduced in Section X, the statistical uncertainties related to the application region would be accounted for automatically.

An additional uncertainty of 40% is applied in the reducible background yield, considered to be uncorrelated across the $\ell\ell + \mathrm{e}\tau_{\mathrm{h}}$, $\ell\ell + \mu\tau_{\mathrm{h}}$, $\ell\ell + \tau_{\mathrm{h}}\tau_{\mathrm{h}}$, and $\ell\ell + \mathrm{e}\mu$ channels. This uncertainty is the dominant uncertainty related to the fake rate method. As discussed in Section 5.6, these uncertainties are based the results of the closure tests comparing the differences between the observed and the estimated reducible background yields.

6.1.2 Shape uncertainties

Tau lepton energy scale

An uncertainty of 1.2% on the tau lepton energy scale is applied for each τ_{h} candidate [88]. This uncertainty is propagated to the analysis through the SVFIT calculation, and thus it affects the mass distributions of both the signal and background processes. The uncertainty is assumed to be uncorrelated across the 1-prong, 1-prong+π^0s, and 3-prong decay modes.

The $\vec{p}_{\mathrm{T}}^{\,\mathrm{miss}}$ scale

The $\vec{p}_{\mathrm{T}}^{\,\mathrm{miss}}$ scale uncertainties [89] are also propagated to the analysis through the SVFIT calculation, and as a result, they affect the normalisation and the shape of the reconstructed mass distributions of simulated processes. Two separate uncertainties affect the $\vec{p}_{\mathrm{T}}^{\,\mathrm{miss}}$ calculation: the one arising from unclustered energy deposits in the detector, as well as the other from the jet energy scale measurement.

Table 6.1: Dominant sources of systematic uncertainties. The sign † marks the uncertainties that affect both the shape and normalisation of the final $m^{c}_{\ell\ell\tau\tau}$ distributions. Uncertainties that only affect the normalisations have no marker. For the shape and normalisation uncertainties, the magnitude column lists an approximation of the associated change in the normalisation of the affected processes.

Source of uncertainty	Process	Magnitude
τ_h id. & isolation	All simulated processes	5%
τ_h energy scale† (1.2% energy shift)	All simulated processes	<2%
e id. & isolation	All simulated processes	2%
e trigger	All simulated processes	2%
μ id. & isolation	All simulated processes	2%
μ trigger	All simulated processes	2%
b jet veto	All simulated processes	4.5% heavy flavor, 0.15% light flavor or gluon
$qq \to ZZ$ theoretical uncertainty	$qq \to ZZ$	4.8%
PDF set uncertainty	Zh, Wh, $gg \to h \to ZZ$, and $t\bar{t}h$	Varies from 1.6 to 3.6% (see text)
RF scale uncertainty	Zh, Wh, $gg \to h \to ZZ$, and $t\bar{t}h$	Varies from 0.7 to 7.5% (see text)
$gg \to ZZ$ uncertainties	$gg \to ZZ$	
theoretical uncertainty		10%
κ-factor (LO-to-NNLO)		10%
$t\bar{t}Z$ theoretical uncertainty	$t\bar{t}Z$	25%
$t\bar{t}W$ theoretical uncertainty	$t\bar{t}W$	25%
Triboson theoretical uncertainty	Triboson	25%
Theoretical uncertainty on $\mathcal{B}(h \to \tau\tau)$	Signal, Zh, and Wh	<2%
Reducible background uncertainties:	Reducible background	
e prompt lepton subtraction		<12% in $\ell\ell + e\mu$, <1% in $\ell\ell + e\tau_h$
μ prompt lepton subtraction		<16% in $\ell\ell + e\mu$, <1.5% in $\ell\ell + \mu\tau_h$
τ prompt lepton subtraction		<3.5% in $\ell\ell + e\tau_h$ and $\ell\ell + \mu\tau_h$, <1% in $\ell\ell + \tau_h\tau_h$
Normalisation		40% in $\ell\ell + e\tau_h$, $\ell\ell + \mu\tau_h$, $\ell\ell + \tau_h\tau_h$, and $\ell\ell + e\mu$
$\vec{p}_T^{\,miss}$ energy scale†	All simulated processes	<2%
Limited number of events	All background processes	Statistical uncertainty in individual bins
Integrated luminosity	All simulated processes	2.5%

6.2 Signal extraction

Both ATLAS and CMS experiments use a standardised approach for all Higgs boson analyses, where the 95% CL upper limits are set using the modified frequentist CLs methods [149–151]. In the approach, signal and background expectations, s and b, are defined as function of the nuisance parameters θ, that represent the uncertainties present in the analysis. Furthermore, the possible signal is represented by *a signal modifier* μ, which in this analysis is a product of the cross section and branching fraction of the A boson. The results are given in terms of the signal modifier.

The signal modifier and the nuisance parameters are accounted for in the likelihood function $\mathcal{L}(\text{data}|\mu,\theta)$, that describes the probability to observe the data assuming the given modelling of the signal, background, and the systematic uncertainties:

$$\begin{aligned}\mathcal{L}(\text{data}|\mu,\theta) &= \text{Poisson}(\text{data}|\mu\cdot s(\theta)+b(\theta))\cdot p(\tilde{\theta}|\theta)\\ &= \prod_i \frac{(\mu s_i+b_i)^{n_i}}{n_i!}e^{-\mu s_i-b_i},\end{aligned} \tag{6.1}$$

where the Poisson term is a product of Poisson probabilities in all bins of the reconstructed mass distribution. The term $p(\tilde{\theta}|\theta)$ is the probability density function of a systematic uncertainty, describing the probability to measure the nominal value of the nuisance parameter $(\tilde{\theta})$ given the true value (θ).

The next step is to compare the data with the background-only and signal-plus-background hypothesis to understand how well each hypothesis describe the data. Likelihood functions are constructed for each hypotheses, and a *profile likelihood ratio* is formed to distinguish between the two hypotheses:

$$q_\mu = -2\ln\frac{\mathcal{L}(\text{data}|\mu,\hat{\theta}_\mu)}{\mathcal{L}(\text{data}|\hat{\mu},\hat{\theta})},\ \text{requiring } 0\le\hat{\mu}\le\mu. \tag{6.2}$$

In the denominator the likelihood function is maximised, described by the maximum likelihood estimators $\hat{\mu}$ and $\hat{\theta}$. In the numerator the likelihood function is given for a fixed value of μ, accompanied by the conditional maximum likelihood estimator of

θ. The allowed values of the signal strength modifier are defined by physics (signal rate must be positive), and to ensure that upward fluctuations of data ($\hat{\mu} > \mu$) are not taken as an evidence against the signal hypothesis described by the fixed value of μ.

Producing the upper limits from Eq. 6.2 has multiple steps. First, the observed value of the test statistic is obtained from a fit for the given signal strength modifier. Next, the values of the nuisance parameters $\hat{\theta}_{\mu}^{\text{obs}}$ and $\hat{\theta}_{0}^{\text{obs}}$ are obtained by maximising the likelihood functions under the signal+background and background-only hypothesis. The upper limits are constructed by computing two probabilities, one associated with the observation for the signal+background and other for the back-ground only hypotheses, and studying the ratio of these probabilities:

$$\text{CL}_s(\mu) = \frac{\text{CL}_{s+b}(\mu)}{\text{CL}_b(\mu)} = \frac{p_\mu}{1-p_b} = \frac{P(q_\mu \geq q_\mu^{\text{obs}}|\mu, \hat{\theta}_\mu^{\text{obs}})}{P(q_\mu \geq q_\mu^{\text{obs}}|\mu = 0, \hat{\theta}_0^{\text{obs}})}, \tag{6.3}$$

where the probabilities are integrals over the probability density functions:

$$\begin{aligned} P(q_\mu \geq q_\mu^{\text{obs}}|\mu, \hat{\theta}_\mu^{\text{obs}}) &= \int_{q_\mu^{\text{obs}}}^{\infty} f(q_\mu|\mu, \hat{\theta}_\mu^{\text{obs}}) dq_\mu, \text{ and} \\ P(q_\mu \geq q_\mu^{\text{obs}}|\mu = 0, \hat{\theta}_0^{\text{obs}}) &= \int_{q_0^{\text{obs}}}^{\infty} f(q_\mu|0, \hat{\theta}_0^{\text{obs}}) dq_\mu. \end{aligned} \tag{6.4}$$

These probability density functions are obtained by generating toy Monte Carlo pseudo-data, with the fixed values of $\hat{\theta}_{\mu}^{\text{obs}}$ and $\hat{\theta}_{0}^{\text{obs}}$, for the signal+background and background-only hypotheses, respectively. When evaluating the test statistic, they are able to float freely. The observed 95% CL upper limit is then computed as $\text{CL}_s(\mu) \leq 5\%$. The expected 95% CL upper limit and the uncertainty bands are obtained by generating toy Monte Carlo pseudo-data under the background-only hypothesis, and calculating $\text{CL}_s(\mu)$ for each of them. A cumulative probability distribution of results is then built to define the median expected upper limit (50% quantile), the $\pm 1\sigma$ bands (16% and 84% quantiles), and the $\pm 2\sigma$ bands (2.5% and 97.5% quantiles).

Using the toy Monte Carlo pseudo-data is computationally time-consuming,

and thus the asymptotic approximation of the described method is preferred [151, 152]. The approach is based on the Wilks' theorem, which states that in the asymptotic approximation q_μ has half a χ^2 distribution for one degree of freedom. As a result, finding μ so that $q_\mu = 3.84$, yields $\mathrm{CL}_s = 0.05$ when the observed number of events match exactly the expected number of events. Thus, there would be no need to generate toy Monte Carlo pseudo-data to obtain the expected 95% CL upper limit.

If we require $\hat{\mu} > 0$, the probability density functions given in Eq. 6.4 follow another known formulae [151, 152]. This approach relies on a suggestion that a single data set, referred to as the Asimov data set, can represent all data sets generated under background-only hypothesis. The test statistic of Eq. 6.2 for the Asimov data set is obtained by replacing the observed event yield in each bin of the studied distribution with the expected number of events. The test statistic $q_{\mu,A}$ has also the form

$$q_{\mu,A} = \frac{\mu^2}{\sigma^2}, \tag{6.5}$$

where μ is the numerical value that produces $\mathrm{CL}_s = 0.05$. Morever, due to Wilks' theorem, σ (the spread of μ) can be simply computed as $\sigma^2 = \mu^2/q_{\mu,A} = \mu^2/3.84$.

Due to the well-defined probability density functions, asymptotic relations yield an upper limit for the CL_s method:

$$\mathrm{CL}_s = 0.05 = \frac{1 - \Phi(\sqrt{q_\mu})}{\Phi(\sqrt{q_{\mu,A}} - \sqrt{q_\mu})}, \tag{6.6}$$

where Φ is the cumulative distribution of a standard Gaussian, and q_μ ($q_{\mu,A}$) is the test statistic evaluated with the observed (Asimov) data set.

This analysis uses the asymptotic approximation of the modified frequentist CLs methods to calculate the 95% CL upper limits. A program used widely in the CMS Collaboration provides the limit computation. First, a fit is performed to both observed and Asimov data sets to obtain the μ values that maximise the corresponding likelihood functions, i.e. $\hat{\mu}$ and $\hat{\mu}_A$, respectively. Next, the value of

μ that produces $\mathrm{CL}_s = 0.05$ is found by scanning over possible μ values. This is repeated for each studied signal mass point to obtain the observed 95% CL upper limit.

The median expected 95% CL_s limit and the uncertainty bands are computed from

$$\mu_{\mathrm{up}+N} = \sigma(\Phi^{-1}(1 - \alpha\Phi(N)) + N), \tag{6.7}$$

with $\alpha = 0.05$ and suitable value of N: $N = 0$ for the median expected upper limit, and $N = \pm 1$ ($N = \pm 2$) for the 1σ (2σ) band. The median expected upper limits is thus

$$\mu_{\mathrm{up}}^{\mathrm{med}} = \sigma(\Phi^{-1}(1 - 0.5\alpha) = \sigma\Phi^{-1}(0.975). \tag{6.8}$$

7. Results

The reconstructed pseudoscalar Higgs boson mass, $m^{c}_{\ell\ell\tau\tau}$, is used as the discriminating variable between the signal and the background processes. The $m^{c}_{\ell\ell\tau\tau}$ distributions in each of the eight final states are utilised in a combined analysis to search for excesses above the standard model background expectations, possibly indicating the existence of the A boson, and to set the model-independent and model-dependent 95% CL upper limits.

The distribution of the reconstructed mass $m^{c}_{\ell\ell\tau\tau}$ is extended outside the studied signal mass range: the distribution ranges from 200 to 600 GeV, but the studied signal mass points are between 220 and 400 GeV. The additional information on the background distributions can constrain the corresponding parameters in the simultaneous fit. Moreover, a possible signal could have a wide width especially at higher masses, which must be accommodated in the distribution.

Each of the eight final states results in a distribution that is treated separately from others in the simultaneous fit. When displaying the results, they are combined together but only for visualisation purposes. Additionally, background processes are grouped as follows:

- "h(125 GeV)" includes all processes with the SM Higgs boson (including $gg \to h \to ZZ \to 4\ell$),
- "$ZZ \to 4\ell$" includes events from $qq \to ZZ$ and $gg \to ZZ$ processes,
- "Other" includes events from triboson, $t\bar{t}Z$, and $t\bar{t}W$ production, and

- "Reducible" includes the reducible background contribution.

The $m^{\mathrm{c}}_{\ell\ell\tau\tau}$ distributions for each of the four h boson decay channels, adding the $\mathrm{Z} \to \ell\ell$ channels together, are shown in Fig. 7.1. The $m^{\mathrm{c}}_{\ell\ell\tau\tau}$ distribution for all eight final states together can be seen in Fig. 7.2. The distributions are shown after a background-only fit to data and include both statistical and systematic uncertainties. No excess above the standard model background expectations is observed in data. A minor trend is seen in the ratio of the data and background estimation for A boson masses below 320 GeV. Since the validation of the background prediction demonstrated in Figs. 5.9 and 5.10 show a good agreement between the data and background contribution, the trend can be caused by a statistical fluctuation. The predicted signal and background yields are given in Table 7.1 together with the number of observed events for each of the four Zh channels.

Table 7.1: Background and signal expectations together with the numbers of observed events, for the signal region distributions after a background-only fit. The expected contribution from the $\mathrm{A} \to \mathrm{Zh}$ signal process is given for a pseudoscalar Higgs boson with $m_{\mathrm{A}} = 300\,\mathrm{GeV}$ with the product of the cross section and branching fraction of 20 fb. The background uncertainty accounts for all sources of uncertainty, systematic as well as statistical, after the simultaneous fit.

Process	$\ell\ell + \mathrm{e}\tau_{\mathrm{h}}$	$\ell\ell + \mu\tau_{\mathrm{h}}$	$\ell\ell + \tau_{\mathrm{h}}\tau_{\mathrm{h}}$	$\ell\ell + \mathrm{e}\mu$
h(125 GeV)	0.77±0.02	1.39±0.03	1.28±0.04	0.45±0.01
$\mathrm{ZZ} \to 4\ell$	6.48±0.13	11.38±0.25	7.59±0.20	4.57±0.09
Other	0.10±0.01	0.24±0.02	0.04±0.01	0.69±0.04
Reducible	5.52±0.42	9.12±0.93	6.68±0.65	2.04±0.24
Total background	12.88±0.45	22.13±0.94	15.58±0.68	7.74±0.28
$\mathrm{A} \to \mathrm{Zh}$, $m_{\mathrm{A}} = 300\,\mathrm{GeV}$, $\sigma\mathcal{B} = 20\,\mathrm{fb}$	4.13±0.18	7.32±0.30	7.01±0.40	2.26±0.10
Observed	13	22	14	12

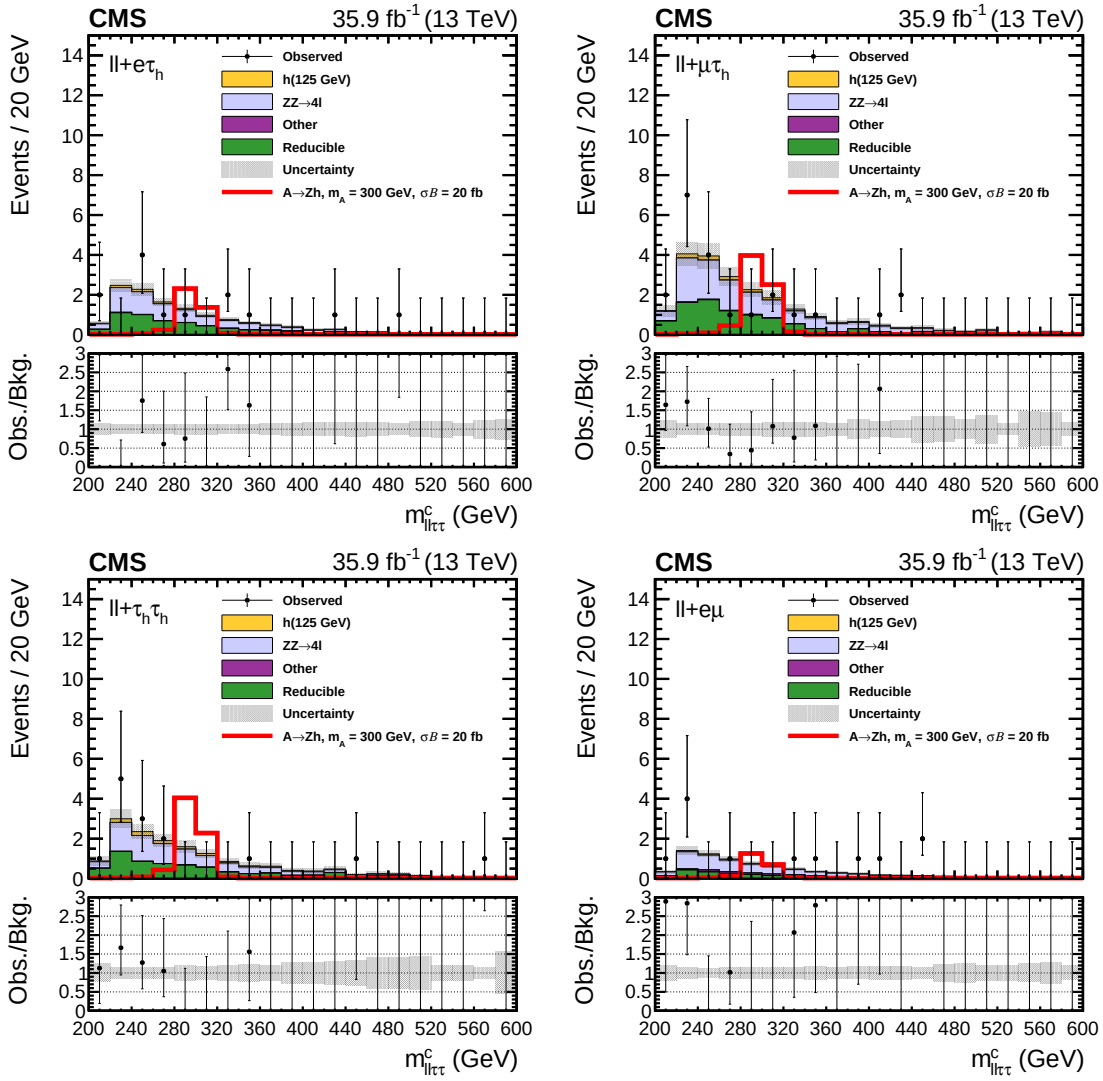

Figure 7.1: The reconstructed mass $m^{c}_{\ell\ell\tau\tau}$ distributions and uncertainties after a background-only fit for the $\ell\ell + e\tau_h$ (upper left), $\ell\ell + \mu\tau_h$ (upper right), $\ell\ell + \tau_h\tau_h$ (lower left), and $\ell\ell + e\mu$ (lower right) channels. In all cases the two decay channels of the Z boson are included as separate distributions in the simultaneous fit; combining them together is for visualisation purposes only. The uncertainties include both statistical and systematic components. The expected contribution from the $A \to Zh$ signal process is shown for a pseudoscalar Higgs boson with $m_A = 300\,\text{GeV}$ with the product of the cross section and branching fraction of 20 fb and is for illustration only.

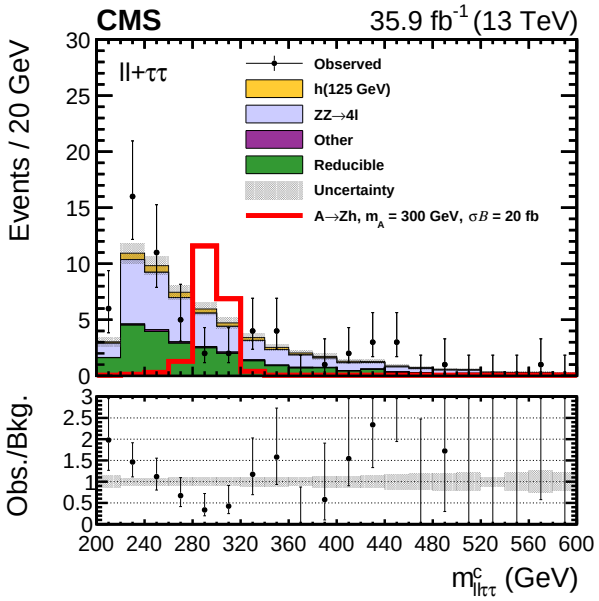

Figure 7.2: The reconstructed mass $m^{c}_{\ell\ell\tau\tau}$ distribution and uncertainties after a background-only fit in all eight final states. The final states are included as separate distributions in the simultaneous fit; combining them together is for visualisation purposes only. The uncertainties include both statistical and systematic components. The expected contribution from the $A \to Zh$ signal process is shown for a pseudoscalar Higgs boson with $m_A = 300\,\text{GeV}$ with the product of the cross section and branching fraction of 20 fb and is for illustration only.

The model-independent 95% CL upper limits are set on the product of the cross section and branching fraction, $\sigma(gg \to A)\mathcal{B}(A \to Zh \to \ell\ell\tau\tau)$, and are consistent with the absence of any signal, as demonstrated in Fig. 7.3. The obtained model-independent 95% CL upper limits reflect the trend seen in Fig. 7.2, discussed above.

The model-dependent 95% CL upper limits are set in two MSSM benchmark scenarios, the hMSSM and the low-tb-high. For both MSSM scenarios, limits were set considering both the $gg \to A$ and $b\bar{b}A$ production processes. In some parameter space regions, the $b\bar{b}A$ cross section is not negligible, and thus the estimated $b\bar{b}A$ contribution must be included when setting model-dependent limits. The cross sections depend on m_A and $\tan\beta$ values. For reference, at $m_A = 300\,\text{GeV}$ and $\tan\beta = 4$, the ratio of process cross sections $\sigma_{b\bar{b}A}/\sigma_{gg\to A}$ is 0.22 in the hMSSM scenario. Accounting for a nonnegligible contribution from the $b\bar{b}A$ production

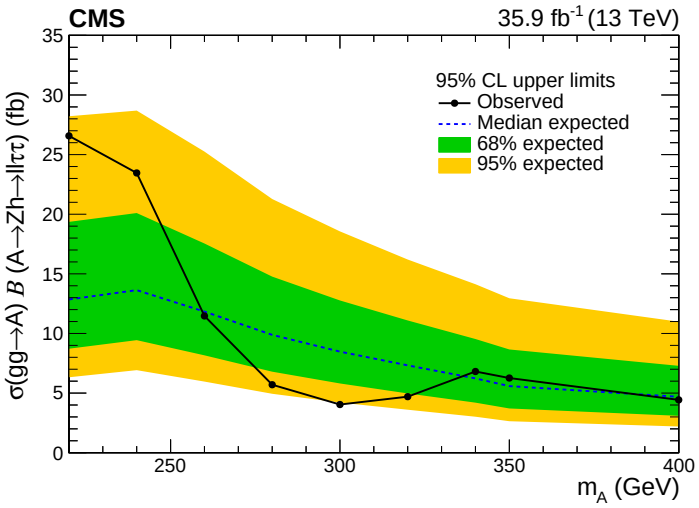

Figure 7.3: The expected and observed 95% CL model-independent upper limits on the product of the cross section and branching fraction $\sigma(\mathrm{gg} \to \mathrm{A})\mathcal{B}(\mathrm{A} \to \mathrm{Zh} \to \ell\ell\tau\tau)$ are shown. The green (yellow) band corresponds to the 68 (95)% confidence intervals for the expected limit.

requires scaling the yield of the signal process resulting from gg → A production, as the simulated signal events are generated only with the gg → A process. The scaling is performed at each point in the m_A–tan β plane as follows:

$$\text{Total signal yield} = \mathrm{gg} \to \mathrm{A}\text{ yield} \times \left(1 + \epsilon_{\mathrm{b\bar{b}A/gg\to A}} \times \frac{\sigma_{\mathrm{b\bar{b}A}}}{\sigma_{\mathrm{gg\to A}}}\right), \tag{7.1}$$

where $\epsilon_{\mathrm{b\bar{b}A/gg\to A}}$ stands for the difference in the signal region selection efficiency, measured to be 0.76 at a single mass point ($m_\mathrm{A} = 300\,\mathrm{GeV}$). Additional studies were performed to confirm that for the studied mass range (220–400 GeV) the efficiency is nearly flat.

The model-dependent results are shown in Fig. 7.4 in the m_A–tan β plane. The trend seen in Fig. 7.2 is visible also in the model-dependent interpretation of the results.

The observed and expected limits in the hMSSM scenario are shown together with numerous results from other analyses by the CMS Collaboration in Fig. 7.5. The parameter space region with low tan β values for $220 < m_\mathrm{A} < 350\,\mathrm{GeV}$ can be constrained by this search that also supports the results of previous direct and

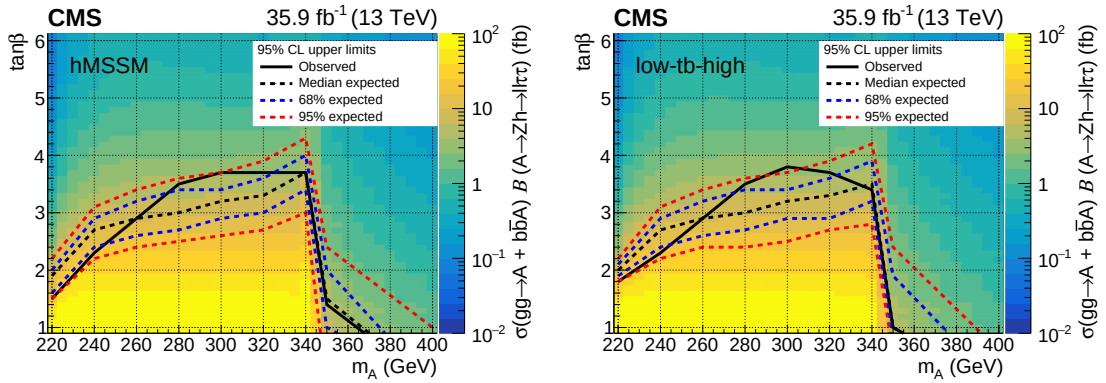

Figure 7.4: The expected and observed 95% CL exclusion limits in the m_{A}–tan β plane are shown for two MSSM scenarios: hMSSM (left) and low-tb-high (right). The area under the solid black curve is excluded. The dashed black curve corresponds to the median expected limit, surrounded by the 68 (95)% confidence intervals in blue (red). The limits are overlaid on a background showing the $\sigma(\mathrm{gg} \to \mathrm{A} + \mathrm{b\bar{b}A})\mathcal{B}(\mathrm{A} \to \mathrm{Zh} \to \ell\ell\tau\tau)$ as predicted by each model at each grid point.

indirect searches. Out of the direct searches targeting the m_{A} values below 400 GeV, this analysis has a similar sensitivity as the searches using the $\mathrm{A} \to \mathrm{Zh}(\mathrm{h} \to \mathrm{b\bar{b}})$ decay, performed by the ATLAS and CMS Collaborations [44, 45]. Moreover, the results of this analysis exclude a large part of the parameter space region with low tan β values together with an analysis which targets the decay of the H boson into a pair of W or Z bosons [48, 153, 154]. Other striking exclusion limits in the figure are the ones obtained from the combined measurement of the standard model Higgs boson couplings, that indicate that m_{A} values below 600 GeV are disfavoured by the observed data [33]. This is due to a parameter included in the combined measurement, the ratio of the Higgs boson couplings to up- and down-type fermions (λ_{du}), which has a best fit value below unity. In the hMSSM scenario, however, the parameter is required to be greater than unity for most of the parameter space. The said parameter approaches unity only for larger m_{A} values, resulting in the strong exclusion limits for m_{A} values below 600 GeV. The ATLAS Collaboration has presented similar exclusion limits [155].

In contrast to the hMSSM scenario, the CMS Collaboration has previously

set model-dependent limits in the low-tb-high scenario using the $A \to Zh \to \ell\ell\tau\tau$ decay channel. The earlier observed (expected) limits excluded $\tan\beta$ values up to 2.7 (2.4) at $m_A = 300\,\text{GeV}$ [43], whereas a $\tan\beta$ value of 3.8 (3.2) is reached by this analysis. Thus, the limits are improved by more than 30% for $m_A = 300\,\text{GeV}$. The improvement in the limits is mainly due to the new mass reconstruction method and the optimization of the event selection described in Section 5.5.

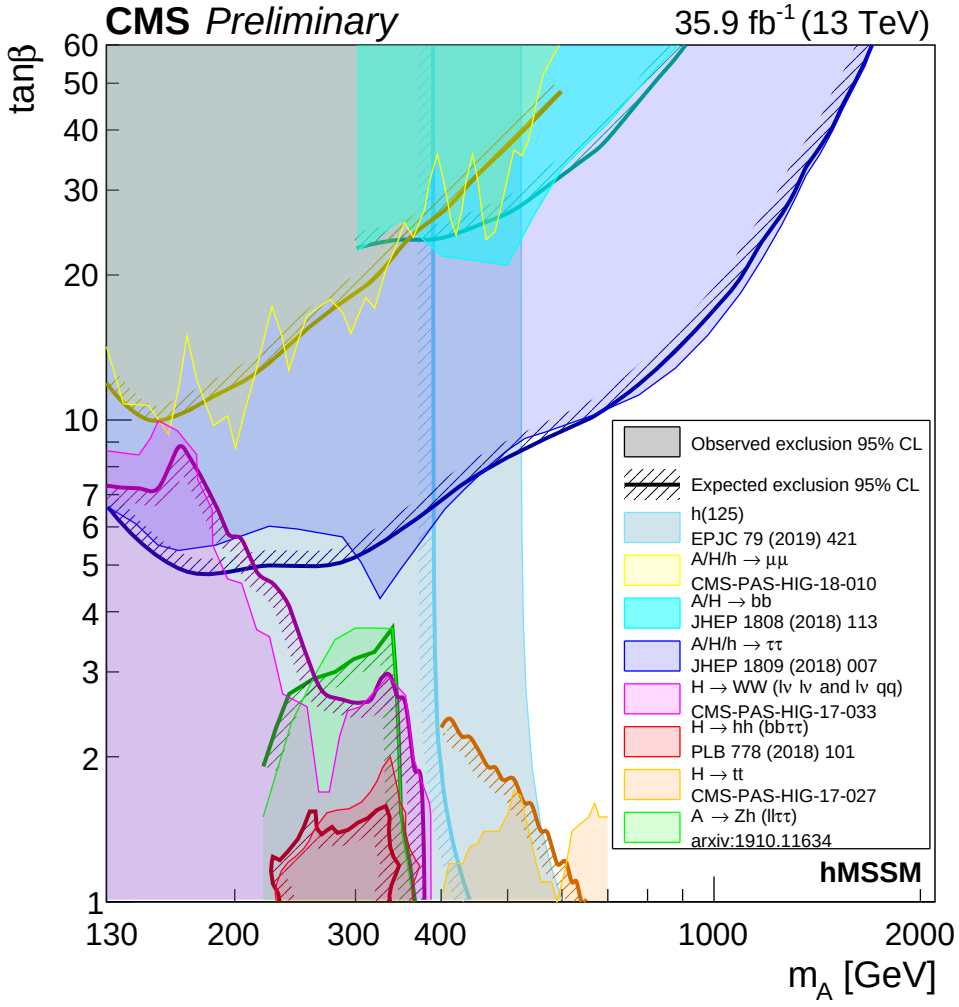

Figure 7.5: The expected and observed 95% CL exclusion limits in the m_A–$\tan\beta$ plane, obtained by numerous analyses by the CMS Collaboration, are shown for the hMSSM scenario. [156]

8. Summary and outlook

This thesis presents a search for a pseudoscalar A boson decaying into a standard model-like Higgs boson and a Z boson. The SM-like Higgs boson subsequently decays into tau leptons, whereas the Z boson decays into a pair of electrons or muons. The search targets gluon fusion production of the A boson, and four $\mathrm{h} \to \tau\tau$ decay channels are covered: $\mathrm{e}\tau_\mathrm{h}$, $\mu\tau_\mathrm{h}$, $\tau_\mathrm{h}\tau_\mathrm{h}$, and $\mathrm{e}\mu$. The search is based on a data sample of proton-proton collisions collected at $\sqrt{s} = 13\,\mathrm{TeV}$ by the CMS experiment at the LHC, corresponding to an integrated luminosity of $35.9\,\mathrm{fb}^{-1}$. This search is the first of its kind using 13 TeV proton-proton collision data.

The search is an important handle to explore the parameter space of different benchmark scenarios of two-Higgs-doublet models. It can exclude a part of the phase space region with low $\tan\beta$ values when the mass of the A boson is lower than 350 GeV. For example, in the hMSSM scenario of the minimal sypersymmetric standard model, this is expected to be one of the most sensitive searches in the phase space region with low $\tan\beta$ values when m_A is between 260 and 350 GeV.

The main discriminating variable between the signal and the background processes is the reconstructed A boson mass. By constraining the mass of the Higgs boson h to 125 GeV in the $\mathrm{h} \to \tau\tau$ four-vector reconstruction using the SVFIT algorithm, the sensitivity of the search is increased remarkably since the previous analysis [43]. As a result, the mass resolution improves from 10% to 3% at $m_\mathrm{A} = 300\,\mathrm{GeV}$, and the sensitivity is increased by 30% compared to sensitivity obtained with the

mass reconstruction methods used in the previous analysis. Kinematic selections based on the reconstructed mass of the standard model-like Higgs boson further optimise the signal extraction.

The observed data agrees with the background predictions from the standard model. Model-independent as well as model-dependent exclusion limits in the m_{A}–$\tan\beta$ plane for two minimal supersymmetric standard model scenarios, hMSSM and low-tb-high, are set. The observed model-independent limit on the product of the gluon fusion production cross section and the branching fraction for the $\mathrm{A} \to \mathrm{Zh} \to \ell\ell\tau\tau$ decay ranges from 27 fb at 220 GeV to 5 fb at 400 GeV. The observed model-dependent limits on the process $\sigma(\mathrm{gg} \to \mathrm{A} + \mathrm{b\bar{b}A})\mathcal{B}(\mathrm{A} \to \mathrm{Zh} \to \ell\ell\tau\tau)$ for the hMSSM (low-tb-high) scenario exclude $\tan\beta$ values from 1.6 (1.8) at $m_{\mathrm{A}} = 220$ GeV to 3.7 (3.8) at $m_{\mathrm{A}} = 300$ GeV. Compared to the previous results by the CMS Collaboration [43], the limits are improved by more than 30% for $m_{\mathrm{A}} = 300$ GeV. This results from the new mass reconstruction method, and the optimisation of the event selection.

As this analysis is limited by the statistical uncertainties, producing an analysis utilising the full Run 2 data set corresponding to integrated luminosity of $\sim$140 fb^{-1} will offer more sensitivity to multiple MSSM scenarios. To fully take advantage of the increased amount of data, the analysis could be improved for example by targeting the bottom quark associated production of the A boson. Moreover, developing the alternative method (discussed in Section 5.6) to estimate the yield and the shape of the reducible background would provide even more precise background predictions, and thus improve the results further.

Bibliography

[1] CMS Collaboration, "Search for a heavy pseudoscalar Higgs boson decaying into a 125 GeV Higgs boson and a Z boson in final states with two tau and two light leptons at $\sqrt{s} = 13$ TeV", CMS-HIG-18-023, CERN-EP-2019-231, 2019. arXiv:1910.11634, Submitted to *JHEP*.

[2] S. L. Glashow, "Partial-symmetries of weak interactions", *Nuclear Physics* **22** (1961) 579, doi:10.1016/0029-5582(61)90469-2, http://www.sciencedirect.com/science/article/pii/0029558261904692.

[3] S. Weinberg, "A model of leptons", *Phys. Rev. Lett.* **19** (1967) 1264, doi:10.1103/PhysRevLett.19.1264.

[4] A. Salam, "Weak and electromagnetic interactions", in *Elementary particle physics: relativistic groups and analyticity*, N. Svartholm, ed., p. 367. Almqvist & Wiksell, Stockholm, 1968. Proceedings of the eighth Nobel symposium.

[5] ATLAS Collaboration, "Observation of a new particle in the search for the standard model Higgs boson with the ATLAS detector at the LHC", *Phys. Lett. B* **716** (2012) 1, doi:10.1016/j.physletb.2012.08.020, arXiv:1207.7214.

[6] CMS Collaboration, "Observation of a new boson at a mass of 125 GeV with

the CMS experiment at the LHC", *Phys. Lett. B* **716** (2012) 30, doi:10.1016/j.physletb.2012.08.021, arXiv:1207.7235.

[7] CMS Collaboration, "Observation of a new boson with mass near 125 GeV in pp collisions at $\sqrt{s} = 7$ and 8 TeV", *JHEP* **06** (2013) 081, doi:10.1007/JHEP06(2013)081, arXiv:1303.4571.

[8] T. D. Lee, "A theory of spontaneous T violation", *Phys. Rev. D* **8** (1973) 1226, doi:10.1103/PhysRevD.8.1226.

[9] G. C. Branco et al., "Theory and phenomenology of two-Higgs-doublet models", *Phys. Rept.* **516** (2012) 1, doi:10.1016/j.physrep.2012.02.002, arXiv:1106.0034.

[10] Y. Nagashima, "Beyond the standard model of elementary particle physics". Wiley-VCH, Weinheim, 2014. doi:10.1002/9783527665020.

[11] A. Djouadi and J. Quevillon, "The MSSM Higgs sector at a high M_{SUSY}: reopening the low tanβ regime and heavy Higgs searches", *JHEP* **10** (2013) 028, doi:10.1007/JHEP10(2013)028, arXiv:1304.1787.

[12] L. Maiani, A. D. Polosa, and V. Riquer, "Bounds to the Higgs sector masses in minimal supersymmetry from LHC data", *Phys. Lett. B* **724** (2013) 274, doi:10.1016/j.physletb.2013.06.026, arXiv:1305.2172.

[13] A. Djouadi et al., "The post-Higgs MSSM scenario: Habemus MSSM?", *Eur. Phys. J. C* **73** (2013) 2650, doi:10.1140/epjc/s10052-013-2650-0, arXiv:1307.5205.

[14] A. Djouadi et al., "Fully covering the MSSM Higgs sector at the LHC", *JHEP* **06** (2015) 168, doi:10.1007/JHEP06(2015)168, arXiv:1502.05653.

[15] E. Bagnaschi et al., "Benchmark scenarios for low $\tan\beta$ in the MSSM", Technical Report LHCHXSWG-2015-002, 2015. https://cds.cern.ch/record/2039911.

[16] CMS Collaboration, "Particle-flow reconstruction and global event description with the CMS detector", *JINST* **12** (2017) P10003, doi:10.1088/1748-0221/12/10/P10003, arXiv:1706.04965.

[17] L. Bianchini, J. Conway, E. K. Friis, and C. Veelken, "Reconstruction of the Higgs mass in $H \to \tau\tau$ events by dynamical likelihood techniques", *J. Phys. Conf. Ser.* **513** (2014) 022035, doi:10.1088/1742-6596/513/2/022035.

[18] L. Bianchini et al., "Reconstruction of the Higgs mass in events with Higgs bosons decaying into a pair of τ leptons using matrix element techniques", *Nucl. Instrum. Meth. A* **862** (2017) 54, doi:10.1016/j.nima.2017.05.001, arXiv:1603.05910.

[19] F. Englert and R. Brout, "Broken symmetry and the mass of gauge vector mesons", *Phys. Rev. Lett.* **13** (1964) 321, doi:10.1103/PhysRevLett.13.321.

[20] P. W. Higgs, "Broken symmetries, massless particles and gauge fields", *Phys. Lett.* **12** (1964) 132, doi:10.1016/0031-9163(64)91136-9.

[21] P. W. Higgs, "Broken symmetries and the masses of gauge bosons", *Phys. Rev. Lett.* **13** (1964) 508, doi:10.1103/PhysRevLett.13.508.

[22] G. S. Guralnik, C. R. Hagen, and T. W. B. Kibble, "Global conservation laws and massless particles", *Phys. Rev. Lett.* **13** (1964) 585, doi:10.1103/PhysRevLett.13.585.

[23] P. W. Higgs, "Spontaneous symmetry breakdown without massless bosons", *Phys. Rev.* **145** (1966) 1156, doi:10.1103/PhysRev.145.1156.

[24] T. W. B. Kibble, "Symmetry breaking in non-Abelian gauge theories", *Phys. Rev.* **155** (1967) 1554, doi:10.1103/PhysRev.155.1554.

[25] ATLAS Collaboration, "Observation and measurement of Higgs boson decays to WW* with the ATLAS detector", *Phys. Rev. D* **92** (2015) 012006, doi:10.1103/PhysRevD.92.012006, arXiv:1412.2641.

[26] CMS Collaboration, "Measurements of properties of the Higgs boson decaying to a W boson pair in pp collisions at $\sqrt{s} = 13$ TeV", *Phys. Lett. B* **791** (2019) 96, doi:10.1016/j.physletb.2018.12.073, arXiv:1806.05246.

[27] ATLAS Collaboration, "Cross-section measurements of the Higgs boson decaying into a pair of τ-leptons in proton-proton collisions at $\sqrt{s} = 13$ TeV with the ATLAS detector", *Phys. Rev. D* **99** (2019) 072001, doi:10.1103/PhysRevD.99.072001, arXiv:1811.08856.

[28] CMS Collaboration, "Observation of the Higgs boson decay to a pair of τ leptons with the CMS detector", *Phys. Lett. B* **779** (2018) 283, doi:10.1016/j.physletb.2018.02.004, arXiv:1708.00373.

[29] ATLAS Collaboration, "Observation of $H \to b\bar{b}$ decays and VH production with the ATLAS detector", *Phys. Lett. B* **786** (2018) 59, doi:10.1016/j.physletb.2018.09.013, arXiv:1808.08238.

[30] CMS Collaboration, "Observation of Higgs boson decay to bottom quarks", *Phys. Rev. Lett.* **121** (2018) 121801, doi:10.1103/PhysRevLett.121.121801, arXiv:1808.08242.

[31] ATLAS and CMS Collaborations, "Measurements of the Higgs boson production and decay rates and constraints on its couplings from a combined ATLAS and CMS analysis of the LHC pp collision data at $\sqrt{s} = 7$ and 8

TeV", *JHEP* **08** (2016) 045, doi:10.1007/JHEP08(2016)045, arXiv:1606.02266.

[32] CMS Collaboration, "Measurement and interpretation of differential cross sections for Higgs boson production at $\sqrt{s} = 13$ TeV", *Phys. Lett. B* **792** (2019) 369, doi:10.1016/j.physletb.2019.03.059, arXiv:1812.06504.

[33] CMS Collaboration, "Combined measurements of Higgs boson couplings in proton–proton collisions at $\sqrt{s} = 13\,\text{TeV}$", *Eur. Phys. J. C* **79** (2019) 421, doi:10.1140/epjc/s10052-019-6909-y, arXiv:1809.10733.

[34] CMS Collaboration, "Measurements of properties of the Higgs boson decaying into the four-lepton final state in pp collisions at $\sqrt{s} = 13$ TeV", *JHEP* **11** (2017) 047, doi:10.1007/JHEP11(2017)047, arXiv:1706.09936.

[35] ATLAS and CMS Collaborations, "Combined measurement of the Higgs boson mass in pp collisions at $\sqrt{s} = 7$ and 8 TeV with the ATLAS and CMS experiments", *Phys. Rev. Lett.* **114** (2015) 191803, doi:10.1103/PhysRevLett.114.191803, arXiv:1503.07589.

[36] ATLAS Collaboration, "Measurement of the Higgs boson mass in the $H \to ZZ^* \to 4\ell$ and $H \to \gamma\gamma$ channels with $\sqrt{s} = 13$ TeV pp collisions using the ATLAS detector", *Phys. Lett. B* **784** (2018) 345, doi:10.1016/j.physletb.2018.07.050, arXiv:1806.00242.

[37] S. P. Martin, "A Supersymmetry primer", FERMILAB-PUB-97-425-T, 1997. arXiv:hep-ph/9709356.

[38] LHC Higgs Cross Section Working Group Collaboration, "Handbook of LHC Higgs Cross Sections: 4. Deciphering the Nature of the Higgs Sector", FERMILAB-FN-1025-T, CERN-2017-002-M, 2016. doi:10.23731/CYRM-2017-002, arXiv:1610.07922.

[39] ATLAS Collaboration, "Search for additional heavy neutral Higgs and gauge bosons in the ditau final state produced in 36 fb^{-1} of pp collisions at $\sqrt{s} = 13$ TeV with the ATLAS detector", *JHEP* **01** (2018) 055, doi:10.1007/JHEP01(2018)055, arXiv:1709.07242.

[40] CMS Collaboration, "Search for additional neutral MSSM Higgs bosons in the $\tau\tau$ final state in proton-proton collisions at $\sqrt{s} = 13$ TeV", *JHEP* **09** (2018) 007, doi:10.1007/JHEP09(2018)007, arXiv:1803.06553.

[41] H. Bahl, S. Liebler, and T. Stefaniak, "MSSM Higgs benchmark scenarios for Run 2 and beyond: the low tan β region", *Eur. Phys. J. C* **79** (2019) 279, doi:10.1140/epjc/s10052-019-6770-z, arXiv:1901.05933.

[42] ATLAS Collaboration, "Search for a CP-odd Higgs boson decaying to Zh in pp collisions at $\sqrt{s} = 8$ TeV with the ATLAS detector", *Phys. Lett. B* **744** (2015) 163, doi:10.1016/j.physletb.2015.03.054, arXiv:1502.04478.

[43] CMS Collaboration, "Searches for a heavy scalar boson H decaying to a pair of 125 GeV Higgs bosons hh or for a heavy pseudoscalar boson A decaying to Zh, in the final states with $h \to \tau\tau$", *Phys. Lett. B* **755** (2016) 217, doi:10.1016/j.physletb.2016.01.056, arXiv:1510.01181.

[44] ATLAS Collaboration, "Search for heavy resonances decaying into a W or Z boson and a Higgs boson in final states with leptons and b-jets in 36 fb^{-1} of $\sqrt{s} = 13$ TeV pp collisions with the ATLAS detector", *JHEP* **03** (2018) 174, doi:10.1007/JHEP03(2018)174, arXiv:1712.06518, [Erratum: 10.1007/JHEP11(2018)051].

[45] CMS Collaboration, "Search for a heavy pseudoscalar boson decaying to a Z and a Higgs boson at $\sqrt{s} = 13$ TeV", *Eur. Phys. J. C* **79** (2019) 564, doi:10.1140/epjc/s10052-019-7058-z, arXiv:1903.00941.

[46] CMS Collaboration, "Search for Higgs boson pair production in events with two bottom quarks and two tau leptons in proton–proton collisions at $\sqrt{s} = 13$ TeV", *Phys. Lett. B* **778** (2018) 101, doi:10.1016/j.physletb.2018.01.001, arXiv:1707.02909.

[47] CMS Collaboration, "Search for heavy Higgs bosons decaying to a top quark pair in proton-proton collisions at $\sqrt{s} = 13$ TeV", CMS-HIG-17-027, CERN-EP-2019-147, 2019. arXiv:1908.01115, Submitted to *JHEP*.

[48] CMS Collaboration, "Search for a heavy Higgs boson decaying to a pair of W bosons in proton-proton collisions at $\sqrt{s} = 13$ TeV", CMS Physics Analysis Summary CMS-PAS-HIG-17-033, 2019. https://cds.cern.ch/record/2668687.

[49] W. Herr and B. Muratori, "Concept of luminosity", 2006. doi:10.5170/CERN-2006-002.361, https://cds.cern.ch/record/941318.

[50] R. Sahoo, "Relativistic Kinematics", 2016. arXiv:1604.02651.

[51] L. R. Evans and P. Bryant, "LHC Machine", *JINST* **3** (2008) S08001, doi:10.1088/1748-0221/3/08/S08001, http://cds.cern.ch/record/1129806.

[52] J. J. Goodson, "Search for supersymmetry in states with large missing transverse momentum and three leptons including a Z-boson". PhD thesis, SUNY, Stony Brook, 2012. http://cds.cern.ch/record/1449722.

[53] CMS Collaboration, "Public CMS Luminosity Information", https://twiki.cern.ch/twiki/bin/view/CMSPublic/LumiPublicResults.

[54] CMS Collaboration, "The CMS experiment at the CERN LHC", *JINST* **3** (2008) S08004, doi:10.1088/1748-0221/3/08/S08004.

[55] T. Sakuma and T. McCauley, "Detector and Event Visualization with

SketchUp at the CMS Experiment", *J.Phys.Conf.Ser.* **513** (2014) 022032, doi:10.1088/1742-6596/513/2/022032, arXiv:1311.4942.

[56] M. Schott and M. Dunford, "Review of single vector boson production in pp collisions at $\sqrt{s} = 7$ TeV", *Eur. Phys. J. C* **74** (2014) 2916, doi:10.1140/epjc/s10052-014-2916-1, arXiv:1405.1160.

[57] CMS Collaboration, "Description and performance of track and primary-vertex reconstruction with the CMS tracker", *JINST* **9** (2014) P10009, doi:10.1088/1748-0221/9/10/P10009, arXiv:1405.6569.

[58] A. Dominguez et al., "CMS Technical Design Report for the Pixel Detector Upgrade", CMS Technical Design Report CERN-LHCC-2012-016, CMS-TDR-11, 2012. http://cds.cern.ch/record/1481838.

[59] H. A. Weber, "The construction of the phase 1 upgrade of the CMS pixel detector", CMS Conference Report CMS-CR-2017-247, 2017. doi:10.1088/1748-0221/12/12/C12049, http://cds.cern.ch/record/2285254.

[60] W. Adam, R. Frühwirth, A. Strandlie, and T. Todor, "Reconstruction of Electrons with the Gaussian-Sum Filter in the CMS Tracker at the LHC", Technical Report CMS-NOTE-2005-001, 2005. https://cds.cern.ch/record/815410.

[61] CMS Collaboration, "Performance of electron reconstruction and selection with the CMS detector in proton-proton collisions at $\sqrt{s} = 8\,\text{TeV}$", *JINST* **10** (2015) P06005, doi:10.1088/1748-0221/10/06/P06005, arXiv:1502.02701.

[62] CMS Collaboration, "CMS Physics: Technical Design Report Volume 1:

Detector Performance and Software", CMS Technical Design Report CERN-LHCC-2006-001, 2006. https://cds.cern.ch/record/922757.

[63] J. Mans et al., "CMS Technical Design Report for the Phase 1 Upgrade of the Hadron Calorimeter", CMS Technical Design Report CERN-LHCC-2012-015, CMS-TDR-10, 2012. https://cds.cern.ch/record/1481837.

[64] CMS HCAL/ECAL Collaboration, "The CMS barrel calorimeter response to particle beams from 2 to 350 GeV/c", *Eur. Phys. J. C* **60** (2009) 359, doi:10.1140/epjc/s10052-009-0959-5.

[65] CMS-HCAL Collaboration, "Design, performance, and calibration of the CMS forward calorimeter wedges", *Eur. Phys. J. C* **53** (2008) 139, doi:10.1140/epjc/s10052-007-0459-4.

[66] CMS Collaboration, "Performance of the CMS muon detector and muon reconstruction with proton-proton collisions at $\sqrt{s} = 13$ TeV", *JINST* **13** (2018) P06015, doi:10.1088/1748-0221/13/06/P06015, arXiv:1804.04528.

[67] CMS Collaboration, "The CMS trigger system", *JINST* **12** (2017) P01020, doi:10.1088/1748-0221/12/01/P01020, arXiv:1609.02366.

[68] CMS Collaboration, "CMS Technical Design Report for the Level-1 Trigger Upgrade", CMS Technical Design Report CERN-LHCC-2013-011, CMS-TDR-12, 2013. http://cds.cern.ch/record/1556311.

[69] K. Compton et al., "The MP7 and CTP-6: multi-hundred gbps processing boards for calorimeter trigger upgrades at CMS", *JINST* **7** (2012) C12024, doi:10.1088/1748-0221/7/12/c12024.

[70] D. Acosta et al., "The CMS modular track finder boards, MTF6 and MTF7", *JINST* **8** (2013) C12034, doi:10.1088/1748-0221/8/12/c12034.

[71] CMS Collaboration, "Dimuon Level-1 invariant mass in 2017 data", CMS Detector Performance Summary CMS-DP-2018-002, 2018. https://cds.cern.ch/record/2305543.

[72] CMS Collaboration, "Level-1 muon trigger performance in 2017 data and comparison with the legacy muon trigger system", CMS Detector Performance Summary CMS-DP-2017-041, 2017. https://cds.cern.ch/record/2286327.

[73] CMS Collaboration, "Level-1 muon trigger performance with the full 2017 dataset", CMS Detector Performance Summary CMS-DP-2018-008, 2018. https://cds.cern.ch/record/2306376.

[74] B. Kreis et al., "Run 2 upgrades to the CMS level-1 calorimeter trigger", *JINST* **11** (2016) C01051, doi:10.1088/1748-0221/11/01/c01051, http://cds.cern.ch/record/2103853.

[75] CMS Collaboration, "Level-1 E/Gamma performance on 2017 data", CMS Detector Performance Summary CMS-DP-2018-003, 2018. http://cds.cern.ch/record/2305544.

[76] CMS Collaboration, "Level-1 τ trigger performance in 2017 data", CMS Detector Performance Summary CMS-DP-2018-006, 2018. https://cds.cern.ch/record/2305547.

[77] CMS Collaboration, "Level-1 jets and energy sums trigger performance with full 2017 dataset", CMS Detector Performance Summary CMS-DP-2018-004, 2018. http://cds.cern.ch/record/2305545.

[78] CMS Collaboration, "Performance of CMS muon reconstruction in pp collision events at $\sqrt{s} = 7$ TeV", *JINST* **7** (2012) P10002, doi:10.1088/1748-0221/7/10/P10002, arXiv:1206.4071.

[79] G. Petrucciani, A. Rizzi, and C. Vuosalo, "Mini-AOD: A New Analysis Data Format for CMS", CMS Conference Report CMS-CR-2015-052, 2015. doi:10.1088/1742-6596/664/7/072052, http://cds.cern.ch/record/2029414.

[80] W. Adam, B. Mangano, T. Speer, and T. Todorov, "Track Reconstruction in the CMS tracker", Technical Report CMS-NOTE-2006-041, 2006. https://cds.cern.ch/record/934067.

[81] R. Frühwirth, "Application of Kalman filtering to track and vertex fitting", *Nucl. Instrum. Methods Phys. Res., A* **262** (1987) 444, doi:10.1016/0168-9002(87)90887-4, https://cds.cern.ch/record/178627.

[82] M. Cacciari, G. P. Salam, and G. Soyez, "FastJet user manual", *Eur. Phys. J. C* **72** (2012) 1896, doi:10.1140/epjc/s10052-012-1896-2, arXiv:1111.6097.

[83] M. Cacciari and G. P. Salam, "Dispelling the N^3 myth for the k_{T} jet-finder", *Phys. Lett. B* **641** (2006) 57, doi:10.1016/j.physletb.2006.08.037, arXiv:hep-ph/0512210.

[84] M. Cacciari, G. P. Salam, and G. Soyez, "The anti-k_{T} jet clustering algorithm", *JHEP* **04** (2008) 063, doi:10.1088/1126-6708/2008/04/063, arXiv:0802.1189.

[85] CMS Collaboration, "Jet energy scale and resolution in the CMS experiment in pp collisions at 8 TeV", *JINST* **12** (2017) P02014, doi:10.1088/1748-0221/12/02/P02014, arXiv:1607.03663.

[86] CMS Collaboration, "Identification of heavy-flavour jets with the CMS detector in pp collisions at 13 TeV", *JINST* **13** (2017) P05011, doi:10.1088/1748-0221/13/05/P05011, arXiv:1712.07158.

[87] CMS Collaboration, "Reconstruction and identification of τ lepton decays to hadrons and ν_τ at CMS", *JINST* **11** (2016) P01019, doi:10.1088/1748-0221/11/01/P01019, arXiv:1510.07488.

[88] CMS Collaboration, "Performance of reconstruction and identification of τ leptons decaying to hadrons and ν_τ in pp collisions at $\sqrt{s} = 13$ TeV", *JINST* **13** (2018) P10005, doi:10.1088/1748-0221/13/10/P10005, arXiv:1809.02816.

[89] CMS Collaboration, "Performance of missing transverse momentum reconstruction in proton-proton collisions at $\sqrt{s} = 13$ TeV using the CMS detector", *JINST* **14** (2019) P07004, doi:10.1088/1748-0221/14/07/P07004, arXiv:1903.06078.

[90] A. Buckley et al., "General-purpose event generators for LHC physics", *Phys. Rept.* **504** (2011) 145, doi:10.1016/j.physrep.2011.03.005, arXiv:1101.2599.

[91] M. H. Seymour and M. Marx, "Monte Carlo Event Generators", in *Proceedings, 69th Scottish Universities Summer School in Physics : LHC Phenomenology (SUSSP69): St.Andrews, Scotland, August 19-September 1, 2012*, p. 287. 2013. arXiv:1304.6677. doi:10.1007/978-3-319-05362-2_8.

[92] J. Alwall et al., "The automated computation of tree-level and next-to-leading order differential cross sections, and their matching to parton

shower simulations", *JHEP* **07** (2014) 079, doi:10.1007/JHEP07(2014)079, arXiv:1405.0301.

[93] P. Nason, "A new method for combining NLO QCD with shower Monte Carlo algorithms", *JHEP* **11** (2004) 040, doi:10.1088/1126-6708/2004/11/040, arXiv:hep-ph/0409146.

[94] S. Frixione, P. Nason, and C. Oleari, "Matching NLO QCD computations with parton shower simulations: the POWHEG method", *JHEP* **11** (2007) 070, doi:10.1088/1126-6708/2007/11/070, arXiv:0709.2092.

[95] S. Alioli, P. Nason, C. Oleari, and E. Re, "A general framework for implementing NLO calculations in shower Monte Carlo programs: the POWHEG BOX", *JHEP* **06** (2010) 043, doi:10.1007/JHEP06(2010)043, arXiv:1002.2581.

[96] T. Sjöstrand et al., "An introduction to PYTHIA 8.2", *Comput. Phys. Commun.* **191** (2015) 159, doi:10.1016/j.cpc.2015.01.024, arXiv:1410.3012.

[97] CMS Collaboration, "Event generator tunes obtained from underlying event and multiparton scattering measurements", *Eur. Phys. J. C* **76** (2016) 155, doi:10.1140/epjc/s10052-016-3988-x, arXiv:1512.00815.

[98] R. D. Ball et al., "Unbiased global determination of parton distributions and their uncertainties at NNLO and at LO", *Nucl. Phys. B* **855** (2012) 153, doi:10.1016/j.nuclphysb.2011.09.024, arXiv:1107.2652.

[99] GEANT4 Collaboration, "GEANT4—a simulation toolkit", *Nucl. Instrum. Meth. A* **506** (2003) 250, doi:10.1016/S0168-9002(03)01368-8.

[100] M. Carena et al., "MSSM Higgs Boson Searches at the LHC: Benchmark

Scenarios after the Discovery of a Higgs-like Particle", *Eur. Phys. J. C* **73** (2013) 2552, doi:10.1140/epjc/s10052-013-2552-1, arXiv:1302.7033.

[101] S. Alioli et al., "Jet pair production in POWHEG", *JHEP* **04** (2011) 081, doi:10.1007/JHEP04(2011)081, arXiv:1012.3380.

[102] S. Alioli, P. Nason, C. Oleari, and E. Re, "NLO Higgs boson production via gluon fusion matched with shower in POWHEG", *JHEP* **04** (2009) 002, doi:10.1088/1126-6708/2009/04/002, arXiv:0812.0578.

[103] G. Luisoni, P. Nason, C. Oleari, and F. Tramontano, "$HW^{\pm}/HZ + 0$ and 1 jet at NLO with the POWHEG BOX interfaced to GoSam and their merging within MiNLO", *JHEP* **10** (2013) 083, doi:10.1007/JHEP10(2013)083, arXiv:1306.2542.

[104] D. de Florian, G. Ferrera, M. Grazzini, and D. Tommasini, "Higgs boson production at the LHC: Transverse momentum resummation effects in the $H \to \gamma\gamma$, $H \to WW \to l\nu l\nu$ and $H \to ZZ \to 4l$ decay modes", *JHEP* **06** (2012) 132, doi:10.1007/JHEP06(2012)132, arXiv:1203.6321.

[105] M. Grazzini and H. Sargsyan, "Heavy-quark mass effects in Higgs boson production at the LHC", *JHEP* **09** (2013) 129, doi:10.1007/JHEP09(2013)129, arXiv:1306.4581.

[106] A. Denner et al., "Standard model Higgs-boson branching ratios with uncertainties", *Eur. Phys. J. C* **71** (2011) 1753, doi:10.1140/epjc/s10052-011-1753-8, arXiv:1107.5909.

[107] NNPDF Collaboration, "Impact of heavy quark masses on parton distributions and LHC phenomenology", *Nucl. Phys. B* **849** (2011) 296, doi:10.1016/j.nuclphysb.2011.03.021, arXiv:1101.1300.

[108] J. M. Campbell and R. K. Ellis, "MCFM for the Tevatron and the LHC", *Nucl. Phys. B Proc. Suppl.* **205-206** (2010) 10, doi:10.1016/j.nuclphysbps.2010.08.011, arXiv:1007.3492.

[109] R. Frederix and S. Frixione, "Merging meets matching in MC@NLO", *JHEP* **12** (2012) 061, doi:10.1007/JHEP12(2012)061, arXiv:1209.6215.

[110] J. Alwall et al., "Comparative study of various algorithms for the merging of parton showers and matrix elements in hadronic collisions", *Eur. Phys. J. C* **53** (2008) 473, doi:10.1140/epjc/s10052-007-0490-5, arXiv:0706.2569.

[111] S. Heinemeyer, W. Hollik, and G. Weiglein, "FeynHiggs: A program for the calculation of the masses of the neutral CP-even Higgs bosons in the MSSM", *Comput. Phys. Commun.* **124** (2000) 76, doi:10.1016/S0010-4655(99)00364-1, arXiv:hep-ph/9812320.

[112] S. Heinemeyer, W. Hollik, and G. Weiglein, "The masses of the neutral CP-even Higgs bosons in the MSSM: Accurate analysis at the two-loop level", *Eur. Phys. J. C* **9** (1999) 343, doi:10.1007/s100529900006, arXiv:hep-ph/9812472.

[113] G. Degrassi et al., "Towards high-precision predictions for the MSSM Higgs sector", *Eur. Phys. J. C* **28** (2003) 133, doi:10.1140/epjc/s2003-01152-2, arXiv:hep-ph/0212020.

[114] M. Frank et al., "The Higgs boson masses and mixings of the complex MSSM in the Feynman-diagrammatic approach", *JHEP* **02** (2007) 047, doi:10.1088/1126-6708/2007/02/047, arXiv:hep-ph/0611326.

[115] T. Hahn et al., "High-precision predictions for the light CP-even Higgs boson mass of the minimal supersymmetric standard model", *Phys. Rev. Lett.* **112** (2014) 141801, doi:10.1103/PhysRevLett.112.141801, arXiv:1312.4937.

[116] R. V. Harlander, S. Liebler, and H. Mantler, "SusHi: A program for the calculation of Higgs production in gluon fusion and bottom-quark annihilation in the standard model and the MSSM", *Comput. Phys. Commun.* **184** (2013) 1605, doi:10.1016/j.cpc.2013.02.006, arXiv:1212.3249.

[117] M. Spira, A. Djouadi, D. Graudenz, and P. M. Zerwas, "Higgs boson production at the LHC", *Nucl. Phys. B* **453** (1995) 17, doi:10.1016/0550-3213(95)00379-7, arXiv:hep-ph/9504378.

[118] R. V. Harlander and M. Steinhauser, "Supersymmetric Higgs production in gluon fusion at next-to-leading order", *JHEP* **09** (2004) 066, doi:10.1088/1126-6708/2004/09/066, arXiv:hep-ph/0409010.

[119] R. Harlander and P. Kant, "Higgs production and decay: Analytic results at next-to-leading order QCD", *JHEP* **12** (2005) 015, doi:10.1088/1126-6708/2005/12/015, arXiv:hep-ph/0509189.

[120] G. Degrassi and P. Slavich, "NLO QCD bottom corrections to Higgs boson production in the MSSM", *JHEP* **11** (2010) 044, doi:10.1007/JHEP11(2010)044, arXiv:1007.3465.

[121] G. Degrassi, S. Di Vita, and P. Slavich, "NLO QCD corrections to pseudoscalar Higgs production in the MSSM", *JHEP* **08** (2011) 128, doi:10.1007/JHEP08(2011)128, arXiv:1107.0914.

[122] G. Degrassi, S. Di Vita, and P. Slavich, "On the NLO QCD corrections to the production of the heaviest neutral Higgs scalar in the MSSM", *Eur. Phys. J. C* **72** (2012) 2032, doi:10.1140/epjc/s10052-012-2032-z, arXiv:1204.1016.

[123] R. V. Harlander and W. B. Kilgore, "Next-to-next-to-leading order Higgs production at hadron colliders", *Phys. Rev. Lett.* **88** (2002) 201801, doi:10.1103/PhysRevLett.88.201801, arXiv:hep-ph/0201206.

[124] C. Anastasiou and K. Melnikov, "Higgs boson production at hadron colliders in NNLO QCD", *Nucl. Phys. B* **646** (2002) 220, doi:10.1016/S0550-3213(02)00837-4, arXiv:hep-ph/0207004.

[125] V. Ravindran, J. Smith, and W. L. van Neerven, "NNLO corrections to the total cross-section for Higgs boson production in hadron-hadron collisions", *Nucl. Phys. B* **665** (2003) 325, doi:10.1016/S0550-3213(03)00457-7, arXiv:hep-ph/0302135.

[126] R. V. Harlander and W. B. Kilgore, "Production of a pseudo-scalar Higgs boson at hadron colliders at next-to-next-to leading order", *JHEP* **10** (2002) 017, doi:10.1088/1126-6708/2002/10/017, arXiv:hep-ph/0208096.

[127] C. Anastasiou and K. Melnikov, "Pseudoscalar Higgs boson production at hadron colliders in next-to-next-to-leading order QCD", *Phys. Rev. D* **67** (2003) 037501, doi:10.1103/PhysRevD.67.037501, arXiv:hep-ph/0208115.

[128] U. Aglietti, R. Bonciani, G. Degrassi, and A. Vicini, "Two-loop light fermion contribution to Higgs production and decays", *Phys. Lett. B* **595** (2004) 432, doi:10.1016/j.physletb.2004.06.063, arXiv:hep-ph/0404071.

[129] R. Bonciani, G. Degrassi, and A. Vicini, "On the generalized harmonic polylogarithms of one complex variable", *Comput. Phys. Commun.* **182** (2011) 1253, doi:10.1016/j.cpc.2011.02.011, arXiv:1007.1891.

[130] R. V. Harlander and W. B. Kilgore, "Higgs boson production in bottom quark fusion at next-to-next-to leading order", *Phys. Rev. D* **68** (2003) 013001, doi:10.1103/PhysRevD.68.013001, arXiv:hep-ph/0304035.

[131] S. Dittmaier, M. Krämer, and M. Spira, "Higgs radiation off bottom quarks at the Fermilab Tevatron and the CERN LHC", *Phys. Rev. D* **70** (2004) 074010, doi:10.1103/PhysRevD.70.074010, arXiv:hep-ph/0309204.

[132] S. Dawson, C. B. Jackson, L. Reina, and D. Wackeroth, "Exclusive Higgs boson production with bottom quarks at hadron colliders", *Phys. Rev. D* **69** (2004) 074027, doi:10.1103/PhysRevD.69.074027, arXiv:hep-ph/0311067.

[133] R. Harlander, M. Kramer, and M. Schumacher, "Bottom-quark associated Higgs-boson production: reconciling the four- and five-flavour scheme approach", CERN-PH-TH-2011-134, FR-PHENO-2011-009, TTK-11-17, WUB-11-04, 2011. arXiv:1112.3478.

[134] A. Djouadi, J. Kalinowski, and M. Spira, "HDECAY: A program for Higgs boson decays in the standard model and its supersymmetric extension", *Comput. Phys. Commun.* **108** (1998) 56, doi:10.1016/S0010-4655(97)00123-9, arXiv:hep-ph/9704448.

[135] A. Djouadi, M. M. Mühlleitner, and M. Spira, "Decays of supersymmetric particles: The program SUSY-HIT (SUspect-SdecaY-Hdecay-InTerface)", *Acta Phys. Polon. B* **38** (2007) 635, arXiv:hep-ph/0609292.

[136] A. Djouadi, J. Kalinowski, M. Mühlleitner, and M. Spira, "HDECAY: Twenty$_{++}$ years after", *Comput. Phys. Commun.* **238** (2019) 214, doi:10.1016/j.cpc.2018.12.010, arXiv:1801.09506.

[137] A. Bredenstein, A. Denner, S. Dittmaier, and M. M. Weber, "Precise predictions for the Higgs-boson decay H→ WW/ZZ → 4 leptons", *Phys. Rev. D* **74** (2006) 013004, doi:10.1103/PhysRevD.74.013004, arXiv:hep-ph/0604011.

[138] A. Bredenstein, A. Denner, S. Dittmaier, and M. M. Weber, "Precision calculations for the Higgs decays H → ZZ/WW → 4 leptons", *Nucl. Phys. B Proc. Suppl.* **160** (2006) 131, doi:10.1016/j.nuclphysbps.2006.09.104, arXiv:hep-ph/0607060.

[139] A. Bredenstein, A. Denner, S. Dittmaier, and M. M. Weber, "Radiative corrections to the semileptonic and hadronic Higgs-boson decays H → WW/ZZ → 4 fermions", *JHEP* **02** (2007) 080, doi:10.1088/1126-6708/2007/02/080, arXiv:hep-ph/0611234.

[140] CMS Collaboration, "Measurements of the Higgs boson width and anomalous HVV couplings from on-shell and off-shell production in the four-lepton final state", *Phys. Rev. D* **99** (2019) 112003, doi:10.1103/PhysRevD.99.112003, arXiv:1901.00174.

[141] F. Cascioli et al., "ZZ production at hadron colliders in NNLO QCD", *Phys. Lett. B* **735** (2014) 311, doi:10.1016/j.physletb.2014.06.056, arXiv:1405.2219.

[142] M. Grazzini, S. Kallweit, and D. Rathlev, "ZZ production at the LHC: fiducial cross sections and distributions in NNLO QCD", *Phys. Lett. B* **750** (2015) 407, doi:10.1016/j.physletb.2015.09.055, arXiv:1507.06257.

[143] S. Kallweit and M. Wiesemann, "ZZ production at the LHC: NNLO predictions for $2\ell 2\nu$ and 4ℓ signatures", *Phys. Lett. B* **786** (2018) 382, doi:10.1016/j.physletb.2018.10.016, arXiv:1806.05941.

[144] CMS Collaboration, "Electron and photon performance in CMS with the full 2016 data sample", CMS Detector Performance Summary CMS-DP-2017-004, 2017. https://cds.cern.ch/record/2255497.

[145] CMS Collaboration, "Muon Identification and Isolation efficiency on full 2016 dataset", CMS Detector Performance Summary CMS-DP-2017-007, 2017. https://cds.cern.ch/record/2257968.

[146] R. J. Barlow and C. Beeston, "Fitting using finite Monte Carlo samples", *Comput. Phys. Commun.* **77** (1993) 219, doi:10.1016/0010-4655(93)90005-W.

[147] CMS Collaboration, "CMS luminosity measurements for the 2016 data taking period", CMS Physics Analysis Summary CMS-PAS-LUM-17-001, 2017. https://cds.cern.ch/record/2257069.

[148] J. Butterworth et al., "PDF4LHC recommendations for LHC Run II", *J. Phys. G* **43** (2016) 023001, doi:10.1088/0954-3899/43/2/023001, arXiv:1510.03865.

[149] T. Junk, "Confidence level computation for combining searches with small statistics", *Nucl. Instrum. Meth. A* **434** (1999) 435, doi:10.1016/S0168-9002(99)00498-2, arXiv:hep-ex/9902006.

[150] A. L. Read, "Presentation of search results: The CL_s technique", *J. Phys. G* **28** (2002) 2693, doi:10.1088/0954-3899/28/10/313.

[151] ATLAS and CMS Collaborations, The LHC Higgs Combination Group, "Procedure for the LHC Higgs boson search combination in Summer 2011", Technical Report CMS-NOTE-2011-005, ATL-PHYS-PUB-2011-11, 2011. https://cds.cern.ch/record/1379837.

[152] G. Cowan, K. Cranmer, E. Gross, and O. Vitells, "Asymptotic formulae for likelihood-based tests of new physics", *Eur. Phys. J. C* **71** (2011) 1554, doi:10.1140/epjc/s10052-011-1554-0, arXiv:1007.1727, [Erratum: 10.1140/epjc/s10052-013-2501-z].

[153] ATLAS Collaboration, "Search for heavy resonances decaying into WW in the $e\nu\mu\nu$ final state in pp collisions at $\sqrt{s} = 13$ TeV with the ATLAS detector", *Eur. Phys. J. C* **78** (2018) 24, doi:10.1140/epjc/s10052-017-5491-4, arXiv:1710.01123.

[154] ATLAS Collaboration, "Search for heavy ZZ resonances in the $\ell^+\ell^-\ell^+\ell^-$ and $\ell^+\ell^-\nu\bar{\nu}$ final states using proton proton collisions at $\sqrt{s} = 13$ TeV with the ATLAS detector", *Eur. Phys. J. C* **78** (2018) 293, doi:10.1140/epjc/s10052-018-5686-3, arXiv:1712.06386.

[155] ATLAS Collaboration, "Combined measurements of Higgs boson production and decay using up to 80 fb^{-1} of proton-proton collision data at $\sqrt{s} = 13$ TeV collected with the ATLAS experiment", CERN-EP-2019-097, 2019. arXiv:1909.02845, Submitted to *Phys. Rev. D.*

[156] CMS Collaboration, "Higgs Physics Analysis Group Summary Plots", https://twiki.cern.ch/twiki/bin/view/CMSPublic/SummaryResultsHIG.

ISBN 978-951-51-1289-7 (paperback)

ISBN 978-951-51-1290-3 (pdf)

ISSN 1455-0563

Printed by Picaset Oy

http://ethesis.helsinki.fi

Helsinki 2019